HOKKAIDO UNIVERSITY

Title	Theoretical Study on Catalytic Property of Ceria for the Reduction of Nitrogen Oxides
Author(s)	大城, 海
Degree Grantor	北海道大学
Degree Name	博士(理学)
Dissertation Number	甲第16361号
Issue Date	2025-03-25
DOI	https://doi.org/10.14943/doctoral.k16361
Doc URL	https://hdl.handle.net/2115/97624
Type	doctoral thesis
File Information	OSHIRO_Kai.pdf



Hokkaido University Collection of Scholarly and Academic Papers : HUSCAP

Theoretical Study on Catalytic Property of Ceria for the Reduction of Nitrogen Oxides

Kai Oshiro

Hokkaido University

2025

窒素酸化物還元における酸化セリウムの触媒特性に関する理論的研究

大城　海

北海道大学

2025

Contents

Chapter 1. General Introduction 7
1.1. Heterogeneous Catalysts 8
1.2. Environmental Catalysts 8
1.3. Catalytic Reduction for NO_X 9
1.3.1. Catalytic Poisoning of NH_3-SCR 11
1.3.2. Alkali Metal Poisoning 12
1.3.3. Zeolite for NH_3-SCR 12
1.3.4. Metal Oxide for NH_3-SCR 13
1.3.5. Ce-based Catalysts 14
1.4. Theoretical Study on NH_3-SCR 15
1.5. Machine Learning Force Fields 16
1.6. Purpose of the Tesis 18
1.7. Overview of the Thesis 19
1.8. References 22
Chapter 2. Theoretical Investigation of the Alkali Metal Poisoning Tolerance Mechanism of CeO_2 Containing Fe and H_2SO_4 Additives 28
2.1. Introduction 29
2.2. Computational Details 33
2.3. Results and Discussion 34
2.3.1. Investigation of the Catalytic Surface upon the Inclusion of Additives 34
2.3.2. Projected Density of States 38
2.3.3. Effects of Oxygen Vacancy Formation 41
2.3.4. Alkali Metal Poisoning 48
2.3.5. Alkali Metal Adsorption 50
2.3.6. Charge Density Differences 54
2.3.7. Adsorption of Multiple Potassium Atoms 56
2.4. Conclusion 59
2.5. Supporting Information 61
2.6. References 75
Chapter 3. Constructing Machine-Learning Force Field Describing Oxygen Vacancy on CeO_2 Surfaces 81
3.1. Introduction 82
3.2. Computational Details 85

3.3. Results and Discussion 88
3.3.1. Oxygen Diffusion Pathways 93
3.4. Conclusions 99
3.5. Supporting Information 101
3.6. References 108
Chapter 4 General Conclusion 113
Acknowledgment 117

Chapter 1. General Introduction

1.1. Heterogeneous Catalysts

The conversion of substances through chemical reactions is essential for producing fuels and materials that support our daily lives. Catalysis is a crucial technology for converting compounds under industrially feasible pressure and temperature conditions by providing an energetically favorable reaction pathway to chemical reactions.[1]

Catalysts play a crucial role in reducing activation energy and facilitating chemical reactions, which is vital for efficient energy use in creating a sustainable society. Among them, heterogeneous catalysts are widely used in industrial applications. These catalysts exist in a different phase from the reactants and products, separating them easily after a reaction. This ability to separate is one of the key reasons why heterogeneous catalysts are frequently employed in the synthesis of mass-produced compounds.[2]

1.2. Environmental Catalysts

Since the Industrial Revolution, the production of unwanted waste from chemical processes has significantly increased, becoming a substantial burden on the environment. To address this issue, catalysts are also employed to break down pollutants generated by chemical processes before pollutants are released into the environment. Hence, catalysts are not only used for producing compounds but also for mitigating the environmental impact of industrial activities.

For example, in combustion reactions above 1500 ºC, the reaction of oxygen and nitrogen in the air produces nitrogen oxides (NO_X).[3] When this NO_X coexists with hydrocarbons, photochemical reactions produce oxidants (oxidizing substances, mainly ozone), which cause photochemical smog. As a method to remove NO_X, the causative

agent, from exhaust gases, the selective catalytic reduction method using NH_3 as a reductant is widely used at large thermal power plants. The catalyst consists of active species such as V_2O_5, WO_3, and MoO_3 on a TiO_2 support.

In addition to NO_X, emissions of HC (unburned hydrocarbons) and CO are regulated in gasoline-powered vehicles. Therefore, a three-way catalyst removes these three components from the exhaust gas. In this catalytic reaction, NO acts as an oxidant, while HC and CO act as reductants. The reaction is, therefore, complex and involves a variety of compounds and chemical reactions.

$$\mathrm{NO} + \mathrm{CO} \rightarrow \frac{1}{2}\mathrm{N_2} + \mathrm{CO_2} \quad (1)$$

$$\left(2n + \frac{m}{2}\right)\mathrm{NO} + \mathrm{C}_n\mathrm{H}_m \rightarrow \left(n + \frac{m}{4}\right)\mathrm{N_2} + n\mathrm{CO_2} + \frac{m}{2}\mathrm{H_2O} \quad (2)$$

$$\mathrm{NO} + \mathrm{H_2O} \rightarrow \frac{1}{2}\mathrm{N_2} + \mathrm{H_2O} \quad (3)$$

$$\mathrm{CO} + \mathrm{H_2O} \rightarrow \mathrm{CO_2} + \mathrm{H_2} \quad (4)$$

$$\mathrm{C}_n\mathrm{H}_m + 2n\mathrm{H_2O} \rightarrow n\mathrm{CO_2} + \left(2n + \frac{m}{2}\right)\mathrm{H_2} \quad (5)$$

As the main component of three-way catalysts, a support such as Al_2O_3 with a CeO_2 promoter catalyst and active species such as Rh, Pt, and Pd have been put to practical use.

In addition, the Catalytic Wet Air Oxidation Method decomposes organic compounds from wastewater. Catalysts with transition metals supported on TiO_2 or ZrO_2 are used mainly for this purpose.

1.3. Catalytic Reduction for NO_X

About 60% of the world's electricity generation is provided by coal and natural gas.[4] The combustion of these fossil fuels is accompanied by the formation of NO_X, resulting

in severe air pollution. In recent years, the use of biomass fuels as a sustainable alternative to fossil fuels has also been considered. However, it has been reported that some types of raw materials emit more NO_X than oil,[5] and exhaust gas purification technology will continue to be an essential topic in the catalyst field.

Selective catalytic reduction with Ammonia (NH_3-SCR) is widely used as an efficient way to remove NO_X from exhaust gas. Different types of catalysts used in this SCR system have been commercialized depending on the operating environment. For example, V_2O_5-WO_3 (MoO_3)/TiO_2 catalysts are commercially available for thermal power plants (stationary sources),[6] and CHA-type zeolite catalysts with small pores, such as Cu-SSZ-13, for vehicles with diesel engines (mobile sources).[7,8]

It is also known through years of research that the same catalyst can have different activities depending on the ratio of NO_X species involved in NH_3-SCR.[9,10] In general, NH_3-SCR expressed in the stoichiometry of Eq. (6) is called Standard SCR; in Eq. (7), equal amounts of NO and NO_2 react, which is called Fast SCR because the reaction efficiency can reach 10 times higher than Standard SCR.

$$2NH_3 + 2NO + \frac{1}{2}O_2 \rightarrow 2N_2 + 3H_2O \quad (6)$$

$$2NH_3 + NO + NO_2 \rightarrow 2N_2 + 3H_2O \quad (7)$$

Today's essential topics for deNO_X catalysts include lower active temperatures, more expansive temperature windows, and improved resistance to poisoning by various substances. At the same time, catalyst materials should be less toxic to the environment and less expensive.

For example, exhaust gases contain SO_X,[11,12] alkali/alkaline earth metals,[13,14] phosphorus,[15] and heavy metals,[16] which can poison the active species on the deNO_X catalyst. Therefore, exhaust gases are treated in a desulfurizer or dust collector before

passing through the catalyst, and in the process, the exhaust gas temperature is lowered. The reaction temperature of SCR with V-based catalysts is relatively high, 300 ~ 400 °C, so the lowered temperature exhaust gas must be reheated as it passes over the deNO_X catalyst.[17] For this reason, it has been reported that the entire NH_3-SCR process uses 0.5 % of the energy generated.[18] This means additional fuel is consumed to operate the SCR system, generating extra NO_X and CO_2. Therefore, lowering the temperature of the deNO_X catalyst and expanding the temperature window are essential issues for reducing the environmental impact of the SCR system. Lowering the NO_X reduction temperature also allows for more flexible operation of the SCR system, but there is also a problem specific to the lower temperature. SO_2, a toxic substance to the deNO_X catalysts, precipitates more significantly at low temperatures (LT), so LT-SCR must also acquire resistance to these toxic substances.[19]

1.3.1. Catalytic Poisoning of NH_3-SCR

In exhaust gases, SO_X and fossil fuel-derived metals cause catalyst deactivation by occupying active sites on the catalyst surface or altering active species' redox properties.

SO_2 is often oxidized to SO_3 and SO_4^{2-} on the catalyst, which inhibits the reduction of NO_X by sulfating the active species. It can also form stable ammonium sulfate ($(NH_4)_2SO_4$) and ammonium hydrogen sulfate (NH_4HSO_4) with the reducing agent NH_3, which blocks the active sites and causes catalyst deactivation.

Heavy metals are also known to poison SCR. In particular, metals such as Pb, As, and Zn significantly reduce SCR activity.

1.3.2. Alkali Metal Poisoning

Fossil fuels often contain alkali metals and other metals. These metals are known to cause deactivation of the catalyst by reducing its reducing ability, decreasing surface acidity, and occupying pores. For example, K species occupy Brønsted acid sites on the catalyst surface, reducing acidity.[20] There are two strategies for improving alkali resistance: (1) providing additional acid sites for NH_3 adsorption or (2) separating Alkali trap sites from active sites for the SCR reaction.

Regarding (1), Alkali ions preferentially interact with acidic supports, which helps protect the active sites. For instance, researchers can supply additional acid sites to the catalyst or use an acidic support. Yue et al. reported that by adding CeO_2 to MnO_X/TiO_2, SCR activity was retained due to the additional Lewis acid sites being provided and the amount of NH_3 adsorbed being maintained.[21]

In method (2), alkali metal poisoning is reduced by introducing alkali metal trapping sites in the SCR catalyst that are separate from the active site. Huang et al.[22] reported that hollandite manganese oxide (HMO) has isolated active and Alkali trap sites on the outside and inside of the tunnel structure, respectively. They found that Alkali may spontaneously migrate into the inner tunnel to protect the catalytically active sites, resulting in good alkali resistance. Based on the strong alkali resistance of HMO catalysts, Hu proposed an exchange coordination mechanism,[23] i.e., a mechanism that can exchange alkali metal ions and stabilize them in cavities suitable for their size in the HMO pores.

1.3.3. Zeolite for NH_3-SCR

Three-way catalysts contribute to removing CO, HC, and NO_X from gasoline

vehicles. However, they were unsuitable for diesel engines operating at high air-fuel ratios and emitting large amounts of NO_X.[24] Therefore, ion-exchange zeolite catalysts have attracted attention due to their wide temperature range, but their hydrothermal stability at high temperatures and SO_2 tolerance remain challenging. In addition, zeolite catalysts with large pore structures easily adsorb hydrocarbons produced by incomplete combustion of fuels, leading to the destruction of the framework, so small pore Cu-exchange SSZ-13 and SAPO-34 have attracted much attention in recent years.[25]

1.3.4. Metal Oxide for NH_3-SCR

V_2O_5-WO_3 (MoO_3)/TiO_2 catalysts are currently the most popular metal oxide-based denitration catalysts. However, weak low-temperature activity, narrow temperature windows, high SO_2 to SO_3 oxidation activity, and vanadium toxicity remain challenging.[24]

MnO_X has SCR activity at low temperatures due to its excellent redox properties. On the other hand, it has been reported that pure MnO_X catalysts have too strong oxidizability, resulting in the formation of the byproduct N_2O by NH_3 oxidation, causing a significant reduction in N_2 selectivity.[26] Not only that, SO_2 is also oxidized to SO_3, which is known to poison active sites on the catalyst and cause inactivation of catalytic activity. Modification and substitution with other metals have been investigated to overcome these drawbacks and improve N_2 selectivity and SO_2 tolerance. Studies have also been conducted to improve N_2 selectivity with appropriate support materials.

One of the characteristics of Fe_2O_3-based catalysts is their low price due to their abundant reserves. While they have excellent activity and hydrothermal tolerance at high temperatures, pure Fe_2O_3 catalysts have low activity and a narrow range of active

temperatures.[27] Multi-element substitution has been investigated to improve the low-temperature activity of Fe-based catalysts and surface acidity. Substituting multiple elements has also been considered to improve the redox properties and surface acidity. Metals such as Mn, W, Ce, Ti, V, and Zr are often selected.

CuO is a promising material for NH_3-SCR applications due to its strong redox properties resulting from the change in oxidation number (Cu^{2+}/Cu^{+}). On the other hand, the disadvantages of CuO are its narrow active temperature window and NH_3 oxidation to lead byproduct N_2O.[26]

1.3.5. Ce-based Catalysts

CeO_2 is one of the most abundant rare earth elements in the earth's crust, and its relatively stable price has led to its application in various fields, including catalysis.[28] In addition, the application of CeO_2 for SCR catalysts has been actively explored due to its excellent redox properties related to Ce^{4+}/Ce^{3+} cooperation.[28] The excellent oxygen storage capacity (OSC) of CeO_2 has also attracted attention for its application as an active species in catalysts and its use as a support.[26] On the other hand, a drawback of CeO_2 is its low surface acidity, which prevents efficient adsorption of NH_3. The substitution of transition metals and the addition of oxoacids have been investigated to address this drawback. Since CeO_2 is easily sulfated, SO_2 poisoning also needs to be addressed.[24] CeO_2-based catalysts have excellent activity in the medium to high-temperature range but still have poor low-temperature catalytic activity, which hinders their industrial application.

The excellent activity of CeO_2 for NH_3-SCR at medium to high temperatures is attributed to its oxygen vacancies.[29] Chen et al.[30] proposed from DFT calculations that

the reactive oxygen species O*, produced by the reoxidation of oxygen vacancy by O_2, is necessary for activating NH_3. Chen et al.[31] investigated NO oxidation on CeO_2 surfaces using experiments and calculations and suggested that reactive oxygen species O* contribute to NO oxidation. The NO_2 produced would then contribute to the reduction of NO_X by Fast SCR together with NO. Efforts to improve the low surface acidity of CeO_2, such as the addition of sulfuric acid, have also been investigated.[24] H_2SO_4-doped CeO_2 has been found to have abundant acid sites, Ce^{3+} species, defect sites, and reducibility, resulting in excellent activity.

1.4. Theoretical Study on NH_3-SCR

NH_3-SCR with NO and O_2 is called Standard SCR and is represented by Eq. (6). O_2 has two possible roles under these reaction conditions.

$$2H + \frac{1}{2}O_2 \rightarrow H_2O \quad (8)$$

$$NO + \frac{1}{2}O_2 \rightarrow NO_2 \quad (9)$$

Eq. (8) is the direct oxidation of the reduced surface by O_2, and Eq. (9) is the contribution to the oxidation of NO to NO_2. Chen et al. proposed that the case proceeding in Eq. (8) would be Standard SCR, and the case proceeding in Eq. (9) corresponds to Fast SCR.[30]

Regarding Fast SCR, several studies have proposed that the Fast-SCR stoichiometry (Eq. (7)) is expressed as the sum of Eq. (10) and Eq. (11).[10,32]

$$2NH_3 + 2NO_2 \rightarrow N_2 + H_2O + NH_4NO_3 \quad (10)$$

$$NO + NH_4NO_3 \rightarrow NO_2 + N_2 + 2H_2O \quad (11)$$

Indeed, it is reasonable that Fast SCR goes through Eq. (10), considering that the most

stable NO_3^- absorbed species among the NO_X species is observed under experimental conditions. Under NO_2 conditions, the observed NO and NO_3^- species suggest that the $2NO_2$ in Eq. (10) is disproportionated to NO_3^- and NO^+ along Eq. (12).

$$2NO_2 \rightleftarrows N_2O_4 \rightleftarrows NO+ + NO_3^- \quad (12)$$

Furthermore, it has been experimentally confirmed that NH_4NO_3 produced in Eq. (10) forms N_2O by thermal decomposition.[10] Thus, Eq. (13) is the pathway that produces the byproduct N_2O.

$$NH_4NO_3 \rightarrow N_2O + 2H_2O \quad (13)$$

1.5. Machine Learning Force Fields

Recently, machine learning force fields (MLFF) have attracted attention as a method to bridge the computational cost and accuracy gap between first-principles (FP) calculations and classical force fields. Attempts have been made to apply Machine Learning Force Fields (MLFF), which learn chemical interactions from FP calculations, to long-time simulations or large systems. MLFF can enhance simulations beyond the accuracy of classical force fields across various systems. A feature of MLFF is that patterns are automatically found and learned from the correspondence between structures and energies. Unlike classical force fields, there is no need to explicitly specify the information of chemical bonds in advance.[33]

The most commonly used methods for MLFF applications can be divided into kernel-based and neural network-based methods. Generally, kernel-based methods tend to achieve good prediction accuracy with fewer data points. They are also faster than learning NNs when the data set is small since the optimal parameters can be determined analytically. However, it is disadvantageous for large data sets since analytically

determining the parameters requires the computation of an inverse matrix, the computational cost of which scales by $O(n^3)$ for the number of data, n.[33]

One kernel-based method is the Gaussian Approximate Potential (GAP).[34,35] Similar to high-dimensional neural network potentials (HDNNP) proposed by Behler and Parrinello,[36] it partitions the system of interest into local environments centered on each atom *i* and expresses the energy of the entire system as the contribution from each atom *i*. The trained force field can be applied to systems with different compositions or atomic numbers by decomposing the total energy into contributions from each atom. In addition, for the prediction of the total energy, a smooth cutoff function is applied to the pairwise distance to ensure that the value is not discontinuous as atoms enter or exit the cutoff radius at each local structure.

Constructing machine-learning forcefields presents a challenge due to the significant trial-and-error needed for proper data sampling. Jinnouchi et al. developed a method for on-the-fly forcefield generation that automatically selects training data while performing ab initio molecular dynamics (MD) to tackle this issue. They successfully applied their method to calculate melting points[37] and simulate phase transitions[38], demonstrating its effectiveness for metallic, covalent, and ionic materials. Additionally, their MD simulations of large-scale structures using MLFF achieved speeds three orders of magnitude faster than FP calculations, showcasing the method's usefulness.

Researchers have increasingly applied machine learning force fields (MLFF) to study catalyst reaction mechanisms in recent years. Staub et al. employed neural network potential (NNP) and Artificial Force Induced Reaction (AFIR) methods on homogeneous catalysts.[39] They found that the NNP often predicts incorrect outcomes for the collapsed structures when external forces are applied using the AFIR method. To address this issue,

they demonstrated that they could obtain a reaction pathway network that accurately reproduces the reaction yield from the DFT calculation by using NNP to correct the discrepancies from the DFT calculation for the semi-empirical potential, xTB. Ichino et al. applied universal neural network potentials (NNP) to investigate reaction mechanisms in heterogeneous catalysis.[40] Using a combination of universal NNP and AFIR, they calculated networks of methane oxidation reactions on a huge Pd surface. Their results showed that the trend of activation energy was qualitatively consistent with previously reported DFT data.

1.6. Purpose of the Tesis

Thus, heterogeneous catalysts play an important role, especially in industry. However, because the particles of metals and the oxides that act as catalysts vary in size and shape, elucidating the relationship between catalytic activity and their structure is complex. For example, local structural differences must be considered, such as how multiple atoms are arranged in a solid solution and the presence of defects and adsorbed atoms. Even if we focus on the broader surface structure, a single heterogeneous catalyst can mix several different surface structures.

Therefore, to elucidate the mechanism of catalysis, it is important to model the catalyst surface properly, considering the additives and experimental conditions. However, this task is usually difficult because the more additives there are, the more complex the combination of their arrangements becomes.

In recent years, observing solid surfaces at the atomic level has become possible using a scanning tunneling microscope (STM). However, there are several limitations related to the measurement environment, such as eliminating vibrations and conducting

observations under ultra-high vacuum conditions. Additionally, the types of samples that can be measured are generally restricted to those with conductive properties. This limitation often confines the study to metal oxides widely used as catalyst materials. As a result, the modeling of catalyst surfaces based on experimental observations is quite limited and typically relies on FP calculations to discuss the stability of surface structures.

In Chapter 2, I applied first-principles thermodynamics to model the surface structure based on experimental conditions and investigated its contribution to poisoning resistance.

In Chapter 3, I examined a fast-screening method for various surface structures, including an oxygen vacancy, using a machine-learning force field.

1.7. Overview of the Thesis

Chapter 1 serves as a general introduction. It begins by emphasizing the significance of heterogeneous catalysts and one of their applications: the NH_3-SCR process, which is utilized in environmental catalysis, particularly for exhaust gas purification. The proposed reaction mechanism for NH_3-SCR is also outlined. Additionally, the latter part of the introduction discusses machine learning force fields and neural network potentials.

Chapter 2 is entitled "Theoretical Investigation of the Alkali Metal Poisoning Tolerance Mechanism of CeO_2-Containing Fe and H_2SO_4 Additives". This chapter focuses on understanding the influence of Fe and H_2SO_4 in the ongoing development and improvement of alkali tolerance catalysts. Density functional theory (DFT) calculations were used to investigate the role of Fe and H_2SO_4 in alkali poisoning tolerance. The results showed that potassium species occupy lattice oxygen sites on the CeO_2 surface, inhibiting the formation of Brønsted acid sites and the adsorption of the reducing agent, NH_3. The induced Fe and H_2SO_4 promoted oxygen vacancy formation and generated a

characteristic adsorption site (SO_4/Fe_CeO_2_V_O) for the accumulation of multiple potassium atoms. Thus, the synergistic effect of Fe and H_2SO_4 additives suggested that the NH_3 adsorption sites on the CeO_2 surface were protected from potassium poisoning of the catalyst.

Chapter 3 is entitled "Constructing Machine-Learning Force Fields Describing Oxygen Vacancy on CeO_2 Surfaces". This chapter investigated an efficient database construction method, using the VASP on-the-fly machine learning to train MLFF that accurately describe the properties of complex metal oxide surfaces. Particular focus was placed on the stability of oxygen vacancy and its diffusion to contracts MLFF suitable for simulating various CeO_2 surface structures. The following procedures were considered on-the-fly training approaches for robust MLFF: (1) Start with an unstable structure: Initializing with a more unstable structure resulted in faster convergence of error and improved MLFF accuracy with fewer steps. I trained MLFF on small-slab models (including two or three CeO_2 layers with (100) or (111) facets). After on-the-fly training, the accuracy of MLFF was evaluated on medium slab models with seven different facets. (2) Gradually increasing the temperature: By gradually increasing the temperature of the on-the-fly training run from 300 K to 4000 K, MLFF can capture a wide variety of atomic configurations while maintaining simulation stability. (3) Merging data sets: Merging data sets of training models with different numbers of atoms improved the accuracy of MLFF.

In particular, combining the training data from the three-layer pristine surface model (100-Ce_3L_0V) and the oxygen vacancy model (100-Ce_3L_1V) significantly improved MLFF performance. Further structural optimization and diffusion pathway calculations were performed on pristine and oxygen-vacancy surfaces. MLFF successfully reproduced fundamental diffusion properties comparable to those obtained

with DFT, yielding similar geometry, relative stability, and energy barriers. However, it could not correctly reproduce the energy change when the energy difference was slight (< 0.3 eV). Overall, MLFF effectively captured the potential energy surface of the CeO_2 surface, except for the energy difference below 0.3 eV.

Chapter 5 provides a general summary of this thesis. Specifically, it summarizes the results of applying conventional first-principles calculations and machine-learning force-field-based simulation methods to cerium oxide materials used as catalysts in NH_3-SCR. It provides insights into poisoning tolerance and redox properties.

1.8. References

(1) Ib Chorkendorff, J. W. N. Concepts of Modern Catalysis and Kinetics. Wiley-VCH Verlag GmbH & Co. KGaA, **2003**, Weinheim, FRG.

(2) Jens K. Nørskov, F. S., Frank Abild-Pedersen, Thomas Bligaard. Fundamental Concepts in Heterogeneous Catalysis. John Wiley & Sons, Inc., **2014**, Hoboken, NJ.

(3) Eiichi Kikuchi, Y. I., Kohichi Segawa, Akio Tada, Hideshi Hattori. 新版 新しい触媒化学. SANKYO SHUPPAN Co., Ltd., **2013**, Tokyo, JP.

(4) Pioro, I.; Duffey, R. B.; Kirillov, P. L.; Pioro, R.; Zvorykin, A.; Machrafi, R. Current Status and Future Developments in Nuclear-Power Industry of the World. *Journal of Nuclear Engineering and Radiation Science* **2019**, *5*.

(5) Ozgen, S.; Cernuschi, S.; Caserini, S. An overview of nitrogen oxides emissions from biomass combustion for domestic heat production. *Renewable and Sustainable Energy Reviews* **2021**, *135*.

(6) Inomata, Y.; Hata, S.; Mino, M.; Kiyonaga, E.; Morita, K.; Hikino, K.; Yoshida, K.; Kubota, H.; Toyao, T.; Shimizu, K.-i.; et al. Bulk Vanadium Oxide versus Conventional V_2O_5/TiO_2: NH_3–SCR Catalysts Working at a Low Temperature Below 150 °C. *ACS Catalysis* **2019**, *9*, 9327-9331.

(7) Villamaina, R.; Liu, S.; Nova, I.; Tronconi, E.; Ruggeri, M. P.; Collier, J.; York, A.; Thompsett, D. Speciation of Cu Cations in Cu-CHA Catalysts for NH_3-SCR: Effects of SiO_2/AlO_3 Ratio and Cu-Loading Investigated by Transient Response Methods. *ACS Catalysis* **2019**, *9*, 8916-8927.

(8) Jabłońska, M. Review of the application of Cu-containing SSZ-13 in NH_3-SCR-DeNO_X and NH_3-SCO. *RSC Adv* **2022**, *12*, 25240-25261.

(9) Wang, X.; Du, X.; Yang, G.; Xue, J.; Chen, Y.; Zhang, L. Chemisorption of NO_2 on V-Based SCR Catalysts: A Fundamental Study toward the Mechanism of "Fast SCR" Reaction. *The Journal of Physical Chemistry C* **2019**, *123*, 20451-20458.

(10) Liu, C.; Malta, G.; Kubota, H.; Kon, K.; Toyao, T.; Maeno, Z.; Shimizu, K.-i. In Situ/Operando IR and Theoretical Studies on the Mechanism of NH_3–SCR of NO/NO_2 over H–CHA Zeolites. *The Journal of Physical Chemistry C* **2021**, *125*, 13889-13899.

(11) Liu, Z.; Shan, Y.; Han, S.; Fu, Y.; Du, J.; Sun, Y.; Shi, X.; Yu, Y.; He, H. Insights into SO_2 Poisoning Mechanisms of Fresh and Hydrothermally Aged Cu-KFI Catalysts for NH_3-SCR Reaction. *Environ Sci Technol* **2023**, *57*, 4308-4317.

(12) Cai, Y.; Zhang, B.; Yu, H.; Ji, X.; Sun, J.; Wang, X.; Qian, Q.; Li, L.; Liu, A.; Tan, W.; et al. Shielding ceria based catalysts from SO_2 poisoning in NH_3-SCR reaction: Modification effect of acid metal oxides. *Applied Catalysis B: Environmental* **2024**, *342*.

(13) Wu, P.; Tang, X.; He, Z.; Liu, Y.; Wang, Z. Alkali Metal Poisoning and Regeneration of Selective Catalytic Reduction Denitration Catalysts: Recent Advances and Future Perspectives. *Energy & Fuels* **2022**, *36*, 5622-5646.

(14) Guan, B.; Chen, J.; Guo, J.; Liu, Z.; Zheng, C.; Zhou, J.; Su, T.; Zhang, Y.; Yuan, Y.; Dang, H.; et al. Study on Effect and Mechanism of Alkaline Earth Metal Poisoning on Cu/SSZ-13 Catalysts for Selective Catalytic Reduction of NO_X with NH_3. *Industrial & Engineering Chemistry Research* **2023**, *62*, 9662-9672.

(15) Guo, A.; Xie, K.; Lei, H.; Rizzotto, V.; Chen, L.; Fu, M.; Chen, P.; Peng, Y.; Ye, D.; Simon, U. Inhibition Effect of Phosphorus Poisoning on the Dynamics and Redox of Cu Active Sites in a Cu-SSZ-13 NH_3-SCR Catalyst for NO_X Reduction. *Environ Sci Technol* **2021**, *55*, 12619-12629.

(16) Wang, S.; Liu, J.; Jin, Z.; Guo, S.; Cheng, D.; Deng, J.; Zhang, D. Gas-Phase Regeneration of Metal-Poisoned V_2O_5-WO_3/TiO_2 NH_3-SCR Catalysts via a Masking and Reconstruction Strategy. *Environ Sci Technol* **2024**.

(17) Xu, G.; Guo, X.; Cheng, X.; Yu, J.; Fang, B. A review of Mn-based catalysts for low-temperature NH_3-SCR: NO_X removal and H_2O/SO_2 resistance. *Nanoscale* **2021**, *13*, 7052-7080.

(18) Graus, W. H. J.; Worrell, E. Effects of SO_2 and NO_X control on energy-efficiency power generation. *Energy Policy* **2007**, *35*, 3898-3908.

(19) Guo, K.; Ji, J.; Song, W.; Sun, J.; Tang, C.; Dong, L. Conquering ammonium bisulfate poison over low-temperature NH_3-SCR catalysts: A critical review. *Applied Catalysis B: Environmental* **2021**, *297*.

(20) Jiang, Y.; Gao, X.; Zhang, Y.; Wu, W.; Luo, Z.; Cen, K. Effect of KCl on the selective catalytic reduction of NO with NH_3 over vanadia‐based catalysts for biomass combustion. *Environmental Progress & Sustainable Energy* **2013**, *33*, 390-395.

(21) Peng, Y.; Li, J.; Si, W.; Li, X.; Shi, W.; Luo, J.; Fu, J.; Crittenden, J.; Hao, J. Ceria promotion on the potassium resistance of MnO_X/TiO_2 SCR catalysts: An experimental and DFT study. *Chemical Engineering Journal* **2015**, *269*, 44-50.

(22) Huang, Z.; Gu, X.; Wen, W.; Hu, P.; Makkee, M.; Lin, H.; Kapteijn, F.; Tang, X. A "Smart" Hollandite $DeNO_X$ Catalyst: Self-Protection against Alkali Poisoning. *Angew Chem Int Ed Engl* **2013**, *52*, 660-664.

(23) Hu, P.; Huang, Z.; Gu, X.; Xu, F.; Gao, J.; Wang, Y.; Chen, Y.; Tang, X. Alkali-Resistant Mechanism of a Hollandite $DeNO_X$ Catalyst. *Environ Sci Technol* **2015**, *49*, 7042-7047.

(24) Han, L.; Cai, S.; Gao, M.; Hasegawa, J. Y.; Wang, P.; Zhang, J.; Shi, L.; Zhang, D. Selective Catalytic Reduction of NO_X with NH_3 by Using Novel Catalysts: State of the Art and Future Prospects. *Chem Rev* **2019**, *119*, 10916-10976.

(25) Wang, X.; Xu, Y.; Zhao, Z.; Liao, J.; Chen, C.; Li, Q. Recent progress of metal-exchanged zeolites for selective catalytic reduction of NO_X with NH_3 in diesel exhaust. *Fuel* **2021**, *305*.

(26) Chen, W.; Zou, R.; Wang, X. Toward an Atomic-Level Understanding of the Catalytic Mechanism of Selective Catalytic Reduction of NO_X with NH_3. *ACS Catalysis* **2022**, *12*, 14347-14375.

(27) Yuan, L.; Hu, P.; Hu, B.; Han, J.; Ma, S.; Yang, F.; Volinsky, A. A. Metallic and non-metallic components and morphology of iron-based catalytic effects for selective catalytic reduction performance: A systematic review. *Molecular Catalysis* **2023**, *541*.

(28) Montini, T.; Melchionna, M.; Monai, M.; Fornasiero, P. Fundamentals and Catalytic Applications of CeO_2-Based Materials. *Chem Rev* **2016**, *116*, 5987-6041.

(29) Chung, C.-H.; Tu, F.-Y.; Chiu, T.-A.; Wu, T.-T.; Yu, W.-Y. Critical Roles of Surface Oxygen Vacancy in Heterogeneous Catalysis over Ceria-based Materials: A Selected Review. *Chemistry Letters* **2021**, *50*, 856-865.

(30) Chen, W.; Xu, S. Unraveling the Complete Mechanism of the NH_3-Selective Catalytic Reduction of NO over CeO_2. *ACS Catalysis* **2023**, *13*, 15481-15492.

(31) Chen, W.; Wang, X.; Xu, S. Investigation of intrinsic catalytic mechanism for NO oxidation to NO_2 in CeO_2 used for NO removal. *Chemical Engineering Journal* **2023**, *460*.

(32) Nova, I.; Ciardelli, C.; Tronconi, E.; Chatterjee, D.; Bandl-Konrad, B. NH_3–NO/NO_2 chemistry over V-based catalysts and its role in the mechanism of the Fast SCR reaction. *Catalysis Today* **2006**, *114*, 3-12.

(33) Unke, O. T.; Chmiela, S.; Sauceda, H. E.; Gastegger, M.; Poltavsky, I.; Schutt, K. T.; Tkatchenko, A.; Muller, K. R. Machine Learning Force Fields. *Chem Rev* **2021**, *121*, 10142-10186.

(34) Bartok, A. P.; Payne, M. C.; Kondor, R.; Csanyi, G. Gaussian approximation potentials: the accuracy of quantum mechanics, without the electrons. *Phys Rev Lett* **2010**, *104*, 136403.

(35) Klawohn, S.; Darby, J. P.; Kermode, J. R.; Csanyi, G.; Caro, M. A.; Bartok, A. P. Gaussian approximation potentials: Theory, software implementation and application examples. *J Chem Phys* **2023**, *159*.

(36) Behler, J.; Parrinello, M. Generalized Neural-Network Representation of High-Dimensional Potential-Energy Surfaces. *Phys Rev Lett* **2007**, *98*, 146401.

(37) Jinnouchi, R.; Karsai, F.; Kresse, G. On-the-fly machine learning force field generation: Application to melting points. *Phys Rev B* **2019**, *100*.

(38) Jinnouchi, R.; Lahnsteiner, J.; Karsai, F.; Kresse, G.; Bokdam, M. Phase Transitions of Hybrid Perovskites Simulated by Machine-Learning Force Fields Trained on the Fly with Bayesian Inference. *Phys Rev Lett* **2019**, *122*, 225701.

(39) Staub, R.; Gantzer, P.; Harabuchi, Y.; Maeda, S.; Varnek, A. Challenges for Kinetics Predictions via Neural Network Potentials: A Wilkinson's Catalyst Case. *Molecules* **2023**, *28*.

(40) Ichino, T.; Nabata, H.; Matsumoto, K.; Hasegawa, T.; Maeda, S. Systematic and unbiased pathway exploration by artificial force application to a generic neural network potential. *ChemRxiv* **2024**.

Chapter 2. Theoretical Investigation of the Alkali Metal Poisoning Tolerance Mechanism of CeO_2 Containing Fe and H_2SO_4 Additives

2.1. Introduction

Nitrogen oxides (NO_X) released from stationary and mobile sources is one of the main causes of air pollution. To remove NO_X from exhaust gas, the selective catalytic reduction (SCR) with ammonia (NH_3-SCR) is a powerful technique, wherein V_2O_5/TiO_2 catalysts doped with WO_3 or MoO_3 are commonly employed as deNO_X catalysts.[1] Extensive works have been done to understand the NH_3-SCR mechanism. It is commonly accepted that there are two typical SCR reaction mechanisms over metal oxide catalysts, Eley-Rideal (E-R) mechanism and Langmuir-Hinshelwood (L-H) mechanism as shown in Scheme 1.[1] In the E-R mechanism, NH_3 molecules are adsorbed onto LA or BA acid sites, leading to the formation of NH_3/NH_4^+ species. These species are subsequently oxidized by high-valent redox sites, resulting in the formation of active NH_2 species. The adsorbed NH_2 or NH_3 species then react with gaseous NO, forming intermediate NH_2NO/NH_3NO species, which further decompose into N_2 and H_2O. Meanwhile, the high-valent redox sites undergo reduction to a lower valence state, but they can be reoxidized by O_2, completing the redox cycle. In the L-H mechanism, NH_3 molecules adsorb on LA or BA acid sites, leading to the formation of NH_4^+ species. Simultaneously, NO is oxidized by high-valent redox sites, generating active bidentate nitrate/bridged nitrate/monodentate nitrite species. These species then react with NH_4^+ to form NH_4NO_2/NH_4NO_3, which subsequently decompose into N_2 and H_2O. Similar to the E-R mechanism, the high-valent redox sites undergo reduction to a lower valence state, but they can be reoxidized by O_2, completing the redox cycle.

Eley-Rideal (E-R)

$$LA + NH_3(g) \rightarrow LA\text{-}NH_3 \quad (1)$$
$$LA\text{-}NH_3 + NO(g) \rightarrow N_2(g) + H_2O(g) + H\text{-}O_{lat} \quad (2)$$

Langmuir-Hinshelwood (L-H)

$$BA + NH_3(g) \rightarrow BA\text{-}NH_3 \quad (3)$$
$$BA\text{-}NH_3 + NO_2^* \rightarrow N_2(g) + 2H_2O(g) \quad (4)$$

Scheme 1. Representative chemical equations for the Eley-Rideal and the Langmuir-Hinshelwood mechanism. * indicates metal oxide surface, LA and BA indicate Brønsted acid site and Lewis acid site, respectively.

However, there is still a serious drawback left for commercial deNO_X catalysts, that is deactivation by chemical compounds, such as H_2O, SO_X, alkali metals, alkaline-earth metals, and heavy metals. For example, biomass fuels, which are an alternative to fossil fuels, are rich in alkali metals,[2] and so their usage can lead to the deactivation of deNO_X catalysts. Therefore, the demand for deNO_X catalysts with superior alkali tolerances has dramatically increased with the ongoing development of biomass fuels.

The mechanism responsible for the poisoning of commercial V_2O_5/TiO_2 catalysts by alkali metals has been studied experimentally for many years.[3-6] As shown in Scheme 1, no matter which mechanism that SCR follows, NH_3 molecule adsorption is the initial and important step to generate active NH_X species to react with NO or NO_2 molecules. Therefore, a generally recognized deactivation mechanism involves the adsorption of alkali metals on the catalytic surface, which decreases the number of available Brønsted acid (BA) sites and reduces NH_3 adsorption. Indeed, Chen et al. investigated the

poisoning mechanism associated with nano V_2O_5-WO_3/TiO_2 catalysts using major alkali and alkaline earth metals,[5] and they found that the addition of alkali metals significantly decreased the amount and stability of the BA sites, which hindered the reducibility of the vanadium species. They also clarified that the degree of poisoning by alkali and alkaline-earth metals corresponded to their order of basicity, as follows: K > Na > Ca > Mg. In addition, Kohg et al. studied the deactivation mechanism of V_2O_5-WO_3/TiO_2 catalysts using various potassium compounds, including KCl, K_2O, and K_2SO_4.[7] Their results showed that the number and stability of BA and Lewis acid (LA) sites decreased after alkali metal poisoning. Surprisingly, the poisoning effect of K_2SO_4 was smaller than those of KCl and K_2O, indicating that while V–OH was poisoned, resulting in the generation of V–OK, the SO_4^{2-} species were able to provide new –OH groups as adsorption sites for NH_3. Their results also suggested that H_2SO_4 could improve alkali tolerance of the catalyst by promoting the adsorption of NH_3 at the H_2SO_4 sites.

DFT calculations are also performed to gain atomic-level insight into catalyst poisoning.[8-11] As an example study, Lyu et al. compared the poisoning effects of Na and K on the NH_3-SCR reaction catalyzed by α-Fe_2O_3.[12] Their results indicated that the adsorption of K was stronger than that of Na, and the adsorption of NH_3 at the LA sites was not affected by K or Na poisoning, whereas that at the BA site was directly inhibited. In another study, Jiang et al. investigated the poisoning effects of KCl, K_2O, and K_2SO_4 on Ce/TiO_2 catalysts using both experimental and theoretical methods.[13,14] They found that the introduction of these potassium species significantly decreased the degree of NH_3 adsorption, the catalyst reducibility, and the concentration of chemisorbed oxygen on the Ce/TiO_2 surface. However, it should be noted that although the adsorption of NO on the catalyst surface was promoted, some of the adsorbed NO_X species were not reactive.

To date, many strategies have been proposed to improve the alkali tolerance of deNO_X catalysts. For example, the introduction of additional acid sites for alkali metal binding can prevent poisoning whilst also protecting the active sites for SCR, thereby maintaining the catalytic activity.[15] In this context, Zhou et al. developed $H_2SO_4/V_2O_5/CeO_2$ catalysts that exhibited alkali tolerance and studied the mechanisms of alkali poisoning.[16] More specifically, Raman measurements showed a band corresponding to $KHSO_4$ and revealed that the SO_4 species present on the catalyst surface exhibit preferential bonding to K, acting as a sacrificial site. In contrast to the results of Kohg et al.,[7] these results suggest that H_2SO_4 could protect other NH_3 adsorption sites from alkali poisoning by preferentially trapping K, thereby maintaining a suitable NO_X conversion.

Recently, Zhang and coworkers reported a $Fe/H_2SO_4/CeZr$ catalyst with a high alkali tolerance and NO_X conversion.[17] As expected, the addition of H_2SO_4 to the CeZr catalyst significantly increased the NO_X conversion, while also resulting in a moderate alkali tolerance. Based on previous research, it was proposed that H_2SO_4 can potentially promote the SCR reaction by acting as an adsorption site for NH_3 or by acting as a sacrificial site for alkali metals.[16] However, the incorporation of Fe into CeZr did not improve the conversion or poisoning tolerance of this catalyst, Fe substitution into the $H_2SO_4/CeZr$ system further improved the alkali tolerance while maintaining a high NO_X conversion. Moreover, the amount of Fe added was significantly lower than the quantity of K (i.e., approximately one-sixth). Despite these advances, the mechanisms responsible for the excellent alkali metal tolerance observed following the addition of small amounts of Fe remained unclear. Previously, ammonia temperature-programmed reduction experiments combined with mass spectrometry (NH_3-TPD-MS) revealed that K poisoning reduced the adsorption of NH_3 by $H_2SO_4/CeZr$ and $Fe/H_2SO_4/CeZr$ catalysts,

indicating a reduction in the number of acid sites.[17] In addition, H_2-TPR suggested that Fe/H_2SO_4/CeZr was more reductive than H_2SO_4/CeZr. However, the effects of Fe and H_2SO_4 on the catalyst structure and the K adsorption sites of Fe/H_2SO_4/CeZr catalysts have yet to be clarified.

Thus, the aim of the current study is to carry out a theoretical investigation of the alkali metal poisoning tolerance mechanism of CeZr containing Fe and H_2SO_4 additives. More specifically, using density functional theory (DFT) calculations, the surface structures of catalysts containing Fe/H_2SO_4 are investigated along with their synergistic effects on the adsorption of multiple alkali metals. In addition, the role of oxygen vacancies (V_O) on the catalytic surface is evaluated in terms of their effect in promoting alkali tolerance.

2.2. Computational Details

DFT calculations were performed under periodic boundary conditions using the Vienna Ab initio Simulation Package (VASP) version 5.4.1.[18,19] The PAW method[20,21,22] was adopted for calculations with spin polarization and van der Waals corrections (DFT-D3).[23] The Perdew–Burke–Ernzerhof (PBE) exchange-correlation functional was used for calculations within the generalized gradient approximation (GGA).[24] A (1 × 1 × 1) Gamma mesh k-points grid was adopted for Brillouin zone sampling, and a cutoff energy of 400 eV was used. The strong on-site Coulombic interactions of the Ce_{4f} states were corrected using the Hubbard *U* term method (DFT+U), and 5.0 eV was used for $U_{effective}$ (= $U - J$).[25] A crystal structure of bulk CeO_2 was obtained from the Materials Project

database.[26] The calculated lattice constant was 5.42 Å, which is consistent with the computational value of 5.38 Å[27] and the experimental value of 5.41 Å[28]. As shown in Figure 1, the CeO_2(111) surface, which consists of nine layers, was used for the slab model, wherein the bottom three layers were fixed. The adsorption behavior of K was theoretically studied to characterize the alkali metal poisoning. Charge density differences and projected densities of states (PDOS) were calculated using VASPKIT[29] and visualized using VESTA.[30]

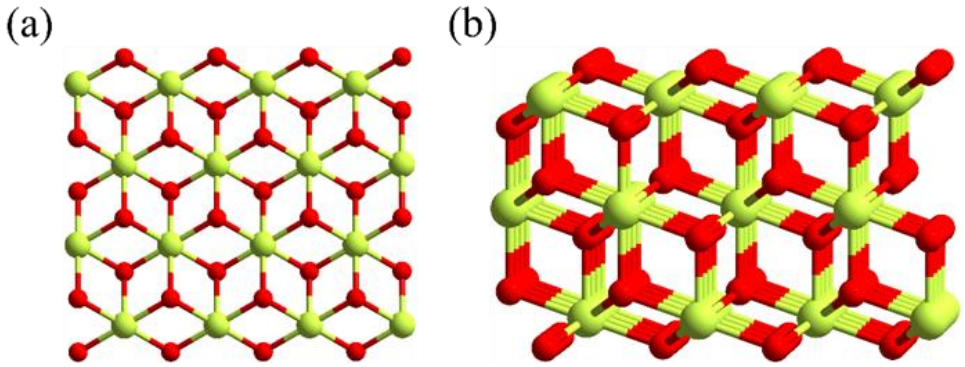


Figure 1. (a) Top view of the upper 3 layers. (b) Side view of the whole slab model. The light green and red colors indicated Ce and O atoms, respectively.

2.3. Results and Discussion

2.3.1. Investigation of the Catalytic Surface upon the Inclusion of Additives

Initially, the effects of Fe and H_2SO_4 addition on the properties of the CeZr catalyst were investigated. According to the experimental X-ray diffraction (XRD) results,[17] No diffraction peak of ZrO_2, FeO_X, and K components was observed and the largest intensity

in Raman spectra for catalyst surface is a symmetric breathing mode of the oxygen atoms around cerium atoms. These experimental results indicate that our CeZr catalyst surface is dominated by the (111) facet of CeO_2. Furthermore, the experimental results reported by Liu *et. al*.[31] revealed similar trend in the activity changes of CeO_2 and CeZr against alkali-poisoning with sulfated compounds. The ability against alkali-poisoning was enhanced by introducing sulfated compounds into CeO_2 and CeZr. Therefore, I used "$Fe/H_2SO_4/CeO_2$" instead of "Fe/H_2SO_4/CeZr" in the following text. In addition, XPS showed that Fe^0 was not present in the system, indicating that the Fe species were atomically dispersed.[17] Hence, the computational model of the catalyst was represented by the $CeO_2(111)$ surface, while that of the Fe-doped CeO_2 catalyst was represented by the Fe_$CeO_2(111)$ surface, where one of the lattice Ce atoms was replaced by an Fe atom.[32,33] Since this replacement could affect the stoichiometry of the surface, I also examined the V_O formation[34] to keep neutrality and its effect on the K poisoning.

Figure 2 shows the optimized geometries of the Fe- and H_2SO_4-modified $CeO_2(111)$ surfaces, where each Ce atom coordinates with seven oxygen atoms on the outermost surface, and the length of the optimized Ce–O_{lat} (lattice oxygen) bond is 2.36 Å. As shown in Figure 2b, Fe substitution causes a V_O-like structure and yields two characteristic O_{lat} atoms with shorter Ce–O_{lat} bonds (2.20 Å) compared to the typical Ce–O_{lat} bonds around the Fe sites. These structural changes can be attributed to an imbalance in the oxidation states of Ce, as the number of closest oxygen atoms on the outermost surface was seven for Ce and four for Fe. The calculated geometric changes are consistent with the experimental XPS results, wherein Fe doping induces mixed-valence states of Ce^{3+} and Ce^{4+}.[35] It was also deduced that the magnetic properties were enhanced by doping with Fe; the spin multiplicities of the $CeO_2(111)$ and Fe_$CeO_2(111)$ surfaces were singlet and

quintet, respectively. The presence of such unpaired electrons is expected to increase the catalytic activity or poisoning tolerance by enhancing the reactivity around the Fe sites.

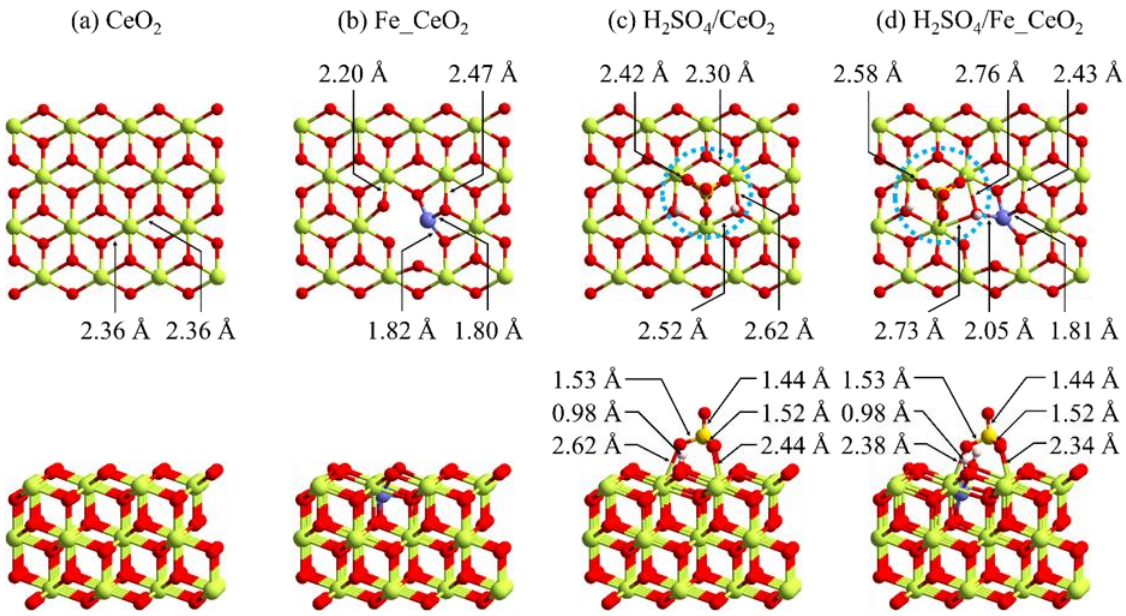


Figure 2. Top and right-side views of (a) CeO_2: the pristine CeO_2(111) surface, (b) Fe_CeO_2: the Fe-doped CeO_2(111) surface, (c) H_2SO_4/CeO_2: the H_2SO_4-modified CeO_2(111) surface, and (d) H_2SO_4/Fe_CeO_2(111): the Fe-doped H_2SO_4-modified CeO_2(111) surface. The dashed circles indicate the position of H_2SO_4. The light green, red, dark blue, yellow, and white colors indicated Ce, O, Fe, S and H atoms, respectively.

Although H_2SO_4 has been widely used as a proton source for metal oxide surfaces,[36,37] the effect of adsorbed H_2SO_4 on metal oxides is not well understood. By screening the possible Ce, Fe, and O sites for H_2SO_4 adsorption with different orientations and for the presence of H^+ adjacent to SO_4 (Figures S1 and S2), the most stable structures were obtained, as shown in Figures 2c and 2d. The adsorption energy of the H_2SO_4 molecules was obtained using equation (1).

$$\Delta E_{\text{ads}} = E_{\text{H}_2\text{SO}_4@\text{Surface}} - E_{\text{Surface}} - E_{\text{H}_2\text{SO}_4} \quad (1)$$

As shown in Figures 2c and 2d, the H_2SO_4 molecule was strongly bound to the CeO_2 and Fe_CeO_2 surfaces. More specifically, ΔE_{ads} (eV) values were calculated to be in the order of: H_2SO_4 (−0.55 eV) > HSO_4^- + H^+ (−1.95 eV) > SO_4^{2-} + 2H^+ (−2.37 eV) for the CeO_2 surface in the absence of additives, thereby indicating that the adsorption of negatively charged compounds is energetically favorable on Ce sites (Figures S1a, S1d, and S1e). In addition, the most stable adsorption structure of H_2SO_4 on the Fe_CeO_2 surface is shown in Figure 2d. This structure possesses a ΔE_{ads} of −2.92 eV, and so it was used to investigate the effect of K poisoning, as described in a later section. The meta-stable geometries shown in Figures S1e and S1f indicate that the protons present on the surface are most stable when they are close to a SO_4 site and at a distance of 1.87 Å from the oxygen atom of sulfuric acid (O_{sul}). This implies that interactions, such as hydrogen bonds, could also contribute to stabilizing the adsorption of SO_4. Thus, H_2SO_4 donates protons (H^+) to the surface, and the remaining SO_4 interacts with three Ce atoms to form a sulfated CeO_2 surface (Figure 2c). This result is consistent with the conclusion of a previous experimental study[38] that H_2SO_4 behaves as a proton resource and increases the number of BA sites. The remaining SO_4 therefore acts as a Brønsted/Lewis base and functions as a K^+ adsorption site.

The lengths of the three Ce–O_{sul} bonds of the H_2SO_4/CeO_2(111) species were determined to be 2.42, 2.44, and 2.62 Å, respectively. Kuczkowski et al. reported two S=O_{sul} double bonds and two S–O_{sul} single bonds exist in the H_2SO_4 molecule, with bond lengths of 1.42 and 1.57 Å, respectively.[39] As shown in Figures 2c and 2d, the three S–O_{sul} bonds adjacent to Ce measure 1.52–1.53 Å in length, which is close to the length of

the S–O_{sul} bond (1.57 Å) in a H_2SO_4 molecule.[39] The S=O_{sul} double bond in the adsorbed SO_4 is also lengthened, and this can be attributed to the strong interaction between Ce and O_{sul}. As a result, three equivalent bonds close to the length of an S–O_{sul} bond are generated. By contrast, the remaining S–O_{sul} bond in the adsorbed SO_4 was found to measure 1.44 Å, which is close to the length of the S=O bond (1.42 Å) in the H_2SO_4 molecule (Figures 2c and 2d).[39] Additionally, the calculated value of the H–O_{lat} bond length and the experimental value of the H–O_{sul} bond length were almost identical (i.e., 0.97 and 0.98 Å, respectively; Figure 2c).[39] For the O_{lat} around the SO_4, Figure 2c shows that the protonated O_{lat} sites around the adsorbed SO_4 species exhibit longer Ce–O_{lat} bonds (2.52–2.62 Å) compared to typical Ce–O_{lat} bonds (2.36 Å). Similarly, the adsorbed SO_4 species considerably extrude the protonated O_{lat} sites to the Fe side on the Fe_CeO_2 surface (Figure 2d) because of the higher basicity of O_{sul} close to the surface. As a result, the protonated O_{lat} possesses the longest Ce–O_{lat} bond lengths (2.73–2.76 Å) among the various modified CeO_2 surface models examined herein.

2.3.2. Projected Density of States

The PDOS was calculated to analyze the effects of Fe and H_2SO_4 on the electronic structure of the CeO_2 surface. However, it is difficult to compare the energies of each particular system owing to their different stoichiometries. Based on previous literature,[40] the PDOS energy was initially shifted according to the state of the atom that is not strongly affected by the presence of an additive. Thus, Ce 5s, −33.5 eV was selected as the reference first, and the Fermi level was set to zero (Figure S3). Figure 3 shows the PDOS of the Ce and O atoms on the surface adjacent to H_2SO_4 or Fe; the positions of the selected

Ce and O atoms used for the PDOS are shown in Figure S4. As presented in Figure 3a, the occupied states peaks at 0 ~ –4 eV correspond to Ce 4*f* and O 2*p*, while the unoccupied state peak at 2 eV corresponds to the Ce 4*f* state. The gap between O 2*p*–Ce 4*f*, 2.29 eV is close to the value of ~2.0 eV given by Maurício et al.[41] In terms of the Fe_CeO_2 (Figure 3b), H_2SO_4/CeO_2 (Figure 3c), and H_2SO_4/Fe_CeO_2 (Figure 3d) surfaces, the PDOS of all Ce atoms was found to be comparable to the PDOS of the Ce atoms of the pristine surface. For the surface with substituted Fe, a sharp peak between −4 and −5 eV was observed, and no peak was found close to the band gap (Figures 3b and 3d). The PDOS of the O_{lat} species around the Fe or H_2SO_4 species are presented as O_{lat_near}, while those of the O_{lat} species far from the Fe or H_2SO_4 species are shown in O_{lat_far}. From Figures. 3b and 3d, it can be seen that O_{lat_near} has a larger density of states close to the band gap compared to the one of O_{lat_far}, implying that Fe substitution promote the surrounding O_{lat} active, such as the formation of V_O. As presented in Figure 3c, O_{lat_near} shows a larger PDOS close to the band gap than O_{lat_far}, thereby suggesting that H_2SO_4 activates the surrounding O_{lat} species. By contrast, O_{sul} exhibits a major peak at a lower energy level, i.e., between −3 and −1 eV.

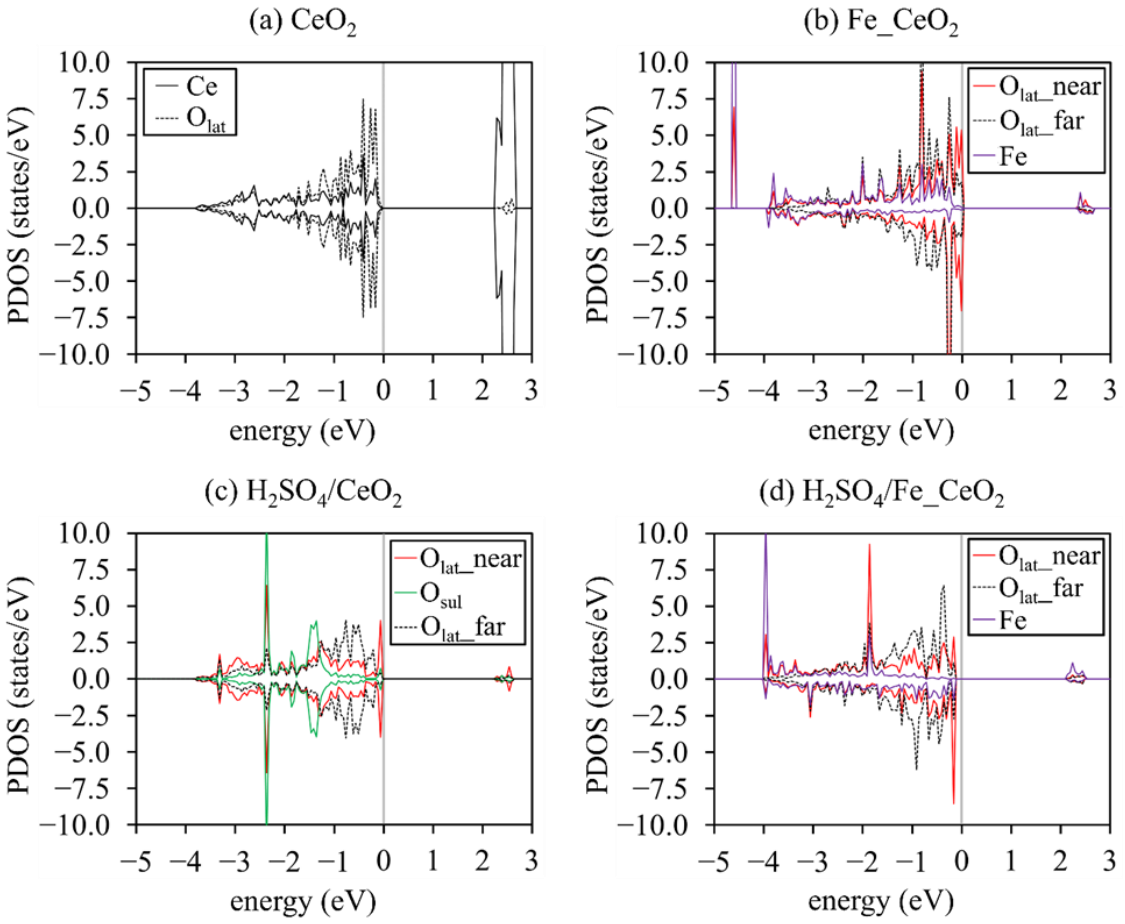


Figure 3. PDOS for the (a) pristine CeO_2(111) surface, (b) Fe-modified CeO_2(111) surface, (c) H_2SO_4-modified CeO_2(111) surface, and (d) H_2SO_4- and Fe-modified CeO_2(111) surface. The Fermi level, E_F was set to 0 eV. The positions of the selected Ce and O atoms used for the PDOS are shown in Figure S4. The lines in positive and negative areas indicate spin-up and spin-down states, respectively.

As the Ce based catalysts exhibit unique catalytic activities as the result of the involvement of the characteristic highly localized 4*f* state, the detailed changes in 4*f* states of Ce atoms induced by additives Fe and H_2SO_4 were analyzed. The PDOS of 4*f* states of Ce atoms nearby Fe and H_2SO_4 were plotted and summarized in Figure S5. It was shown

that the 4f state distributes from 0 eV to −2 eV nearby Fermi level. With the introduction of Fe atoms, a strong peak of 4*f* states of Ce appears near Fermi level as seen in Figure S5b. The imbalance oxidation state between Ce and Fe atoms results in changes in coordination number of Ce and O, and generates V_O-like structure and therefore spin multiplicities (the number of single electrons) changes. The induced single electrons are partially localized at 4*f* states of Ce near Fermi level, which may contribute to unique catalytic activity for NO_X redox. The mechanism of NO_X redox is out scope of this work and will not be discussed here. With both induced H_2SO_4 and Fe, the structure nearby Ce atom doesn't change too much as shown in Figure 2c. The induced V_O-like geometry was refilled by O_{lat} neighboring H_2SO_4, therefore no obvious changes of 4*f* states of Ce atoms.

2.3.3. Effects of Oxygen Vacancy Formation

The V_O formation process was subsequently investigated because CeO_2 is known to possess an excellent oxygen storage capacity.[42] According to the experimental results obtained by Zhang et al.,[43] V_O can be re-oxidized by O_2 molecules to form reactive adsorbed oxygen species, and as a result, the redox properties and catalytic activity are improved. A generally accepted mechanism of V_O formation during the NH_3-SCR process is via the desorption of an adsorbed proton in the form of H_2O_{lat}.[43-45] However, few studies have compared whether V_O is formed via H_2O desorption or directly via O_2 desorption in the presence of protons adsorbed on CeO_2 surface. Therefore, the V_O formation process associated with O_2 desorption (2), which represents the direct desorption of O_{lat}, was compared with the desorption of H_2O (4), wherein$\Delta E_{\mathrm{f}}^{\mathrm{O_2}}$ and $\Delta E_{\mathrm{f}}^{\mathrm{H_2O}}$ indicate the energy of V_O formation in each pathway.

$$\mathrm{O_{lat}} \rightleftarrows \mathrm{V_O} + \frac{1}{2}\mathrm{O_2(g)}, \quad (2)$$

$$\Delta E_{\mathrm{f}}^{\mathrm{O_2}} = E_{\mathrm{V_O}} + \frac{1}{2}E_{\mathrm{O_2(g)}} - E_{\mathrm{O_{lat}}}, \quad (3)$$

$$2\mathrm{H_O_{lat}} \rightleftarrows \mathrm{V_O} + \frac{1}{2}\mathrm{H_2O(g)}, \quad (4)$$

$$\Delta E_{\mathrm{f}}^{\mathrm{H_2O}} = E_{\mathrm{V_O}} + E_{\mathrm{H_2O(g)}} - E_{\mathrm{2H_O_{lat}}}, \quad (5)$$

where $E_{\mathrm{O_{lat}}}$, $E_{\mathrm{V_O}}$, and $E_{\mathrm{2H_O_{lat}}}$ are the energies of the surface without V_O, the surface with V_O, and the surface with two H atoms, respectively.

The initial geometry of the CeO_2 surface containing V_O was created by removing a single oxygen atom from the pristine CeO_2 and Fe/H_2SO_4-modified CeO_2 surfaces. The formation energy of V_O on the pristine CeO_2 was determined to be $\Delta E_{\mathrm{f}}^{\mathrm{O_2}}$ = 2.54 eV (Table 1), which agrees with a previously reported value of 2.61 eV.[46] In this case, $\Delta E_{\mathrm{f}}^{\mathrm{O_2}}$ was found to be similar to $\Delta E_{\mathrm{f}}^{\mathrm{H_2O}}$ (2.46 eV), as shown in Table 1. It was therefore considered that several V_O candidates exist on the Fe_CeO_2 surface, as presented in Figure S6. More specifically, V_O species are formed most easily around the doped Fe atoms; the most stable one is shown in Figure 4b, wherein the energies of formation were determined to be $\Delta E_{\mathrm{f}}^{\mathrm{O_2}}$ = 0.84 eV and $\Delta E_{\mathrm{f}}^{\mathrm{H_2O}}$ = 2.18 eV. The formation of V_O was also found to induce a large cavity close to Fe, which could act as a possible adsorption site for small reactants or K (Figure 4b). The effect of H_2SO_4 adsorption on V_O formation was also investigated (Figures 4c1 and 4d1), and it was found that in H_2SO_4-modified CeO_2 systems, V_O species are easily formed at the sites close to the oxygen atoms of Ce–O_{sul} moieties. After V_O formation, surface reorganization takes place around V_O and SO_4, and O_{sul} occupies the V_O site, as shown in Figures 4c2 and 4d2. The energy difference between isomers c1 and

c2 is 0.91 eV and that for isomers d1 and d2 is 0.63 eV; therefore, $\Delta E_{\mathrm{f}}^{\mathrm{H_2O}}$ was calculated based on the more stable structures shown in Figures 4c2 and 4d2. The energy of V_O formation associated with $SO_4/CeO_2_V_O$ indicated that V_O species are more easily formed at sites close to the O_{sul} atom, with formation energies of $\Delta E_{\mathrm{f}}^{\mathrm{O_2}}$ = 0.27 eV and $\Delta E_{\mathrm{f}}^{\mathrm{H_2O}}$ = 0.58 eV being determined; by contrast, there were no obvious changes in the V_O formation energies at sites far from the O_{sul} species. These results therefore indicate that the adsorption of H_2SO_4 promotes V_O formation close to the SO_4 species. However, the formation of V_O is quite complicated where modification with both Fe and H_2SO_4 is carried out. In such a situation, the V_O sites can be roughly grouped into three types, namely O_{lat} close to O_{sul}, O_{lat} close to Fe, and O_{lat} between Fe and O_{sul}. As indicated by the V_O formation energy determined for the Fe_CeO_2 surface, the O_{lat} atom at the site between Fe and O_{sul} is the easiest to remove, while the O_{lat} is protonated on the H_2SO_4/Fe_CeO_2 surface. Hence, a new structure was obtained in which H was moved from the desorbing O_{lat} onto the opposite O_{lat}, thereby allowing the pathway of O_2 formation resulting from the direct desorption of the O_{lat} to be investigated (Figure S2p). More specifically, the O_2 and H_2O desorption pathways were examined, as outlined in Figures S2p and S2o, respectively. It was found that Figs. S2p and S2o surfaces are comparatively stable in terms of their electronic energies. Thus, the V_O formation energy determined for the SO_4/Fe_CeO_2 surface led to the following results for the O_2 and H_2O desorption pathways, respectively: $\Delta E_{\mathrm{f}}^{\mathrm{O_2}}$ = −0.04 eV and $\Delta E_{\mathrm{f}}^{\mathrm{H_2O}}$ = 0.67 eV.

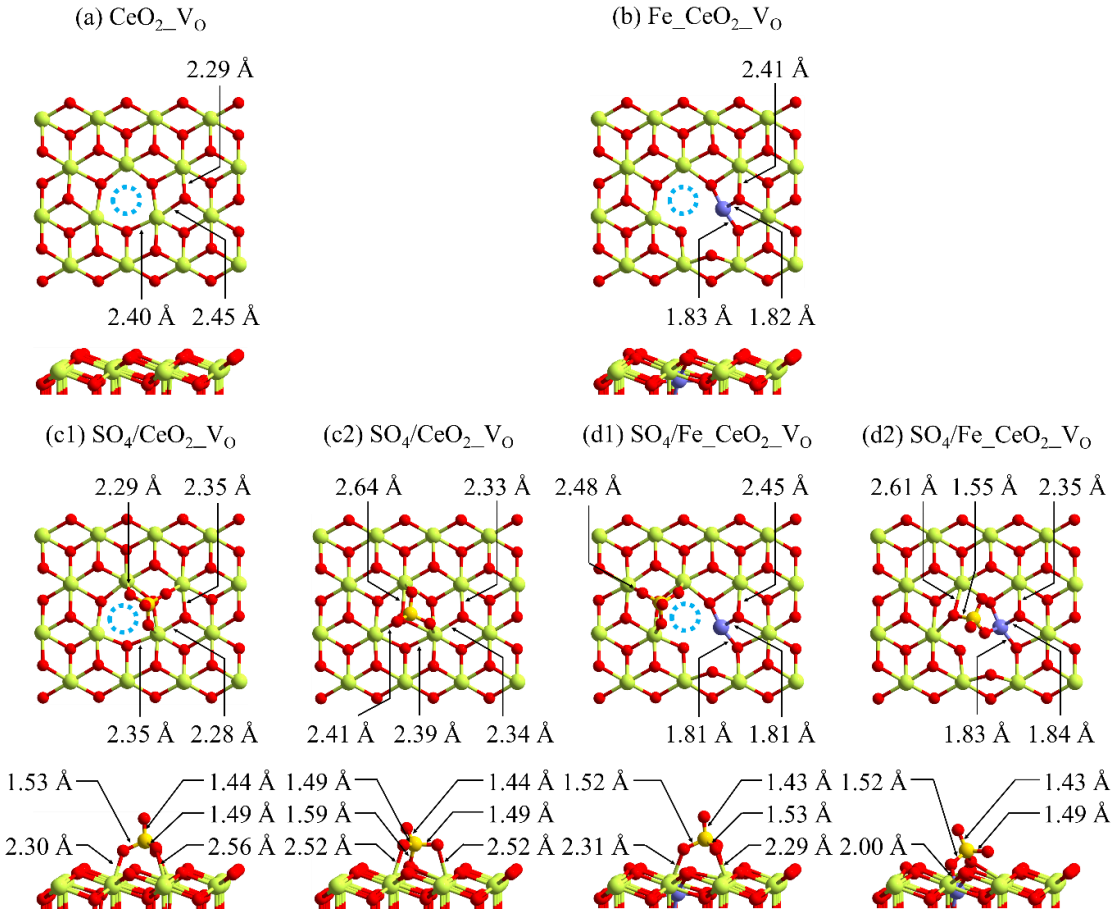


Figure 4. Top and right-side views of the surface models containing V_O. (a) CeO_2_ V_O, (b) Fe _CeO_2_V_O, (c1) SO_4/CeO_2_V_O, (c2) SO_4/CeO_2_V_O (SO_4 is bound to V_O), (d1) SO_4/Fe_CeO_2_V_O, and (d2) SO_4/Fe_CeO_2_V_O (SO_4 is bound to V_O). The dashed circles indicate the positions of V_O. The light green, red, dark blue, yellow colors indicated Ce, O, Fe, S atoms, respectively.

Table 1. Electronic (ΔE) and Gibbs energies (ΔG) for V_O formation in the various surface models. T^{cal} is the calcination temperature for catalyst preparation (800 K).

	CeO_2	Fe_CeO_2	H_2SO_4/CeO_2	H_2SO_4/Fe_CeO_2
$\Delta E_f^{O_2}$	2.54	0.84	0.27	−0.04
$\Delta E_f^{H_2O}$	2.46	2.18	0.58	0.67
$\Delta G(T^{cal}, P_{O_2})$	1.65	−0.05	−0.62	−0.93
$\Delta G(T^{cal}, P_{H_2O})$	0.72	0.44	−1.15	−1.06

Based on *ab initio* thermodynamics,[47] an approximated formula of the Gibbs energy for V_O formation is presented in the following equations:

$$\Delta G(T, P_{O_2}) \approx \Delta E_f^{O_2} + \Delta\mu_{O_2}(T, P_{O_2}^0) + RT \ln(P_{O_2}/P_{O_2}^0), \quad (6)$$

$$\Delta G(T, P_{H_2O}) \approx \Delta E_f^{H_2O} + \Delta\mu_{H_2O}(T, P_{H_2O}^0) + RT \ln(P_{H_2O}/P_{H_2O}^0). \quad (7)$$

The partial pressure of each molecule (P_X, $X = O_2, H_2O$) was determined from the following equation: $P_X/T = P_X^{atm}/T^{atm}$. Here, I used the partial pressure of oxygen in the atmosphere (2.10×10^{-2} MPa) for $P_{O_2}^{atm}$ and the saturated vapor pressure (0.32×10^{-2} Mpa, 298.15 K), which was obtained by Tetens equation[48] (S1) in the Supporting Information, for $P_{H_2O}^{atm}$. In addition, $\Delta\mu_{O_2}(T, P_{O_2}^0)$ and $\Delta\mu_{H_2O}(T, P_{H_2O}^0)$ are given by equations (S2) and (S3), respectively.

The temperature and pressure dependencies of μ were obtained from the NIST-JANAF thermodynamics tables.[49] Figure 5 shows the Gibbs energy changes associated with the V_O formation reactions, wherein the corresponding values were determined based on *ab initio* thermodynamics. The pathways of O_2 desorption and H_2O desorption were considered for the V_O formation reaction as shown in Figure 5. Figure 5a shows that

the formation of V_o becomes easier with increasing temperature, and it is an exothermic process at 800K, which is the calcination temperature for catalyst preparation. Both Fe and H_2SO_4 can promote V_O formation under the conditions evaluated herein, which is consistent with the PDOS results and the experimental observations.[15,50,51] In particular, H_2SO_4 modification significantly reduced the V_O formation energy on the CeO_2 surface. Additionally, V_O formation with the release of H_2O was found to be an exothermic process on the H_2SO_4-modified surface. Furthermore, the formation of V_O species by H_2O desorption is more favored on the H_2SO_4/CeO_2, and H_2SO_4/Fe_CeO_2 surfaces than the formation of V_O species via O_2 desorption at calcination temperature (800 K). By contrast, the desorption energy of H_2O on the Fe_CeO_2 surfaces is large because protonated O_{lat} species around the Fe sites are considerably stable.

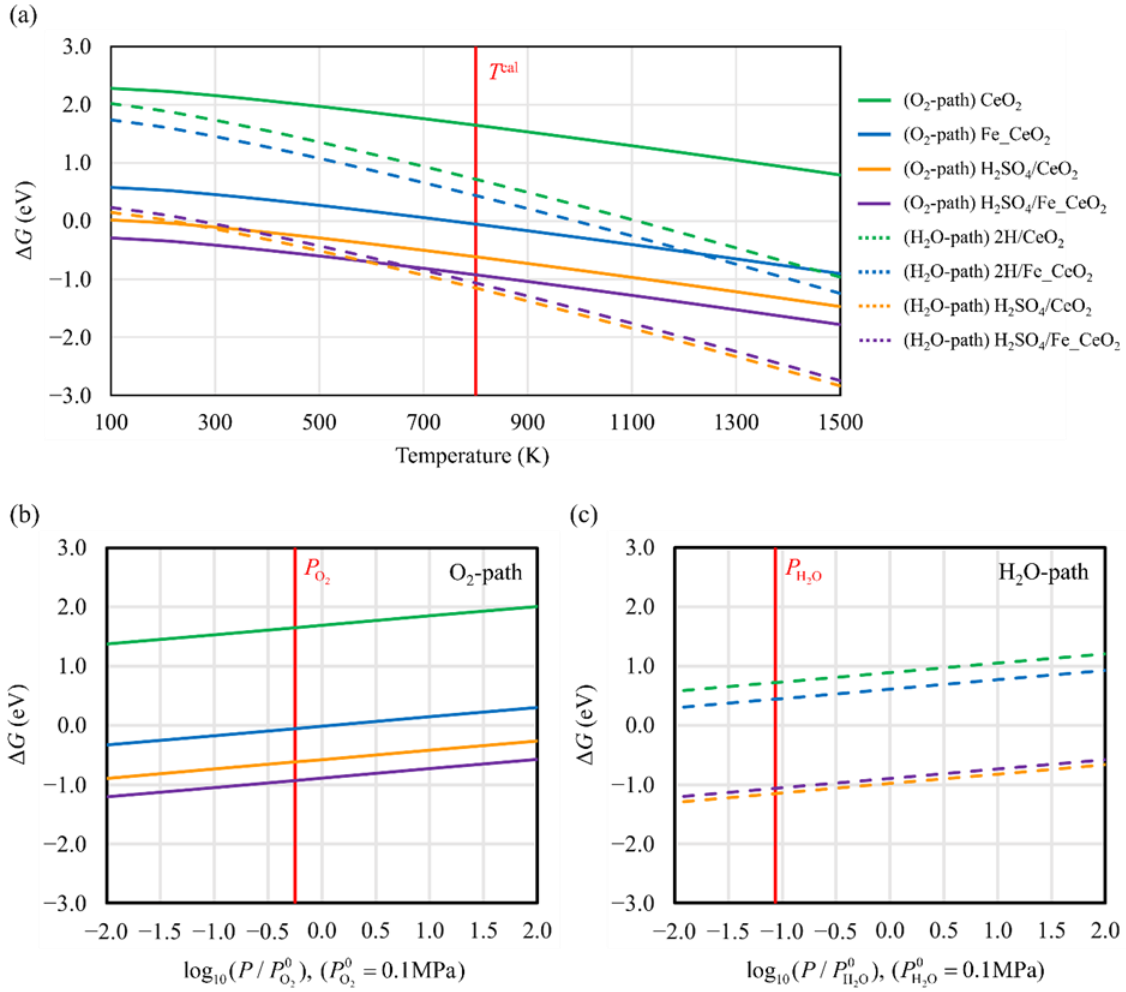


Figure 5. (a) Temperature dependence on Gibbs energy change of oxygen vacancy (V_O) formation attributed to O_2 desorption (solid lines) and H_2O desorption (dashed lines). V_O formation on the CeO_2 surface (green), Fe_CeO_2 surface (blue), H_2SO_4/CeO_2 surface (orange), and H_2SO_4/Fe_CeO_2 surface (purple). T^{cal} is calcination temperature. (b) Pressure dependence on Gibbs energy change of V_O by O_2 desorption path at T^{cal}. P_{O_2} is partial pressure of O_2 at 800 K (c) Pressure dependence on Gibbs energy change of V_O formation by H_2O path at T^{cal}. P_{H_2O} is partial pressure of H_2O at 800 K.

2.3.4. Alkali Metal Poisoning

KNO_3 was used as precursor to prepare K_2O in the experimental investigations.[17] The adsorption of the single K atom and that of K_2O with the counter anion on CeO_2 surfaces were compared (Figure S8). It was shown that the trend of K and K_2O adsorption was consistent with Fe_CeO_2 > H_2SO_4/CeO_2 > CeO_2. The charge of K in K@CeO_2 and K_2O@CeO_2 is almost the same, +0.87 |e| and +0.86 |e|, respectively. Both K and K_2O are slightly reducing the surface in the same way. The charge transfers from adsorbed K atom and K_2O molecule to CeO_2 surface are –0.87 |e| and –0.53 |e|, respectively. Thus, I used K as a model to investigate the detailed poisoning mechanism.

Initially, the stabilities of the K and H atoms on the CeO_2 surface were compared to investigate the effect of K on the BA sites. The relative stabilities of the protonated and K-adsorbed surfaces were evaluated using the K–H exchange reaction (8), which is associated with the exchange energy, E_{ex}, given in equation (9).

$$\mathrm{H@Surface} + \frac{1}{2}\mathrm{K_2O(g)} \rightarrow \mathrm{K@Surface} + \frac{1}{2}\mathrm{H_2O(g)}, \quad (8)$$

$$E_{ex} = E_{\mathrm{K@Surface}} + \frac{1}{2}E_{\mathrm{H_2O(g)}} - E_{\mathrm{H@Surface}} - \frac{1}{2}E_{\mathrm{K_2O(g)}}, \quad (9)$$

where $E_{\mathrm{H_2O(g)}}$ and $E_{\mathrm{K_2O(g)}}$ are the total energies of the H_2O and K_2O molecules in a vacuum, respectively. In addition, H@Surface and K@Surface represent the protonated and K-adsorbed surfaces, respectively, while $E_{\mathrm{H@Surface}}$ and $E_{\mathrm{K@Surface}}$ are the total energies of H@Surface and K@Surface, respectively. Figure 6 shows the most stable adsorption site for H on each surface with E_{ex}, and the adsorption structure of K after the K–H exchange reaction is shown in Figure S10. The obtained E_{ex} values demonstrate that

K is more stably adsorbed than H on all surfaces, which indicates that K species inhibit the formation of BA sites by occupying O_{lat} (Figure 6). Therefore, alkali metal poisoning could cause a decrease in the number of available BA sites in CeO_2-based catalysts. This result is consistent with the decrease in NH_3 adsorption observed on the K-poisoned catalyst.[17]

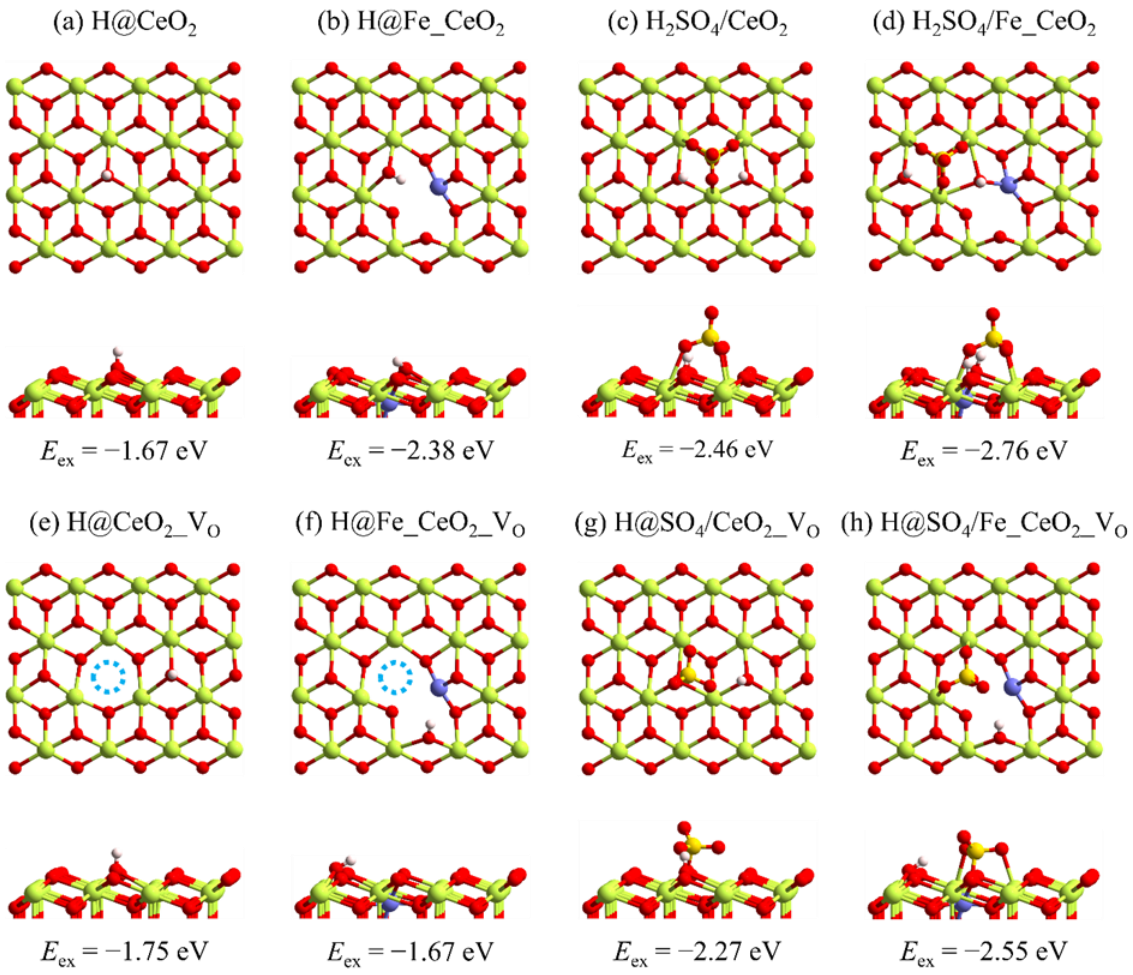


Figure 6. Top and right-side views of the protonated surfaces: (a) $H@CeO_2$ surface, (b) $H@Fe_CeO_2$ surface, (c) H_2SO_4/CeO_2 surface, (d) H_2SO_4/Fe_CeO_2 surface, € $H@CeO_2_V_O$ surface, (f) $H@Fe_CeO_2_V_O$ surface, (g) $H@SO_4/CeO_2_V_O$ surface, and (h) $H_2SO_4/Fe_CeO_2_V_O$ surface. E_{ex} is the energy of the K–H exchange reaction. The

dashed circles indicate the positions of V_O. The light green, red, dark blue, yellow and white colors indicated Ce, O, Fe, S, H atoms, respectively.

2.3.5. Alkali Metal Adsorption

In this section, the interaction between K and the CeO_2 surfaces both with and without V_O is discussed. The adsorption sites for the K atoms were investigated using the K adsorption reaction (10), which is associated with the adsorption energy, E_{ads}, given in equation (11).

$$\mathrm{Surface} + \frac{1}{2}\mathrm{K_2O(g)} \rightarrow \mathrm{K@Surface} + \frac{1}{4}\mathrm{O_2(g)} \tag{10}$$

$$E_{\mathrm{ads}} = E_{\mathrm{K@Surface}} + \frac{1}{4}E_{\mathrm{O_2(g)}} - E_{\mathrm{Surface}} - \frac{1}{2}E_{\mathrm{K_2O(g)}} \tag{11}$$

As shown in Figure 7a, the K atom is adsorbed at the O_{lat} species in the hollow site on the pristine CeO_2 surface. By contrast, on the Fe-doped CeO_2 surface, the adsorption site for the K atom changes to the V_O-like site close to the Fe site (Figures 7b and 7d). In addition, as shown in Figure 7c, the introduction of H_2SO_4 enhances adsorption of the K atom by interacting with both the O_{lat} and O_{sul} atoms. The resulting V_O-like site provides a cavity for K adsorption on the Fe site with large adsorption energies of −3.27 and −2.72 eV on Fe_CeO_2 and H_2SO_4/Fe_CeO_2, respectively (Figures 7b and 7d). Furthermore, it was determined that the stability of K on CeO_2 surface in the absence of V_O decreased in the order of: Fe_CeO_2 (−3.27 eV) > H_2SO_4/Fe_CeO_2 (−2.72 eV) > H_2SO_4/CeO_2 (−2.62 eV) > pristine CeO_2 (−1.60 eV). Overall, these results indicate that both H_2SO_4 and Fe enhance K adsorption, thereby causing K atoms to accumulate close to the additives.

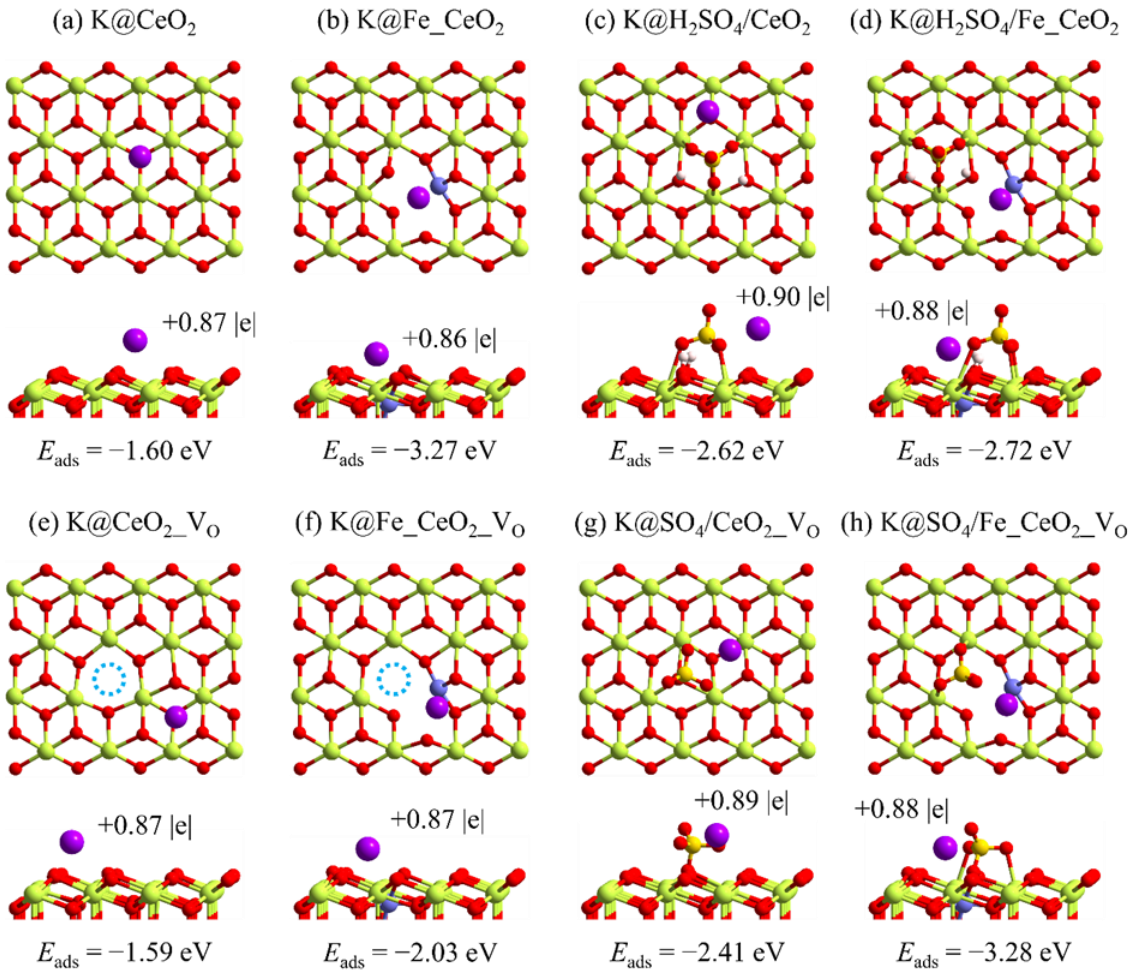


Figure 7. Top and right-side views of K adsorption on the (a) CeO_2 surface, (b) Fe_CeO_2 surface, (c) H_2SO_4/CeO_2 surface, (d) H_2SO_4/Fe_CeO_2 surface, (e) CeO_2_V_O surface, (f) Fe_CeO_2_V_O surface, (g) H_2SO_4/CeO_2_V_O surface, and (h) H_2SO_4/Fe_CeO_2_V_O surface. The dashed circles indicate the positions of V_O. The Bader atomic charges for the adsorbed K species are also given. The light green, red, dark blue, yellow, white and purple colors indicated Ce, O, Fe, S, H and K atoms, respectively.

The effects of V_O were also considered in the context of K poisoning. As shown in Figures 7a and 7e, only minor changes were observed in the K adsorption energy in the

presence and absence of V_O, and no preferential K adsorption was observed on the surface containing V_O. This was attributed to the positively charged Ce atoms exposed on the outermost surface of the V_O site, which repel the positively charged K ions. In addition, V_O formation did not affect neighboring K adsorption on the O_{lat} of the pristine CeO_2 surface, wherein the K atoms interacted with O_{lat} rather than with the V_O site (Figures 7e and 7f). Moreover, K adsorption was weakened on Fe_CeO_2_V_O as the V_O was formed close to the Fe site (Figure 7f). In the case of the modified H_2SO_4, the V_O sites can be easily re-oxidized by the adjacent O_{sul} atom (Figure 7g), thereby leading to no obvious changes in K adsorption. However, it was found that the formation of V_O on the H_2SO_4/Fe_CeO_2 surface highly enhanced the adsorption of K, with an adsorption energy of −3.28 eV being determined, which is twice as large as that in the case of a pristine CeO_2 surface (Figure 7h). The stability of K on the CeO_2 surfaces containing V_O was therefore determined to decrease in the order of: SO_4/Fe_CeO_2_V_O (−3.28 eV) > SO_4/CeO_2_V_O (−2.41 eV) > Fe_CeO_2_V_O (−2.03 eV) > CeO_2_V_O (−1.59 eV) ≈ pristine CeO_2 (−1.60 eV), thereby confirming that the presence of H_2SO_4 and Fe additives enhanced K adsorption on the surfaces containing V_O. From these results, the enhanced adsorption energy of K observed in Figures 7b and 7h can be attributed to the structural rearrangement of O_{sul} and O_{lat} surrounding the K. In addition, H_2SO_4 should be adsorbed around the Fe site, as the molar ratio of Fe to H_2SO_4 in the experimental study was determined to be 0.2:1.[17] Therefore, the favorable K adsorption taking place on the SO_4/Fe_CeO_2_V_O sites protects the other BA sites from alkali metal poisoning, ultimately contributing to the maintenance of a high NO_X conversion over time. This factor could therefore be the origin of the synergistic effect between Fe and H_2SO_4 in terms of improving the alkali tolerance of the catalyst surface.

Subsequently, the Bader charge and electron density differences were analyzed to clarify the interactions between the K atoms and the surfaces. As presented in Figure 7a, the adsorbed K possesses a positive charge on the pristine CeO_2 surface, indicating that K is in the cationic state. The charges of the K atoms on Fe_CeO_2 (Figure 7b) and Fe_CeO_2_V_O (Figure 7f) were determined to be similar to those on pristine CeO_2, while the K atoms around the sulfate groups were found to possess slightly larger positive charges on the H_2SO_4/CeO_2 (Figure 7c) and SO_4/CeO_2_V_O (Figure 7g) surfaces. In addition, the K atoms exhibited similar trends around the SO_4/Fe sites on H_2SO_4/Fe_CeO_2 (Figure 7d) and SO_4/Fe_CeO_2_V_O (Figure 7h). Although these results indicate that all K species were in the cationic state, no clear correlation was found between the degree of charge and the adsorption energy of the K atoms.

The effect of K on the NH_3 molecule adsorption on pristine CeO_2 surface was investigated by comparing NH_3 adsorption on Brønsted acid (BA) sites, Lewis acid (LA), with and without K. The results were summarized in Figure S17. It was shown that NH_3 molecules can be adsorbed on Brønsted acid sites, Lewis acid (LA) with adsorption energy −0.61 eV and −0.77 eV, respectively. NH_3 interacts with the BA site through hydrogen bonds but forms a covalent bond with the Ce atom of the CeO_2 surface. The existence of K species at the LA site does not affect NH_3 adsorption energy strongly, which are similar to the previous report.[12] While K species preferentially occupy the LA site as it binds to the LA site much stronger (−1.60 eV). When K replaces the proton at BA sites, the adsorbed NH_3 is stabilized at the top site of K species which is far from the CeO_2 catalyst with an adsorption energy of −0.52 eV. Therefore, K at Brønsted acid site inhibits the NH_4^+ formation, also the interaction between the CeO_2 catalyst and NH_3 molecule to generate NH_2 species.

2.3.6. Charge Density Differences

Figure 8 shows the difference in electron density induced on the surfaces upon K adsorption. The electron density difference ($\Delta\rho$) was calculated as $\Delta\rho = \rho_{K@Surface} - \rho_{Surface} - \rho_{K(g)}$, where $\rho_{K@Surface}$, $\rho_{Surface}$, and $\rho_{K(g)}$ are the electron density distributions of the K-adsorbed surface, the surface alone, and K atoms in the vacuum layer, respectively. The decrease in the electron density (blue isosurface) around the adsorbed K corresponds to the transfer of valence electrons from the K 4*s* orbitals to the CeO_2 surface (Figure 8a). The orange isosurface indicates that the electron density increased in the 2*p* orbital of O_{lat}, indicating the role of the acceptor orbitals in the electron transfer process associated with K adsorption. The changes in the charge densities of the Ce and Fe atoms upon K adsorption are also shown in Figure 8, wherein it can be seen that the changes in the electron density that took place upon K adsorption also affected the adjacent Ce atoms through the O_{lat} atoms. Similar charge transfer from the K atom to the O_{lat} species was also observed on the Fe_CeO_2 surface (Figure 8b). In addition, an increase in the electron density was observed between K and Fe, suggesting that interactions with both Fe and O_{lat} could account for the strong adsorption of K at the Fe sites. It was deduced that charge transfer between K and the surface occurred through three O_{lat} atoms on the Fe_CeO_2 surface, while only two O_{lat} atoms were involved in the case of the Fe_CeO_2_V_O surface (Figures 8b and 8f). This indicates that the decrease in the K adsorption energy on the Fe_CeO_2_V_O surface is attributed to the absence of one characteristic O_{lat} by V_O formation. Interactions were also observed between the K atom and the three O_{sul} atoms in the H_2SO_4/CeO_2 system (Figure 8c), thereby accounting for the relatively strong adsorption of K on H_2SO_4/CeO_2. Furthermore, for the H_2SO_4/CeO_2_V_O system, only two

O_{sul} atoms interacted with the K atom, and the K adsorption energy was smaller than that on H_2SO_4/CeO_2 (Figure 8g). The charge transfer occurred among the K atoms, three O_{lat} atoms, and Fe atoms (Figure 8d). Nevertheless, the small adsorption energy associated with the K atom can be attributed to repulsion between the positive charges of the H and K atoms. The highest K adsorption energies are −3.27 eV for Fe_CeO_2 and −3.28 eV for $H_2SO_4/Fe_CeO_2_V_O$. The O_{lat} site at Fe_CeO_2 and the O_{lat} and O_{sul} sites at H_2SO_4/Fe_CeO_2_Vo are responsible for the strong adsorption of K, respectively. These results were mainly attributed to the interactions between the O_{lat} and O_{sul} atoms surrounding the K atom (Figures 8b and 8h).

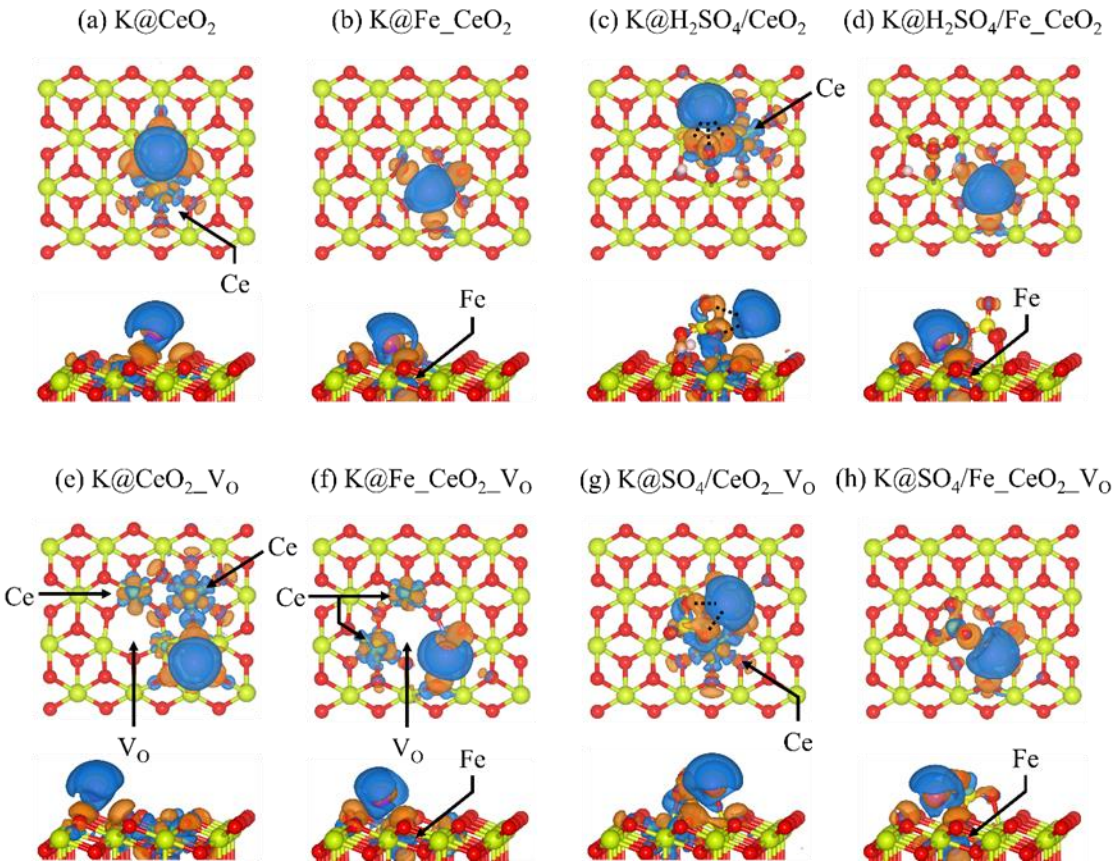


Figure 8. Top view and right-hand view of the electron density differences upon K adsorption on the (a) CeO_2 surface, (b) Fe_CeO_2 surface, (c) H_2SO_4/CeO_2 surface, (d)

H_2SO_4/Fe_CeO_2 surface, (e) CeO_2_V_O surface, (f) Fe_CeO_2_V_O surface, (g) H_2SO_4/CeO_2_Vo surface, and (h) H_2SO_4/Fe_CeO_2_V_O surface. The blue and orange isosurfaces indicate a decrease and increase in the charge density, respectively.

2.3.7. Adsorption of Multiple Potassium Atoms

According to the previously reported experimental details, the Fe:K ratio is equal to 1:5.7,[17] and so multiple K adsorption were considered. The adsorption sites for the K atoms were investigated considering multiple K adsorption steps (12), which are associated with the relative energies, $E_{\mathrm{ads}}(n)$, given in equation (13):

$$\mathrm{Surface} + \frac{n}{2}\mathrm{K_2O(g)} \rightarrow n\mathrm{K@Surface} + \frac{n}{4}\mathrm{O_2(g)}, \tag{12}$$

$$E_{\mathrm{ads}}(n) = E_{n\mathrm{K@Surface}} + \frac{n}{4}E_{\mathrm{O_2(g)}} - E_{\mathrm{Surface}} - \frac{n}{2}E_{\mathrm{K_2O(g)}}, \tag{13}$$

where n (= 1–4) is the number of K atoms, $E_{n\mathrm{K@Surface}}$, E_{Surface}, and $E_{\mathrm{K_2O(g)}}$ are the total energies of nK atoms adsorbed on the surface, the surface alone, and the K_2O molecules in a vacuum, respectively.

The adsorption of K on the considered four surfaces (CeO_2, Fe_CeO_2, SO_4/CeO_2_V_O, SO_4/Fe_CeO_2_V_O) were compared. It was shown that K adsorption becomes weaker with the increased number of adsorbed K atoms. The detailed adsorption energy of K atoms on CeO_2, Fe_CeO_2, SO_4/CeO_2_Vo, SO_4/Fe_CeO_2_Vo were summarized in Figure S18, and their structures were shown in Figure S19. To make clear the difference between the case of additives Fe and H_2SO_4, I focus on the comparison of adsorption energies of the

K atoms on the $SO_4/CeO_2_V_O$ surface and the $SO_4/Fe_CeO_2_Vo$ surface in Figure 9.

Figure 9a indicates that both the $SO_4/CeO_2_V_O$ and $SO_4/Fe_CeO_2_V_O$ surfaces can adsorb multiple K atoms. The energy change between each step presented in Figure 9a is shown in Figure 9b, wherein it can be seen that the adsorption energy of the K atoms decreased as the extent of K adsorption increased on the $SO_4/CeO_2_V_O$ surface. Considering the case of up to three K atoms on the $SO_4/CeO_2_V_O$ surface, the calculated adsorption energy per K atom was greater than the adsorption energy for a single K atom on the pristine CeO_2 surface. However, the binding energies of the third and fourth K atoms on the $SO_4/Fe_CeO_2_V_O$ surface were still higher than those of the single K atom on the pristine CeO_2 surface. Except for the site nearby SO_4 species, normal CeO_2 sites nonadjacent to SO_4 can also trap K species. It was found that the K adsorptions up to 7 K atoms are exothermic on $SO_4/CeO_2_V_O$ and $SO_4/Fe_CeO_2_V_O$. When the number of K is larger than 4, the adsorption energy of K becomes smaller than the one on the pristine CeO_2 surface. Detailed information about multiple K adsorption can be found in Figure S20. Additionally, their structures were summarized in Figure S21.

In addition, the geometry of the charge state of the 4K@surface was analyzed (see Table 2), and it was found that the Bader charges of the adsorbed K and O atoms did not change significantly between the $SO_4/CeO_2_V_O$ and $SO_4/Fe_CeO_2_V_O$ surfaces. However, it was deduced that the distances between the adsorbed K atoms on the $SO_4/Fe_CeO_2_V_O$ surface are shorter than those on the $SO_4/CeO_2_V_O$ surface, which indicates that the additional Fe content causes the K atoms to gather together. In other words, the unique surface structure of $SO_4/Fe_CeO_2_V_O$ played an important role in protecting the NH_3 adsorption sites from alkali metal poisoning.

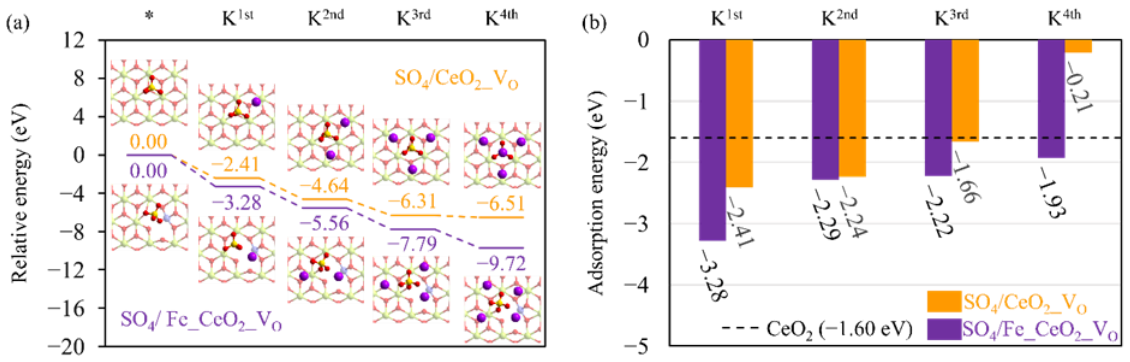


Figure 9. (a) Adsorption energies of the K atoms on the $SO_4/CeO_2_V_O$ surface (orange line) and the $SO_4/Fe_CeO_2_V_O$ surface (purple line) relative to the isolated surface and the K atoms. (b) Adsorption energies of the n^{th} K atoms relative to the $(n-1)^{th}$@surface. * represents the surface without adsorbate.

Table 2. Distance (Å) between the K atom and the closest O atom, along with their Bader charges (|e|) for the geometry of the 4K@surface. The references for Bader change are set to the total number of electrons associated with isolated K and O atoms

$4K@SO_4/CeO_2_V_O$	Distance	Charge (K)	Charge (O)
K^{1st}	2.76	0.87	−1.31
K^{2nd}	2.76	0.86	−1.29
K^{3rd}	2.75	0.87	−1.29
K^{4th}	2.79	0.92	−1.35

4K@SO_4/Fe_CeO_2_V_O	Distance	Charge (K)	Charge (O)
K^{1st}	2.49	0.85	−1.19
K^{2nd}	2.70	0.88	−1.27
K^{3rd}	2.61	0.88	−1.29
K^{4th}	2.53	0.88	−1.27

2.4. Conclusion

In this study, density functional theory (DFT) calculations were used to clarify how alkali metal poisoning is prevented in the CeZr oxide catalyst in the presence of Fe and H_2SO_4 additives. Based on previously reported experimental observations, CeO_2 was adopted as the surface model for the CeZr catalyst. Initially, the complex surface structure of the catalysts was investigated, and it was found that H_2SO_4 addition considerably promoted the formation of oxygen vacancies (V_O) on the CeO_2 surface under calcination conditions. In addition, these V_O easily combined with the oxygen atoms of a neighboring sulfate (SO_4) group to form unique SO_4/CeO_2_V_O and SO_4/Fe_CeO_2_V_O surfaces. The thermodynamic stabilities of the various states were also evaluated using *ab initio* thermodynamic calculations. As a result, it was deduced that V_O formation was promoted by the presence of H_2SO_4, and the V_O sites were thermodynamically stable under the experimental operating conditions. Subsequently, the effect of K poisoning on the CeO_2 surfaces was investigated, wherein K occupies the lattice oxygen sites and inhibits the formation of Brønsted acid sites, which are closely related to the activity of the selective catalytic reduction of ammonia. This result was associated with a reduced degree of NH_3 adsorption on the catalytic surface and the consequent decrease in NO_X conversion.

Investigation of the K adsorption energy showed that K adsorption at the SO_4/Fe_CeO_2_V_O site is preferable to that observed on a normal CeO_2 surface, with up to four K atoms being adsorbed on the former. Hence, the synergistic effect of Fe and H_2SO_4 provides multiple K adsorption sites on the catalyst surface, which ultimately protects the NH_3 adsorption sites from K poisoning and contributes to the maintenance of a high NO_X conversion. These findings can also provide insights into understanding the ability of metal oxide-based catalysts with sulfate ions against alkali-poisoning. Furthermore, they open new avenues for facilitating the tailored design of alkali-tolerant catalysts for NH_3-SCR. I believe that atomic-level insight into the mechanisms of alkali metal poisoning and tolerance of SCR catalysts contributes to the design of catalysts applicable to biomass fuels that contain high amounts of alkali metal. One potential avenue for future research is to understand the effect of the K on the catalytic activity of metal oxide surface for SCR reactions.

2.5. Supporting Information

S1. Various Adsorption Structures of H_2SO_4 on Catalytic Surface.

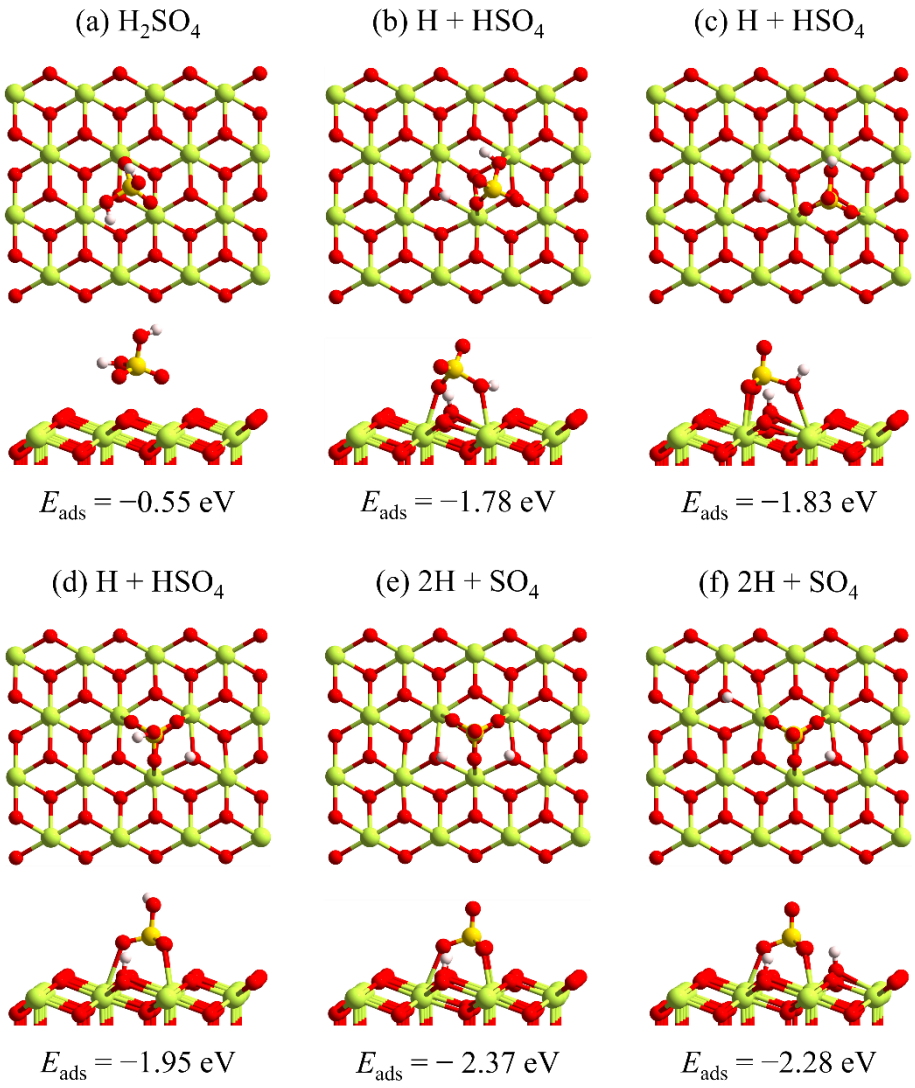


Figure S1. Various adsorption structures of H_2SO_4 on CeO_2 surface. E_{ads} is adsorption energy: $E_{ads} = E_{H_2SO_4@Surface} - E_{H_2SO_4(g)} - E_{Surface}$.

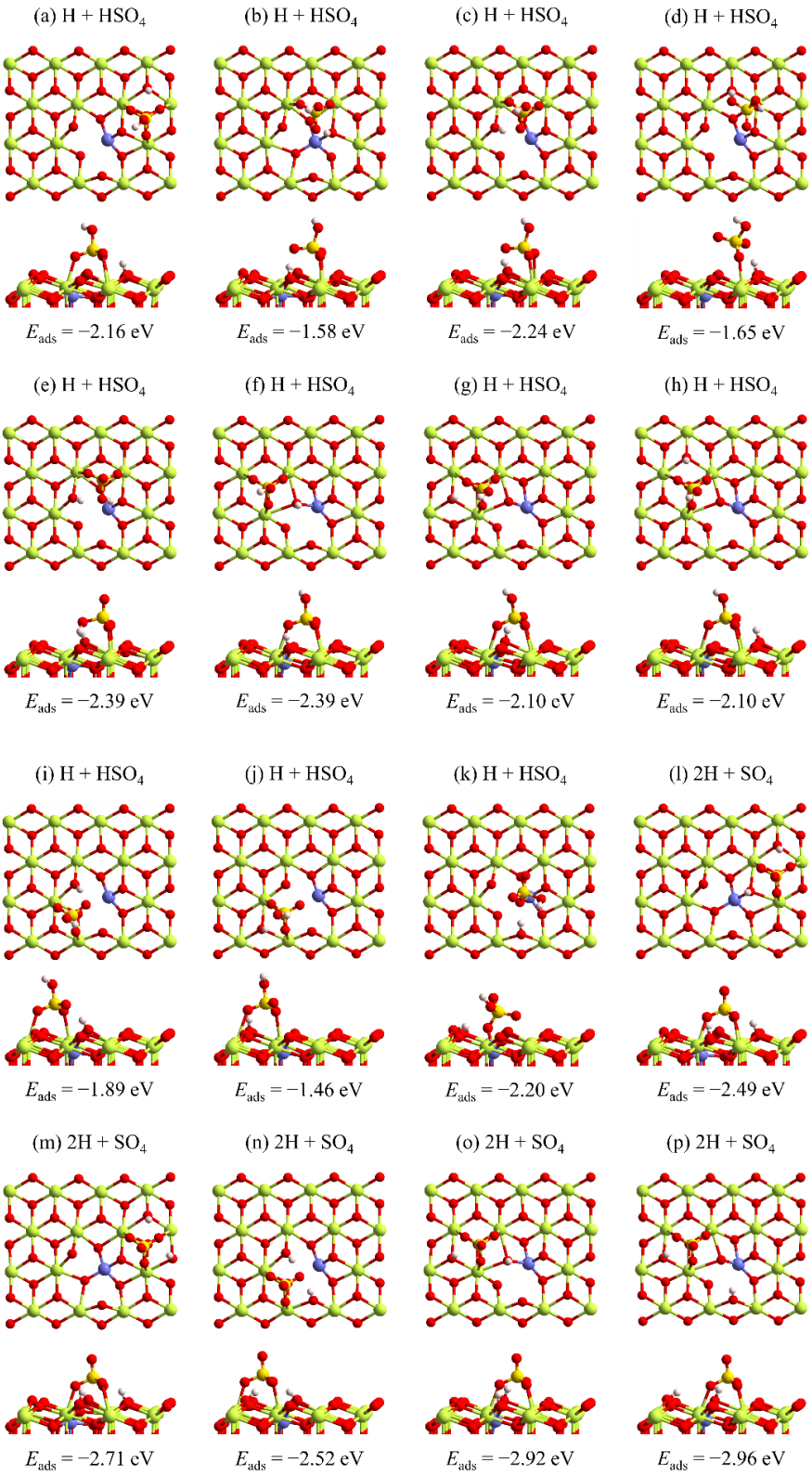


Figure S2. Various adsorption structures of H_2SO_4 on Fe_CeO_2 surface.

S2. Projected Density of States.

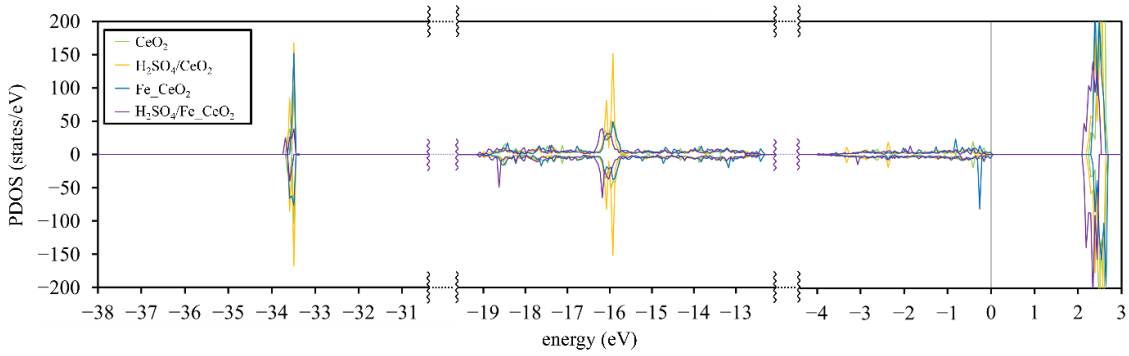
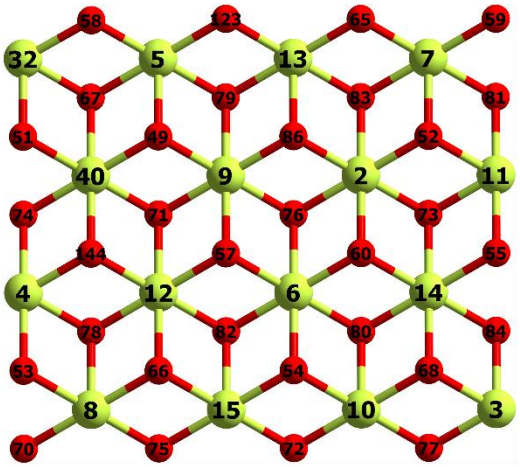


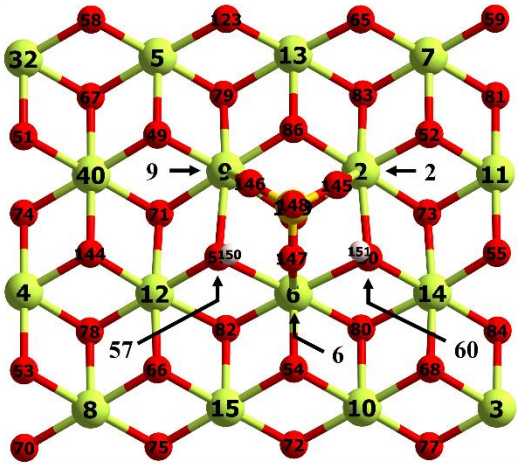
Figure S3. PDOS of 16 metals in the top Ce 1 layer. The PDOS energy of Fe_CeO_2, H_2SO_4/CeO_2, and H_2SO_4/Fe_CeO_2 were shifted to match the largest peak in inner shell states (approximately −33.5 eV) of CeO_2.

(a) CeO_2



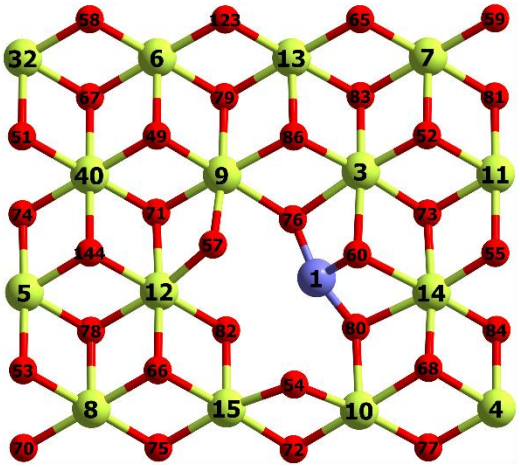
PDOS of Ce; 2, 6 and 9
PDOS of O_{lat}; 57, 60 and 86

(b) H_2SO_4/CeO_2



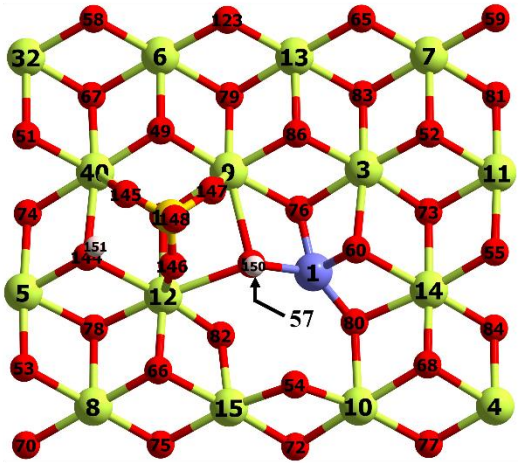
PDOS of Ce; 2, 6 and 9
PDOS of O_{lat_near}; 57, 60 and 86
PDOS of O_{lat_far}; 145, 146 and 147

(c) Fe/CeO_2



PDOS of Fe; 1
PDOS of Ce; 3, 9 and 14
PDOS of O_{lat_near}; 54, 57 and 60
PDOS of O_{lat_far}; 49, 51 and 58

(d) H_2SO_4/Fe_CeO_2



PDOS of Fe; 1
PDOS of Ce-S; 9, 12 and 40
PDOS of Ce-S; 3, 10 and 14
PDOS of O_{lat_near}; 54, 57 and 60
PDOS of O_{lat_far}; 53, 55 and 68

Figure S4. List of atoms selected to plot PDOS.

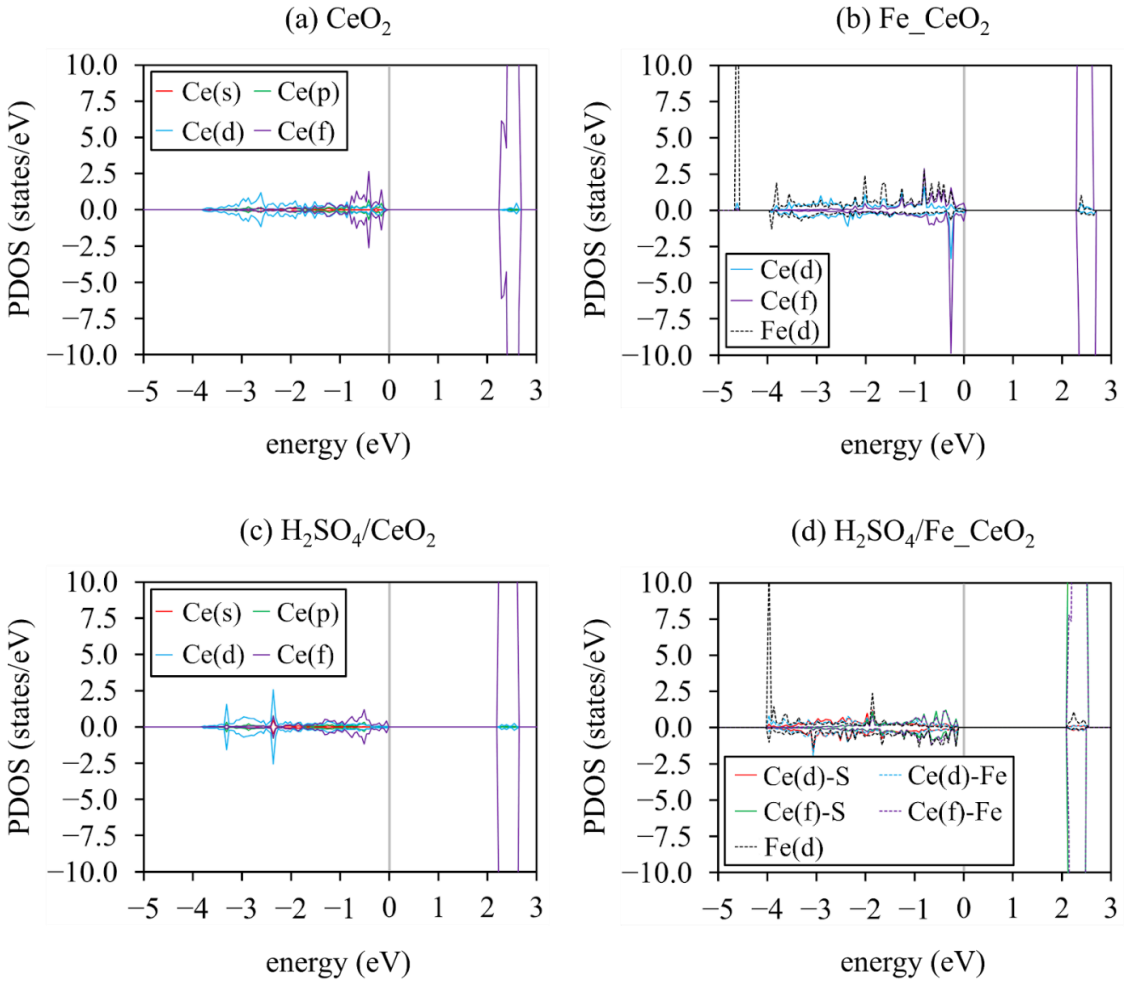


Figure S5. The PDOS for s, p, d, and f states of Ce atoms for the geometries in Figure 2c. Ce(d,f)-S and Ce(d,f)-Fe indicate PDOS of Ce atoms around H_2SO_4 and Fe, respectively. The positions of the selected Ce and O atoms used for the PDOS are shown in Figure S4.

S3. Comparison of V_O Position.

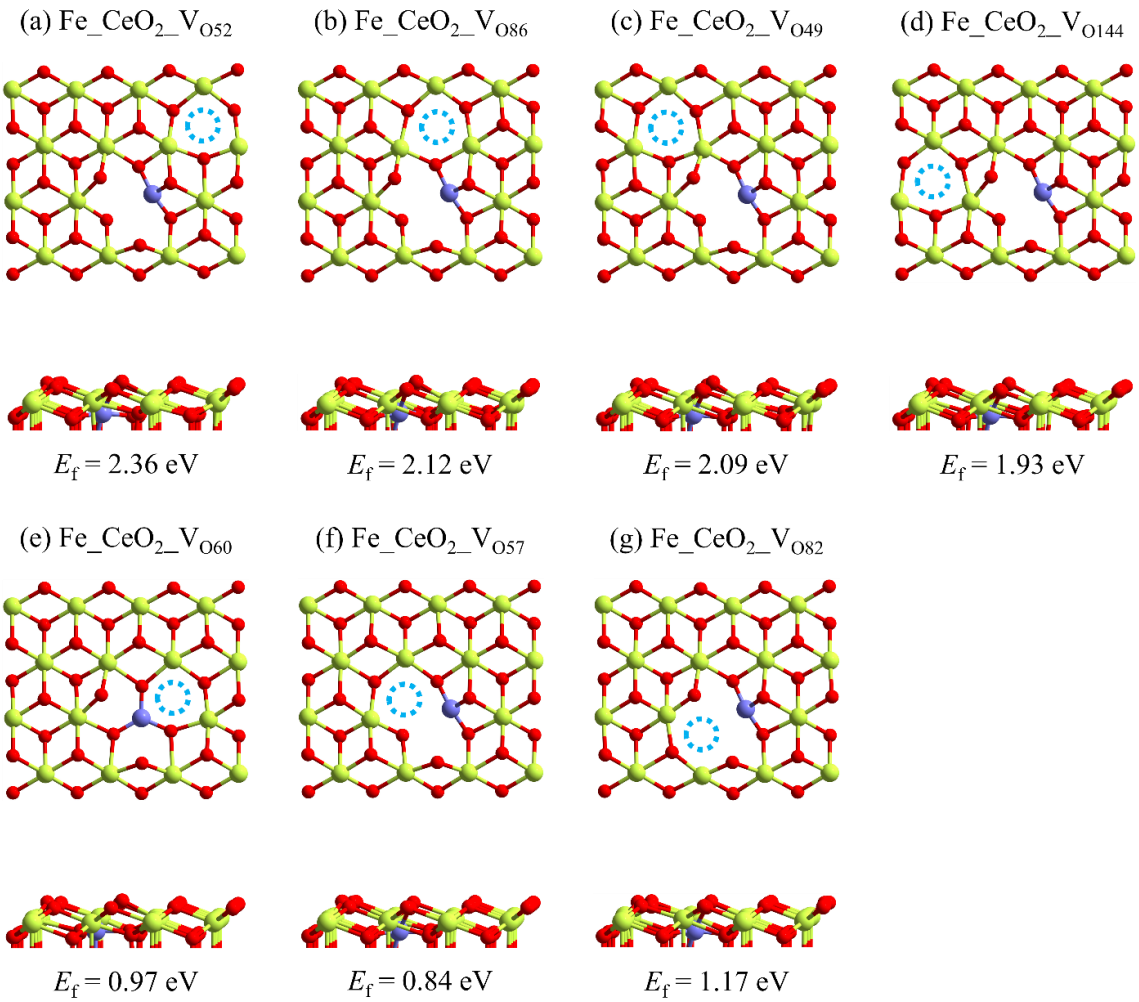


Figure S6. Stability of V_O on Fe_CeO_2 surface. The dashed circle indicates the position of V_O. E_f is formation energy: $E_f = E_{Fe_CeO_2_V_O} + 1/2E_{O_2(g)} - E_{Fe_CeO_2}$.

S4. Equation for Saturated Vapor Pressure and Chemical Potential.

Saturated vapor pressure (e_s) was calculated by Tetens equation

$$e_s = 6.11 \times 10^{\left(\frac{7.5\times T}{237.3+T}\right)}, \quad \text{(S1)}$$

where T is air temperature (°C).

$\mathbf{\Delta}\mu_{O_2}(T, P^0_{O_2})$ and $\mathbf{\Delta}\mu_{H_2O}(T, P^0_{H_2O})$ are given by

$$\mathbf{\Delta}\mu_{O_2}(T, P^0_{O_2}) = \mu_{O_2}(T, P^0_{O_2}) - \mu_{O_2}(T^0, P^0_{O_2})$$

$$= [H(T, P^0_{O_2}) - T \cdot S(T, P^0_{O_2})] - [H(T^0, P^0_{O_2}) - T^0 \cdot S(T^0, P^0_{O_2})], \quad \text{(S2)}$$

$$\mathbf{\Delta}\mu_{H_2O}(T, P^0_{H_2O}) = \mu_{H_2O}(T, P^0_{H_2O}) - \mu_{H_2O}(T^0, P^0_{H_2O})$$

$$= [H(T, P^0_{H_2O}) - T \cdot S(T, P^0_{H_2O})] - [H(T^0, P^0_{H_2O}) - T^0 \cdot S(T^0, P^0_{H_2O})], \quad \text{(S3)}$$

where T^0, $P^0_{O_2}$ and $P^0_{H_2O}$ are 0 K, 0.1 MPa and 0.1 MPa, respectively.

S5. Comparison of K and K_2O Adsorption.

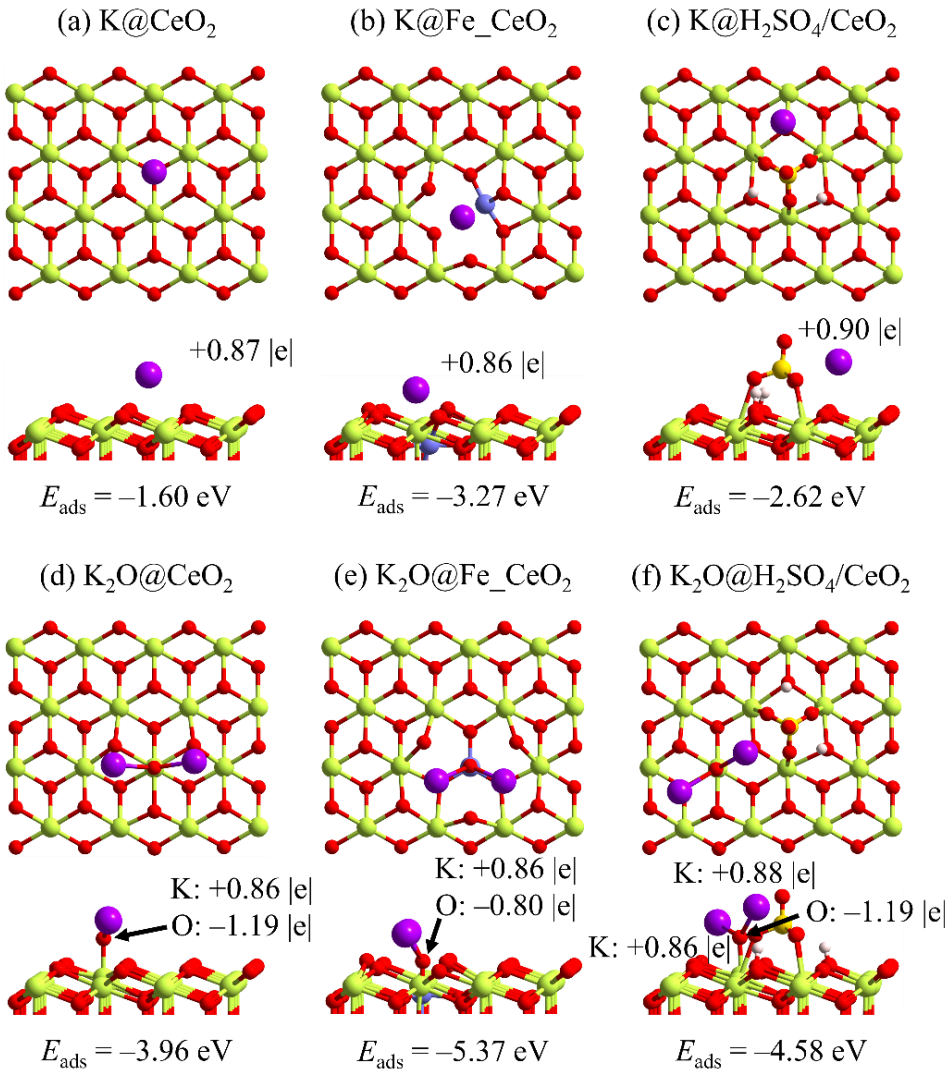


Figure S8. (a-c) K adsorption on the CeO_2 surface with/without additives. The adsorption energies were calculated by: $E_{ads} = E_{K@surface} + 1/4\,E_{O_2(g)} - E_{surface} - 1/2\,E_{K_2O(g)}$. (d-f) K_2O adsorption on the CeO_2 surface with/without additives. The adsorption energies were calculated by: $E_{ads} = E_{K_2O@surface} - E_{surface} - E_{K_2O(g)}$. The charge of the K atom and the O atom in the K_2O molecule are shown in each figure.

S7. Adsorption Structure of K on Each Surface.

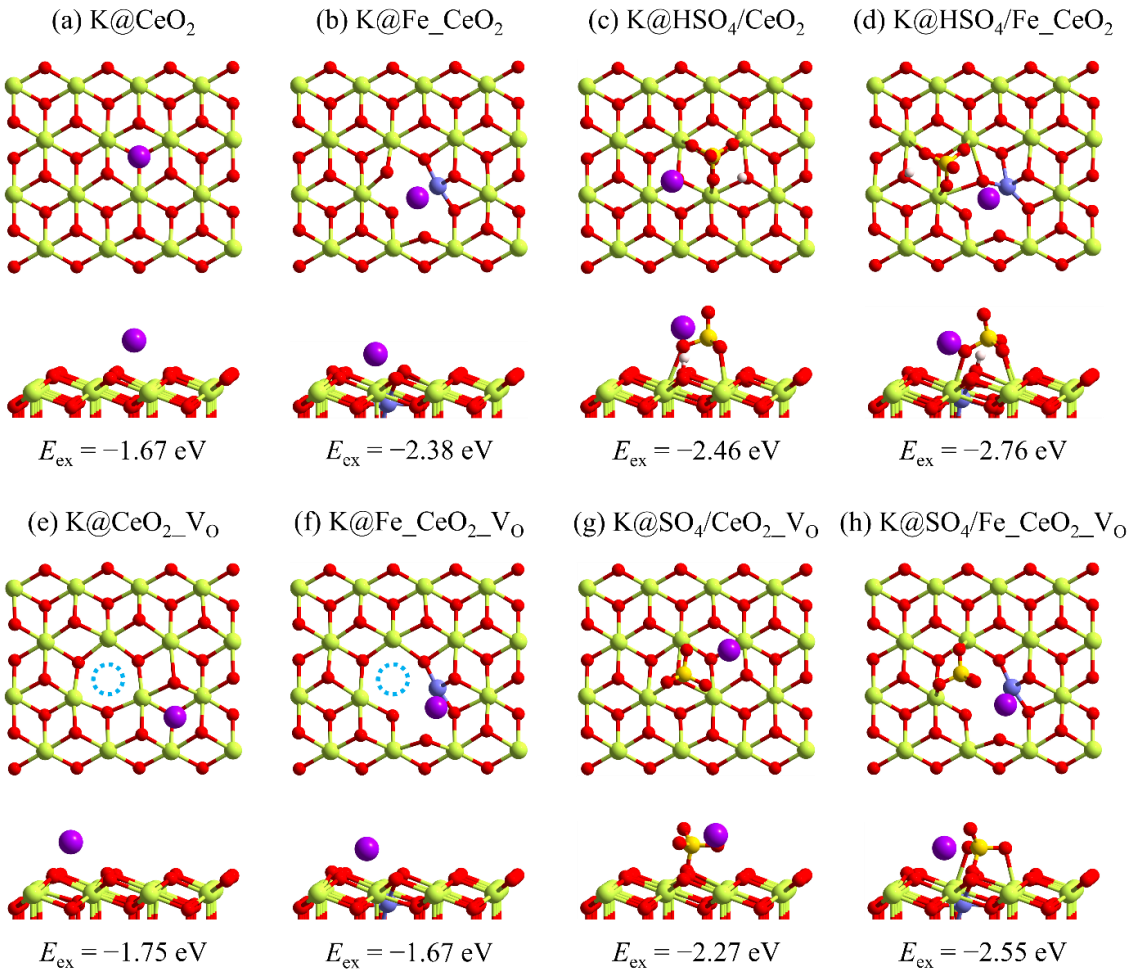


Figure S10. K@surface produced after K-H exchange reaction. The dashed circle indicates the position of V_O. E_{ex} is exchange energy: $E_{ex} = E_{K@Surface} + 1/2E_{H_2O(g)} - E_{H@Surface} - 1/2E_{K_2O(g)}$.

S8. Adsorption Structure of NH_3 on Each Surface.

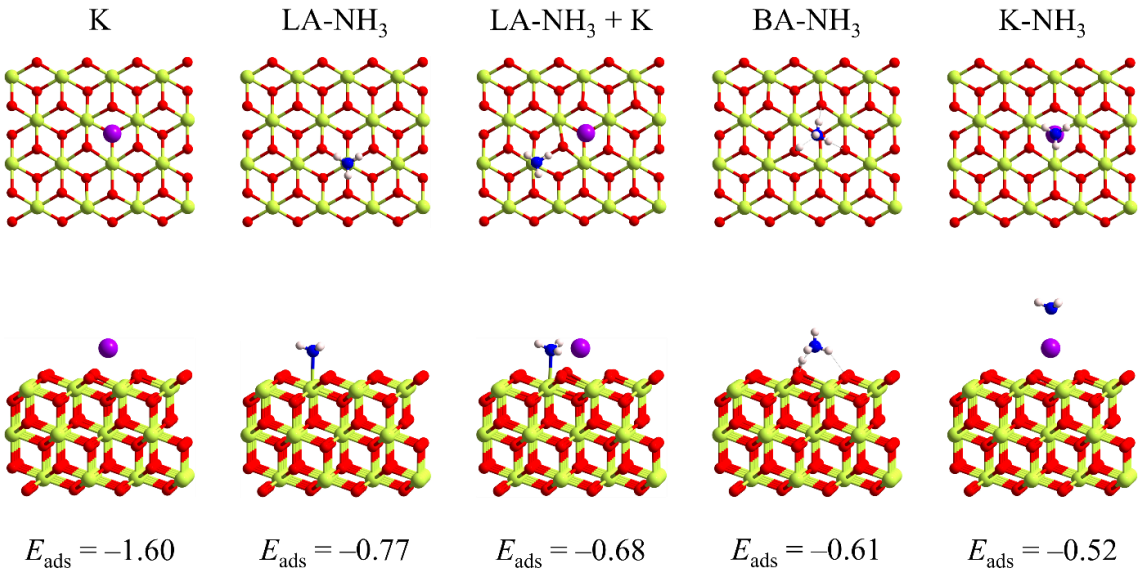


Figure S17. Adsorption of NH_3 on CeO_2 surface with and without K species. Unit for adsorption energy, eV. The adsorption energy of K was calculated as: $E_{ads} = E_{K@Surface} + 1/4E_{O2(g)} - E_{Surface} - 1/2E_{K2O(g)}$. The adsorption energy of NH_3 was calculated as: $E_{ads} = E_{NH3@Surface} - E_{Surface} - E_{NH3(g)}$.

S9. Multiple K Adsorption.

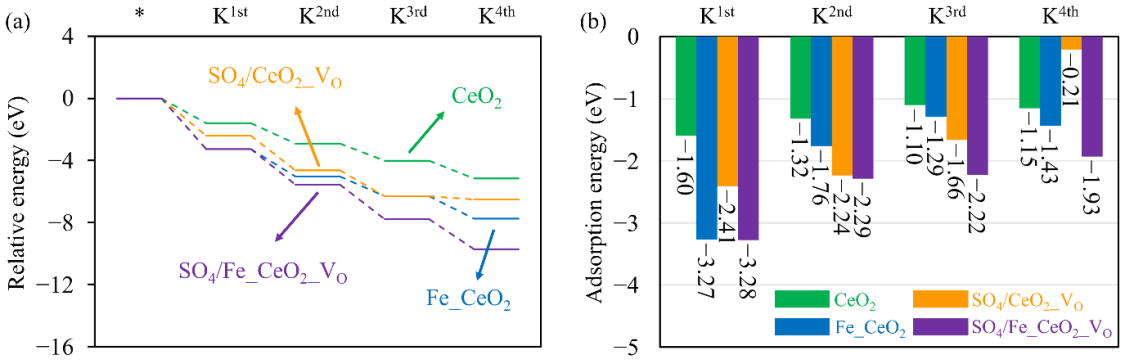


Figure S18. (a) Adsorption energies of the K atoms on the CeO_2 surface (green line) the Fe_CeO_2 surface (blue line), the SO_4/CeO_2_V_O surface (orange line) and the SO_4/Fe_CeO_2_V_O surface (purple line) relative to the isolated surface and the K atoms. (b) Adsorption energies of the n^{th} K atoms relative to the $(n-1)^{th}$@surface. The dashed line indicates the adsorption energy of K on the CeO_2 surface. * represents the surface without adsorbates.

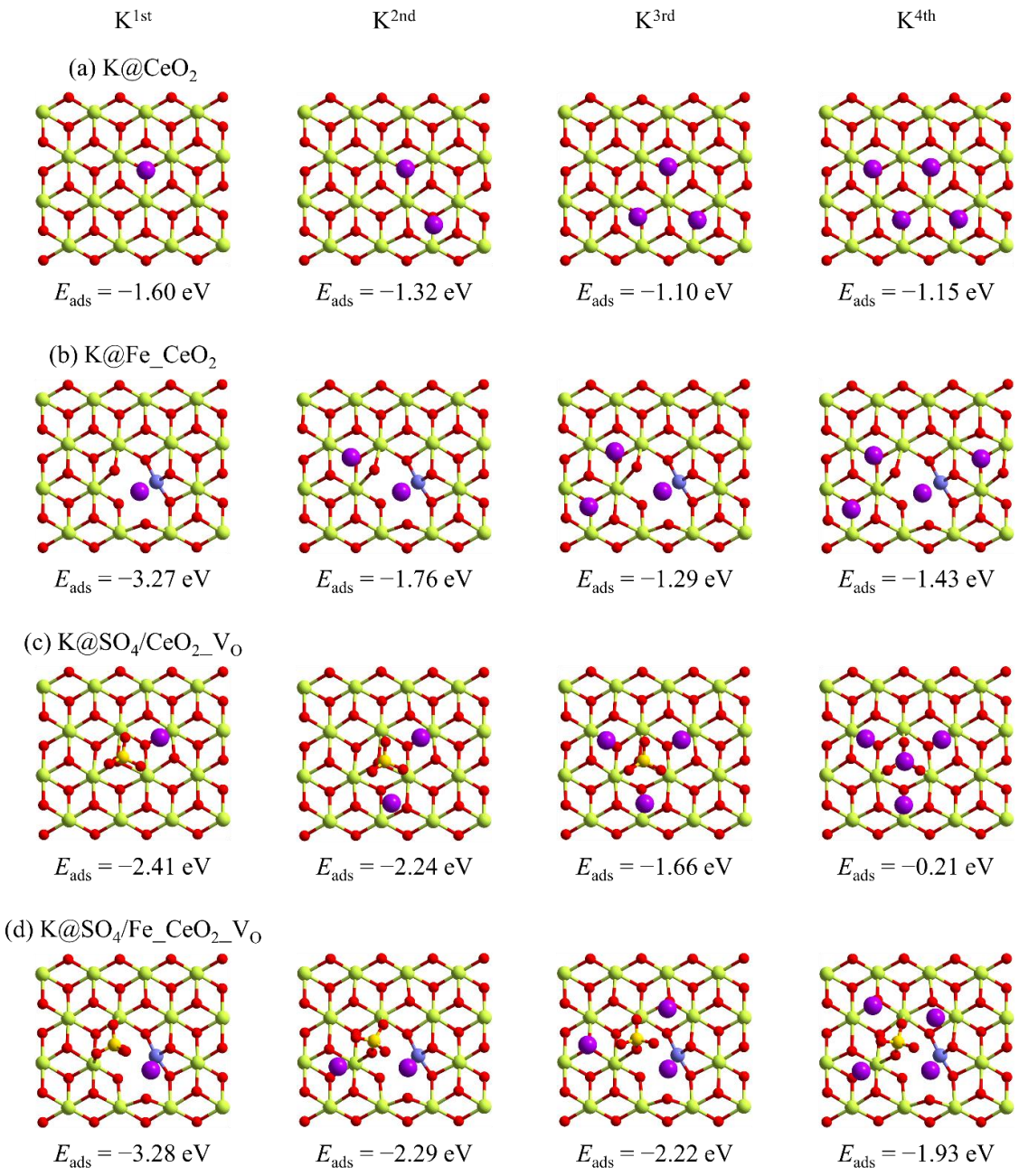


Figure S19. Adsorption structures of the K atoms on each surface model.

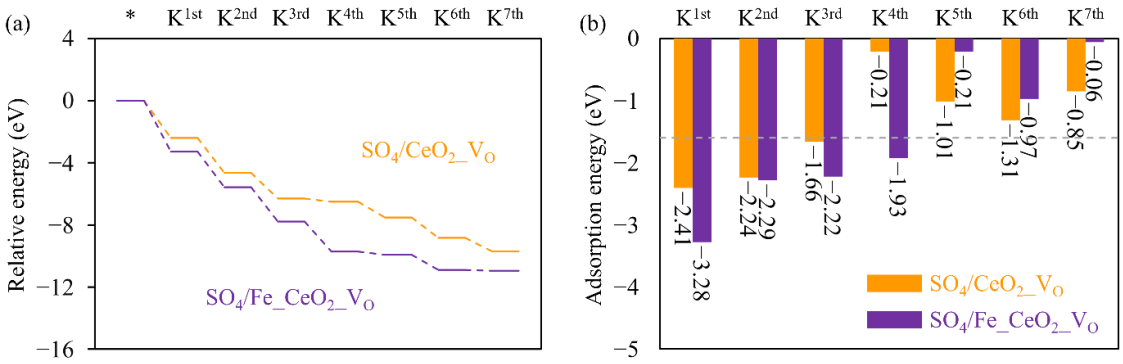


Figure S20. (a) Adsorption energies of the K atoms on the $SO_4/CeO_2_V_O$ surface (orange line) and the $SO_4/Fe_CeO_2_V_O$ surface (purple line) relative to the isolated surface and the K atoms. (b) Adsorption energies of the n^{th} K atoms relative to the $(n-1)^{th}$@surface. * represents the surface without adsorbates.

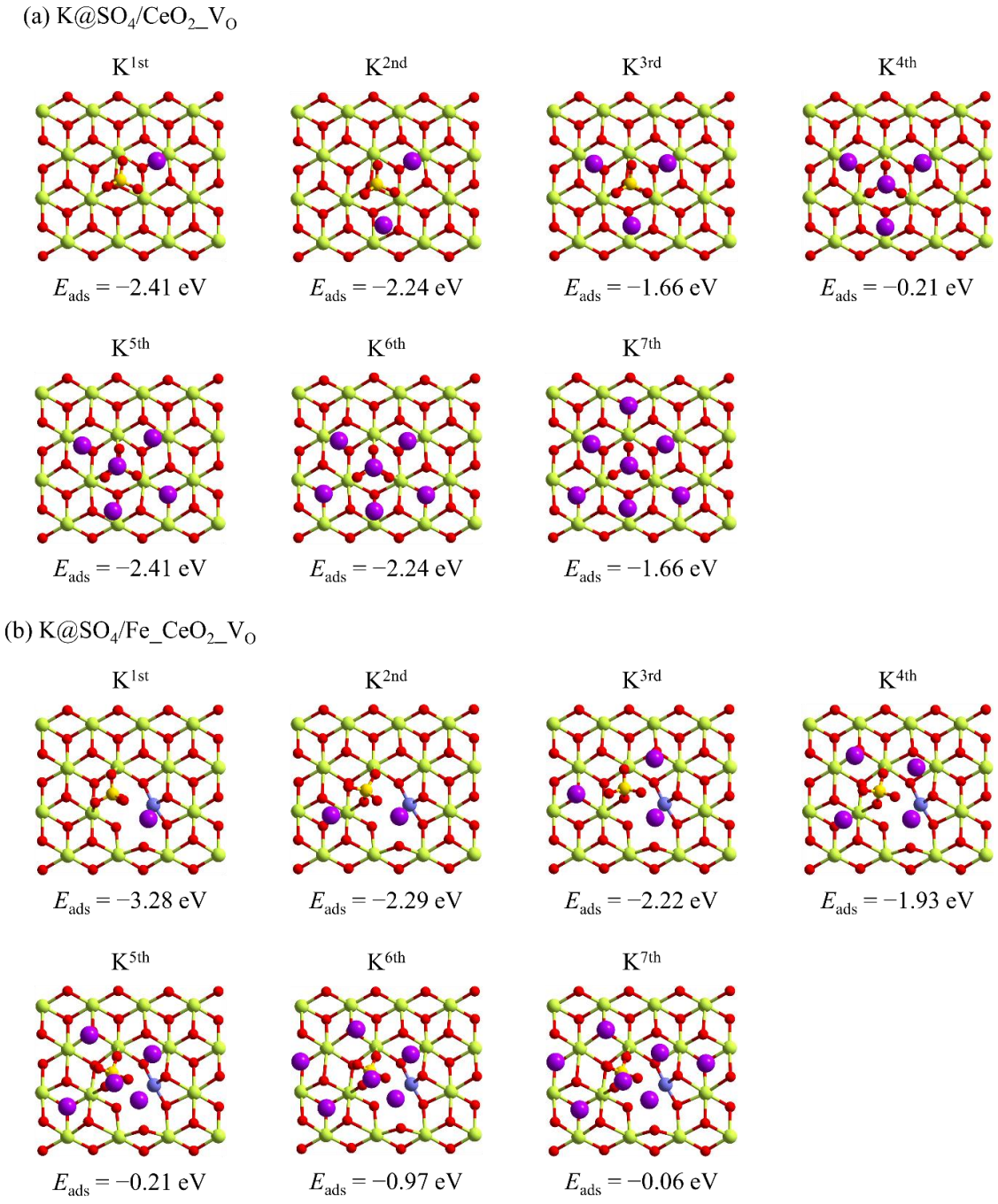


Figure S21. Adsorption structures of the K atoms on each surface model.

2.6. References

(1) Han, L.; Cai, S.; Gao, M.; Hasegawa, J.-y.; Wang, P.; Zhang, J.; Shi, L.; Zhang, D. Selective catalytic reduction of NO_X with NH_3 by using novel catalysts: State of the Art and Future Prospects. *Chem. Rev.* **2019**, *119*, 10916–10976.

(2) Sander, B. Properties of Danish biofuels and the requirements for power production. *Biomass Bioenergy* **1997**, *12*, 177–183.

(3) Chen, J. P.; Buzanowski, M. A.; Yang, R. T.; Cichanowicz, J. E. Deactivation of the Vanadia Catalyst in the Selective Catalytic Reduction Process. *J. Air Waste Manag. Assoc.* **1990**, *40*, 1403–1409.

(4) Kamata, H.; Takahashi, K.; Odenbrand, C. U. I. The role of K_2O in the selective reduction of NO with NH_3 over a $V_2O_5(WO_3)/TiO_2$ commercial selective catalytic reduction catalyst. *J. Mol. Catal. A: Chem.* **1999**, *139*, 189–198.

(5) Chen, L.; Li, J.; Ge, M. The poisoning effect of alkali metals doping over nano V_2O_5–WO_3/TiO_2 catalysts on selective catalytic reduction of NO_X by NH_3. *Chem. Eng. J.* **2011**, *170*, 531–537.

(6) Wu, P.; Tang, X.; He, Z.; Liu, Y.; Wang, Z. Alkali Metal Poisoning and Regeneration of Selective Catalytic Reduction Denitration Catalysts: Recent Advances and Future Perspectives. *Energy Fuels* **2022**, *36*, 5622-5646.

(7) Kong, M.; Liu, Q.; Zhou, J.; Jiang, L.; Tian, Y.; Yang, J.; Ren, S.; Li, J. Effect of different potassium species on the deactivation of V_2O_5-WO_3/TiO_2 SCR catalyst: Comparison of K_2SO_4, KCl and K2O. *Chem. Eng. J.* **2018**, *348*, 637–643.

(8) Peng, Y.; Li, J.; Si, W.; Li, X.; Shi, W.; Luo, J.; Fu, J.; Crittenden, J.; Hao, J. Ceria promotion on the potassium resistance of MnO_x/TiO_2 SCR catalysts: An experimental and DFT study. *Chem. Eng. J.* **2015**, *269*, 44–50.

(9) Fang, Q.; Zhu, B.; Sun, Y.; Song, W.; Xu, M. Effects of alkali metal poisoning and cobalt modification on the NH_3 adsorption behavior on the Mn_xO_y/Ni (1 1 1) surface: A DFT-D study. *Appl. Surf. Sci.* **2020**, *509*, 144901.

(10) Zhou, X. J.; Sun, Y.; Zhu, B.; Chen, J.; Xu, J.; Yu, H.; Xu, M. Influencing mechanism of alkali metals on the adsorption property of NH_3, NO, O_2 and dehydrogenation reaction of NH_3 on the β-MnO_2 (1 1 0) surface: A DFT + U study. *Fuel* **2022**, *318*.

(11) Wei, L.; Cui, S.; Guo, H.; Zhang, L. The effect of alkali metal over Mn/TiO_2 for low-temperature SCR of NO with NH_3 through DRIFT and DFT. *Comput. Mater. Sci.* **2018**, *144*, 216-222.

(12) Lyu, Z.; Niu, S.; Han, K.; Lu, C.; Li, Y. Theoretical insights into the poisoning effect of Na and K on α-Fe_2O_3 catalyst for selective catalytic reduction of NO with NH_3. *Appl. Catal., A* **2021**, *610*.

(13) Jiang, Y.; Lai, C.; Li, Q.; Gao, W.; Yang, L.; Yang, Z.; Lin, R.; Wang, X.; Zhu, X. The poisoning effect of KCl and K_2O on CeO_2-TiO_2 catalyst for selective catalytic reduction of NO with NH_3. *Fuel* **2020**, *280*, 118638.

(14) Jiang, Y.; Liu, T.; Lai, C.; Yang, Z.; Lin, R.; Wang, X.; Zhu, X. Deactivation of CeO_2-TiO_2 catalyst by K_2SO_4 for NH_3-SCR: An experimental and DFT study. *Appl. Surf. Sci.* **2021**, *547*, 149196.

(15) Gao, S.; Wang, P.; Chen, X.; Wang, H.; Wu, Z.; Liu, Y.; Weng, X. Enhanced alkali resistance of CeO_2/SO_4^{2-}–ZrO_2 catalyst in selective catalytic reduction of NO_X by ammonia. *Catal. Commun.* **2014**, *43*, 223–226.

(16) Zhou, G.; Maitarad, P.; Wang, P.; Han, L.; Yan, T.; Li, H.; Zhang, J.; Shi, L.; Zhang, D. Alkali-resistant NO_X reduction over SCR catalysts via boosting NH_3 adsorption rates by in situ constructing the sacrificed sites. *Environ. Sci. Technol.* **2020**, *54*, 13314–13321.

(17) Khan, M. N.; Han, L.; Wang, P.; Zhang, D. Tailored alkali resistance of $DeNO_X$ catalysts by improving redox properties and activating adsorbed reactive species. *iScience* **2020**, *23*, 101173.

(18) Zhou, Z.; Lan, J.; Liu, L.; Liu, Z. Enhanced alkali resistance of sulfated CeO_2 catalyst for the reduction of NO_X from biomass fired flue gas. *Catal. Commun.* **2021**, *149*.

(19) Kresse, G.; Furthmuller, J. Efficiency of ab-initio total energy calculations for metals and semiconductors using a plane-wave basis set. *Comput. Mater. Sci.* **1996**, *6*, 15–50.

(20) Kresse, G.; Hafner, J. *Ab initio* molecular dynamics for liquid metals. *Phys. Rev. B* **1993**, *47*, 558–561.

(21) Kresse, G.; Joubert, D. From ultrasoft pseudopotentials to the projector augmented-wave method. *Phys. Rev. B* **1999**, *59*, 1758–1775.

(22) Bengone, O.; Alouani, M.; Blöchl, P.; Hugel, J. Implementation of the projector augmented-wave LDA+U method: Application to the electronic structure of NiO. *Phys. Rev. B* **2000**, *62*, 16392–16401.

(23) Blöchl, P. E. Projector augmented-wave method. *Phys. Rev. B* **1994**, *50*, 17953–17979.

(24) Grimme, S.; Antony, J.; Ehrlich, S.; Krieg, H. A consistent and accurate *ab initio* parametrization of density functional dispersion correction (DFT-D) for the 94 elements H-Pu. *J. Chem. Phys.* **2010**, *132*, 154104.

(25) Perdew, J. P.; Burke, K.; Ernzerhof, M. Generalized gradient approximation made simple. *Phys. Rev. Lett.* **1996**, *77*, 3865–3868.

(26) Dudarev, S. L.; Botton, G. A.; Savrasov, S. Y.; Humphreys, C. J.; Sutton, A. P. Electron-energy-loss spectra and the structural stability of nickel oxide: An LSDA+U study. *Phys. Rev. B* **1998**, *57*, 1505–1509.

(27) Jain, A.; Ong, S. P.; Hautier, G.; Chen, W.; Richards, W. D.; Dacek, S.; Cholia, S.; Gunter, D.; Skinner, D.; Ceder, G.; et al. Commentary: The Materials Project: A materials genome approach to accelerating materials innovation. *APL Mater.* **2013**, *1*.

(28) Jiang, Y.; Adams, J. B.; van Schilfgaarde, M. Density-functional calculation of CeO_2 surfaces and prediction of effects of oxygen partial pressure and temperature on stabilities. *J. Chem. Phys.* **2005**, *123*, 64701.

(29) Prieur, D.; Bonani, W.; Popa, K.; Walter, O.; Kriegsman, K. W.; Engelhard, M. H.; Guo, X.; Eloirdi, R.; Gouder, T.; Beck, A.; et al. Size dependence of lattice parameter and electronic structure in CeO_2 nanoparticles. *Inorg. Chem.* **2020**, *59*, 5760–5767.

(30) Wang, V.; Xu, N.; Liu, J.-C.; Tang, G.; Geng, W.-T. VASPKIT: A user-friendly interface facilitating high-throughput computing and analysis using VASP code. *Comput. Phys. Commun.* **2021**, *267*, 108033.

(31) Momma, K.; Izumi, F. *VESTA 3* for three-dimensional visualization of crystal, volumetric and morphology data. *J. Appl. Crystallogr.* **2011**, *44*, 1272–1276.

(32) Tian, D.; Li, K.; Wei, Y.; Zhu, X.; Zeng, C.; Cheng, X.; Zheng, Y.; Wang, H. DFT insights into oxygen vacancy formation and CH_4 activation over CeO_2 surfaces modified by transition metals (Fe, Co and Ni). *Phys. Chem. Chem. Phys.* **2018**, *20*, 11912-11929.

(33) Lu, Y.-H.; Chen, H.-T. Computational Investigation of NO_2 Adsorption and Reduction on Ceria and M-Doped CeO_2 (111) (M = Mn, Fe) Surfaces. *J. Phys. Chem. C* **2014**, *118*, 10043-10052.

(34) Chu, K.; Cheng, Y.-h.; Li, Q.-q.; Liu, Y.-p.; Tian, Y. Fe-doping induced morphological changes, oxygen vacancies and Ce^{3+}–Ce^{3+} pairs in CeO_2 for promoting electrocatalytic nitrogen fixation. *J. Mater. Chem. A* **2020**, *8*, 5865-5873.

(35) Khare, A.; Choudhary, R. J.; Phase, D. M.; Sanyal, S. P. Electronic structure studies of Fe doped CeO_2 thin films by resonance photoemission spectroscopy. *J. Appl. Phys.* **2011**, *109*, 123706.

(36) Fan, J.; Ning, P.; Song, Z.; Liu, X.; Wang, L.; Wang, J.; Wang, H.; Long, K.; Zhang, Q. Mechanistic aspects of NH_3-SCR reaction over CeO_2/TiO_2-ZrO_2-SO_4^{2-} catalyst: In situ DRIFTS investigation. *Chem. Eng. J.* **2018**, *334*, 855–863.

(37) Wang, S.; Fan, C.; Zhao, Z.; Liu, Q.; Xu, G.; Wu, M.; Chen, J.; Li, J. A facile and controllable *in situ* sulfation strategy for CuCeZr catalyst for NH_3-SCR. *Appl. Catal., A* **2020**, *597*, 117554.

(38) Zhang, Q.; Zhang, J.; Song, Z.; Ning, P.; Li, H.; Liu, X. A novel and environmentally friendly SO_4^{2-} /CeO_2 catalyst for the selective catalytic reduction of NO with NH_3. *J. Ind. Eng. Chem.* **2016**, *34*, 165-171.

(39) Kuczkowski, R. L.; Suenram, R. D.; Lovas, F. J. Microwave spectrum, structure, and dipole moment of sulfuric acid. *J. Am. Chem. Soc.* **1981**, *103*, 2561–2566.

(40) Kotomin, E. A.; Mastrikov, Y. A.; Kuklja, M. M.; Merkle, R.; Roytburd, A.; Maier, J. First principles calculations of oxygen vacancy formation and migration in mixed conducting $Ba_{0.5}Sr_{0.5}Co_{1-y}Fe_yO_{3-\delta}$ perovskites. *Solid State Ion.* **2011**, *188*, 1–5.

(41) Piotrowski, M. J.; Tereshchuk, P.; Da Silva, J. L. F. Theoretical Investigation of Small Transition-Metal Clusters Supported on the CeO_2(111) surface. *J. Phys. Chem. C.* **2014**, *118*, 21438–21446.

(42) Montini, T.; Melchionna, M.; Monai, M.; Fornasiero, P. Fundamentals and catalytic applications of CeO_2-based materials. *Chem. Rev.* **2016**, *116*, 5987–6041.

(43) Zhang, B.; Zhang, S.; Liu, B. Effect of oxygen vacancies on ceria catalyst for selective catalytic reduction of NO with NH_3. *Appl. Surf. Sci.* **2020**, *529*, 147068.

(44) Liu, B.; Liu, J.; Ma, S.; Zhao, Z.; Chen, Y.; Gong, X.-Q.; Song, W.; Duan, A.; Jiang, G. Mechanistic study of selective catalytic reduction of NO with NH_3 on W-doped CeO_2 catalysts: Unraveling the catalytic cycle and the role of oxygen vacancy. *J. Phys. Chem. C.* **2016**, *120*, 2271–2283.

(45) Song, W.; Liu, J.; Zheng, H.; Ma, S.; Wei, Y.; Duan, A.; Jiang, G.; Zhao, Z.; Hensen, E. J. M. A mechanistic DFT study of low temperature SCR of NO with NH_3 on $MnCe_{1-x}O_2$(111). *Catal. Sci. Technol.* **2016**, *6*, 2120–2128.

(46) Chen, Y.; Hu, P.; Lee, M.-H.; Wang, H. Au on (1 1 1) and (1 1 0) surfaces of CeO_2: A density-functional theory study. *Surface Science* **2008**, *602*, 1736–1741.

(47) Reuter, K.; Scheffler, M. Composition, structure, and stability of RuO_2(110) as a function of oxygen pressure. *Phys. Rev. B* **2001**, *65*, 035406.

(48) Tetens, O. Über einige meteorologische Begriffe. *Z. Geophys.* **1930**, *6*, 297–309.

(49) Chase, W. M. NIST-JANAF Thermochemical Tables. *J. Phys. Chem. Ref. Data Monograph 9;* **1998**.

(50) Qiao, D.; Lu, G.; Liu, X.; Guo, Y.; Wang, Y.; Guo, Y. Preparation of $Ce_{1-x}Fe_xO_2$ solid solution and its catalytic performance for oxidation of CH_4 and CO. *J. Mater. Sci.* **2011**, *46*, 3500–3506.

(51) Zhang, X.; Wang, J.; Song, Z.; Zhao, H.; Xing, Y.; Zhao, M.; Zhao, J.; Ma, Z. a.; Zhang, P.; Tsubaki, N. Promotion of surface acidity and surface species of doped Fe and SO_4^{2-} over CeO_2 catalytic for NH_3-SCR reaction. *Mol. Catal.* **2019**, *463*, 1–7.

Chapter 3. Constructing Machine-Learning Force Field Describing Oxygen Vacancy on CeO_2 Surfaces

3.1. Introduction

Metal oxide catalysts are crucial in various industrial and environmental processes due to their exceptional catalytic properties, stability, and versatility.[1,2] The unique ability of metal oxides to facilitate redox reactions, adsorb and activate reactant, and withstand harsh operating conditions makes them indispensable in modern catalytic technologies. One of the most extensively studied metal oxides is cerium dioxide (CeO_2), renowned for its oxygen storage capacity and redox flexibility. CeO_2 is widely employed in automotive catalytic converters,[3,4] solid oxide fuel cells,[5] and catalyst supports[6] in various chemical reactions. Oxygen vacancies in CeO_2 enhance its catalytic performance by providing active sites for reactant adsorption and facilitating oxygen mobility, which is crucial for reactions such as CO oxidation,[7,8] water-gas shift,[9,10] and methane reforming.[11] Understanding the formation, stability, and diffusion of oxygen vacancies on CeO_2 surfaces is essential for optimizing catalytic efficiency and extending applications. For example, in the selective catalytic reduction of nitrogen oxides with ammonia (NH_3-SCR), oxygen vacancies facilitate the activation of reactants and influence reaction pathways,[12-14] making them central to improving catalytic performance. Our previous theoretical studies using density functional theory (DFT) calculations indicated that additives facilitate the formation of oxygen vacancies on the surface of CeO_2. Additionally, the adsorption sites generated in this process significantly affect the alkali metal tolerance of NH_3-SCR.[15] However, a key challenge still exists in understanding more realistic CeO_2 surfaces.

Simulating realistic catalytic surfaces with oxygen vacancies on CeO_2 poses significant computational challenges. Vacancy configurations vary across different

facets, which can significantly impact catalytic properties. While pristine CeO_2 surfaces, such as the high-symmetry (100), (110), and (111) facets, contain relatively few inequivalent lattice oxygen sites, surfaces with step structures, such as (221) and (331) present numerous lattice oxygen sites with differing symmetries. This diversity necessitates a comprehensive screening of oxygen vacancy configurations to capture their role in catalytic activity accurately. Traditional computational approaches, such as density functional theory (DFT), offer valuable insights into the electronic structure of metal oxide surfaces and reaction pathways. However, the high computational cost of DFT limits its applicability to large-scale systems and extensive sampling of dynamic processes like oxygen vacancy diffusion.

Recent advancements in machine learning (ML) have opened new avenues for overcoming these limitations. Machine learning force fields (MLFF) have emerged as powerful tools for simulating the behavior of complex materials with near-DFT accuracy but at a fraction of the computational expense. By training on DFT data, MLFF can predict atomic forces and energies for new configurations, enabling large-scale MD simulations that capture the dynamic nature of catalyst surfaces. This capability is particularly advantageous for studying metal oxide catalysts, where the ability to model extensive surface areas and diverse vacancy configurations is crucial for a comprehensive understanding of catalytic mechanisms.

In recent years, there has been active investigation into the application of MLFF to surface science.[16,17] As an application to phenomena on metal surfaces, Halim et al. simulated the diffusion of Cu clusters on a Cu (111) facet under CO conditions[18] using a Gaussian approximation potential (GAP)[19] based MLFF implemented in the FLARE

code.[20] They examined the effect of CO exposure and temperature on the diffusion process of Cu clusters. Their ML molecular dynamics (MD) simulations successfully reproduced the decomposition of the Cu surface into nanoclusters upon CO exposure, aligning with experimental results.[21] Youkaichiya et al. proposed a scheme to evaluate adsorption and activation energies of elementary steps on the fly by kinetic Monte Carlo (kMC) simulations combined with neural network potentials (NNP).[22] They applied the method to the diffusion process of H_2 on Pd(111) and the CO oxidation reaction on Pt(111), suggesting that the lateral interaction has an important influence on catalysis. Several applications of MLFF and NNP on the surface science of metal oxide have also been reported. For example, Timmermann et al. applied GAP to global surface structure determination and assessed the stability of various termination structures of IrO_2 and RuO_2 surfaces.[23] Their calculations suggested that novel termination structures exist, which are more stable than previous ones, including the metal-rich (101) structure; experiments also confirmed the structure. Kobayashi et al. conducted NNP-based reactive MD simulations at the water/CeO_2 interface.[24] They proposed enhanced sampling methods and refinement schemes to constrcut reliable NNP and demonstrated the need for sufficiently large models and longer simulation times to estimate reaction rates accurately. They also applied the constructed NNP to compare the water interface on the CeO_2(111) and CeO_2(110) surfaces, finding that proton hopping is more active on the (111) surface than on the (110) surface.

The accuracy of a machine-learning force field (MLFF) depends on the quality of the training data. There is room for improvement in efficiently constructing a database to generate an MLFF capable of accurately describing complex properties. In this study, I introduce an efficient strategy for building an MLFF tailored to CeO_2 surface modeling,

utilizing an on-the-fly method implemented in VASP. Our approach leverages systematic on-the-fly training, starting from small slab models and incorporating varied atomic configurations through controlled temperature increases in MD simulations. By comparing different initial structures, optimizing dataset merging, and testing on diverse ceria surface models, I aim to develop an MLFF capable of accurately capturing oxygen vacancy diffusion and surface stability with minimal computational resources. This work advances MLFF methodologies for simulating complex oxide surfaces, offering scalable techniques for studying realistic catalyst surfaces at the atomic level.

3.2. Computational Details

Density Functional Theory (DFT) calculations were conducted under periodic boundary conditions using the Vienna Ab initio Simulation Package (VASP) version 6.4.2.[25,26] The Projector Augmented Wave (PAW) method was employed, incorporating spin polarization and van der Waals corrections (DFT-D3).[27] The calculations utilized the Perdew–Burke–Ernzerhof (PBE) exchange-correlation functional within the generalized gradient approximation (GGA). A (1 × 1 × 1) gamma-centered k-point grid was used for Brillouin zone sampling, and the cutoff energy was set to 520 eV. The on-site Coulomb interactions of the Ce 4f states were accounted for using the Hubbard U correction method (DFT+U),[28] with U = 5.0 and J = 0.0 eV. The crystal structure of bulk CeO_2 was obtained from the Materials Project database.[29] The computed lattice constant is 5.48 Å, aligning well with the theoretical value of 5.49–5.50 Å[30-33] and the experimental value of 5.41 Å.[34]

The oxygen vacancy diffusion pathway was calculated using the climbing image nudged elastic band (CI-NEB) method implemented in VTST Tools.[35] The datasets of

structures acquired on the fly were combined using pymlff,[36] a Python package for merging VASP ML_AB files.

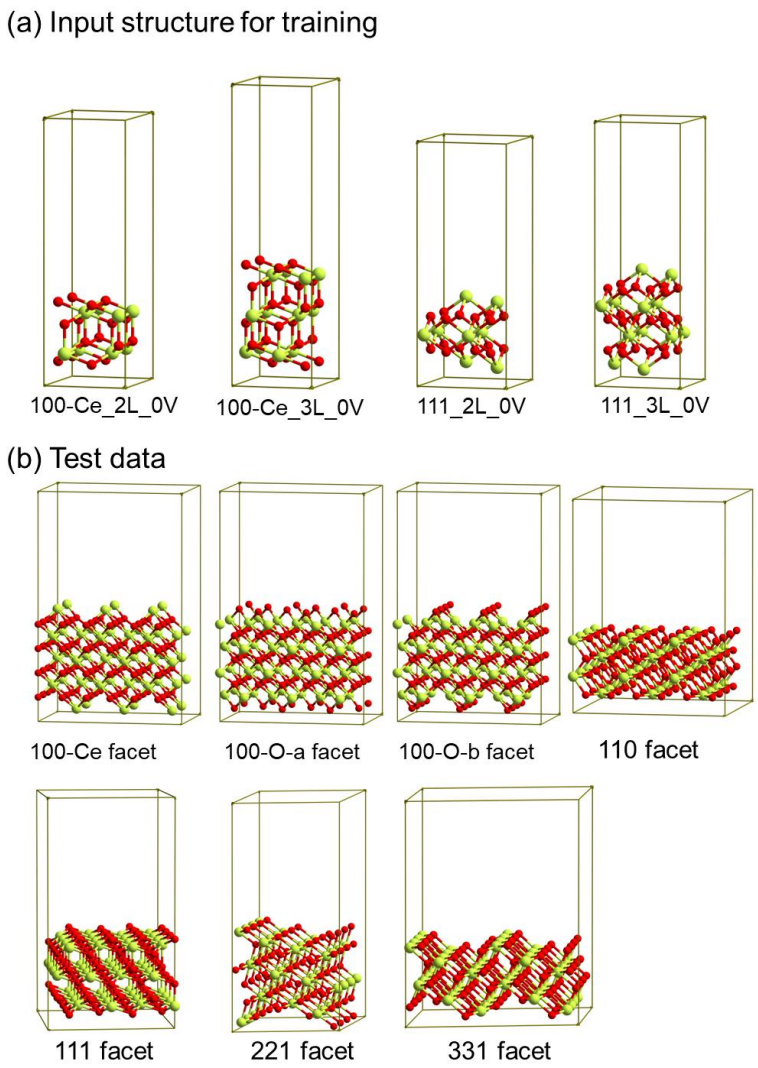


Fig. 1. (a) side view of the initial structures (small slab model) used for on-the-fly training. The labels "2L" and "3L" refer to a two-layer model with 24 atoms and a three-layer model with 36 atoms, respectively. Additionally, "0V" indicates that there are no oxygen vacancies. (b) side view of a medium slab model containing 144 atoms, which is used for validating the trained machine learning force field (MLFF) models.

Relative to the training of the MLFF, the MD was done by the NVT ensemble using the Langevin thermostat.[37,38] LANGEVIN_GAMMA, which specifies the friction coefficients (in ps^{-1}) for atomic degrees-of-freedom when using a Langevin thermostat, was set to 10 for Ce and O, respectively.

The number of MD steps for on-the-fly training of MLFF was set to 10,000 for each input structure. The temperature was gradually increased from 300 K to 4,000 K for the initial 2,000 steps, and the following 8,000 steps were done at 4,000K. This approach ensures a diverse training dataset and prevents rapid atomic movement, which helps avoid collisions between atoms. Such collisions generate significant forces, making it difficult to control the system and potentially causing the entire simulation to terminate unexpectedly.

The parameter determining the threshold value (ML_CTIFOR) was set to 0.5, 1.5 times the default value. This adjustment reduces the number of density functional theory (DFT) calculations performed after 2,000 steps of MD simulations and makes sampling sparser. Besides, In the default setting for on-the-fly learning in VASP, when the number of local reference structures used for training reaches 1,500, the first acquired structure is discarded as new structures are added to the training dataset. To ensure that configurations from all regions of the learning step are included in the training data, the value of ML_SCLC_CTIFOR was increased from the default of 0.6 to 0.8. This change slightly reduces the local reference configurations obtained from one selected structure. Additionally, the upper limit for the number of local reference configurations was increased from 1,500 to 3,000 using the ML_MB tag.

The target surface structure, particularly its interior, shares the same crystal structure, making it also important to sample structures close to this crystal structure adequately. Therefore, the heating run, which involves a gradual increase in temperature, gives the MLFF sufficient time to learn the characteristics of the crystal structure. Additionally, every 1,000 steps, structural optimization calculations were performed using the trained MLFF on seven medium slab models, each consisting of 144 atoms. The results from these calculations were then compared with those obtained from DFT.

3.3. Results and Discussion

Firstly, the effect of the initial structure on the efficient training of the MLFF was investigated. As shown in Fig. 1a, four small-scale slab models of 24 and 36 atoms were used as the input structure for on-the-fly MLFF training. Initially, the most stable (111) surface and the most unstable (100) surface[32] were chosen for the initial geometry in MD sampling. Ce-terminated (100) facet (100-Ce) with 2 and 3 layers, as well as (111) facet with 2 and 3 layers, were employed as the initial structures.

During simulations, Density Functional Theory (DFT) calculations are performed when the estimated error in forces exceeds a certain threshold. VASP sets this threshold as the average estimated error over the last ten steps. Fig. S1 illustrates the trends in threshold updates and force errors for on-the-fly runs. An increase in the root mean square error indicates that DFT calculations are selectively conducted for structures with more significant errors. It was confirmed that over 90% of DFT calculations were skipped, allowing for more efficient structural sampling during on-the-fly runs.

In this study, medium slab models, for which DFT calculations could be performed, were used for accuracy verification. Seven surface structures, as shown in Fig. 1b, each

consisting of 144 atoms, were selected to test the accuracy of the machine learning potential. These included one (100) surfaces with Ce termination, two coordinated O termination (100-O-a), (100-O-b), and the (110), (111), (221), and (331) surfaces. To assess the accuracy of the MLFF, each medium slab—with and without an oxygen vacancy—was optimized using the MLFF obtained through MD simulations. For each surface model, the location of the oxygen vacancy was selected from various possible positions. The selected oxygen vacancy locations are shown in Fig. S2. Seven pristine surface geometries and 30 geometries with an oxygen vacancy were analyzed. The accuracy was evaluated by the Root Mean Square Error (RMSE) of the total system energies using the following equation:

$$\mathrm{RMSE} = \sqrt{\frac{1}{n}\Sigma_{i=1}^{n}({}^{\mathrm{DFT}}E_{\mathrm{r}}^{n} - {}^{\mathrm{MLFF}}E_{\mathrm{r}}^{n})^{2}}$$

Where

$$E_{\mathrm{r}}^{n} = E^{\mathrm{xyz\ facet}} - E^{111\ \mathrm{facet}}$$

n indicates the number of configurations considered for accuracy evaluation, *n* = 7 for pristine surfaces (Fig. 2a), and *n* = 30 for the surface with oxygen vacancy. ${}^{\mathrm{DFT}}E_{\mathrm{r}}^{n}$ is the relative DFT value for each geometry, and ${}^{\mathrm{MLFF}}E_{\mathrm{r}}^{n}$ is the predicted relative energy.

The MLFF was evaluated for every 1,000 steps on the training run. Figure 2a shows the RMSE of the relative energy for seven pristine surfaces after structure optimizations. Fig. 2b illustrates the RMSE for 30 oxygen vacancy surfaces. Training with the unstable 100-Ce model minimized the RMSE at 2,000 steps, whereas training with the stable 111 model required 4,000 steps to minimize the RMSE (Fig. 2). I chose the 100-Ce model for further investigation because it offers relatively high accuracy with minimal data.

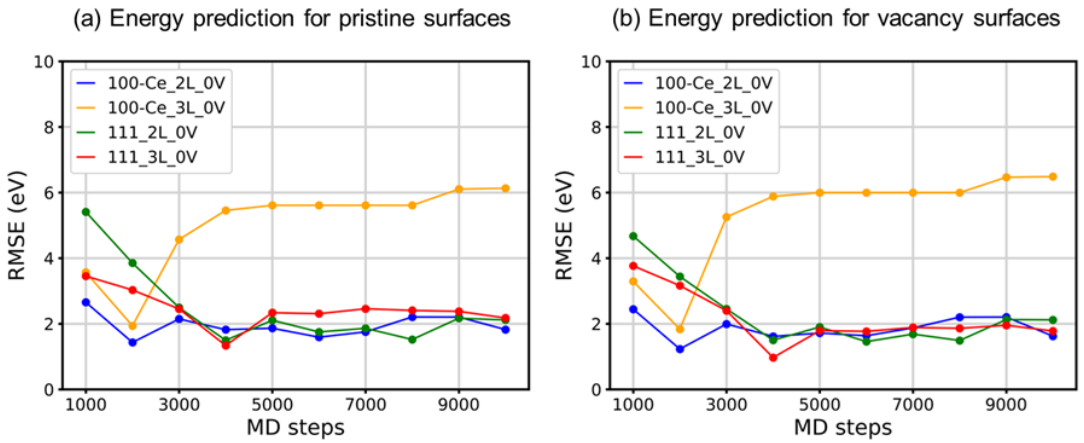


Fig. 2. The root mean square error (RMSE) changes in MLFF accuracy relative to the number of on-the-fly training (MD) steps are shown. The blue and orange colors indicate the RMSE of the MLFF when a 100-Ce facet, 2-layer, and 3-layer small slab is trained as the initial structure. In contrast, the green and red colors represent the RMSE of the MLFF when a 111 facet, 2-layer, and 3-layer small slab is trained as the initial structure. (a) This panel displays the RMSE of predicted relative energies for seven pristine surfaces (validation structure; 144 atoms, as shown in Fig. 1b). (b) This panel presents the RMSE of predicted relative energies for 30 surfaces (validation structures; 143 atoms, as shown in Fig. S2) that include a vacancy.

Although the structure used for training shown in Fig. 2 did not contain any oxygen vacancy, the RMSE for the clean surfaces (Fig. 2a) and the RMSE for the oxygen vacancy surfaces (Fig. 2b) are similar according to the training steps. The RMSE converges as the number of MD simulation steps increases to 3,000, except for the case of 100-Ce_3L_0V (orange line). It is considered that the rapid decline in accuracy after 3,000 training steps using 100-Ce_3L_0V results from sampling highly unstable structures, as shown in Fig. S3.

Table 1. Patterns of Merged Datasets

(a) RMSE of predicted energies for seven pristine surfaces

	100-Ce_2L_0V	**100-Ce_2L_1V**	**100-Ce_3L_0V**	**100-Ce_3L_1V**
	1.43 eV 9.9 meV/atom	1.65 eV 11.5 meV/atom	1.94 eV 13.5 meV/atom	1.50 eV 10.4 meV/atom
100-Ce_2L_0V		2.11 eV 14.7 meV/atom	2.56 eV 17.8 meV/atom	–
100-Ce_2L_1V			–	1.19 eV 8.3 meV/atom
100-Ce_3L_0V				0.46 eV 3.2 meV/atom

(b) RMSE of predicted energies for 30 surfaces with an oxygen vacancy

	100-Ce_2L_0V	**100-Ce_2L_1V**	**100-Ce_3L_0V**	**100-Ce_3L_1V**
	1.23 eV 8.6 meV/atom	1.50 eV 10.5 meV/atom	1.84 eV 12.8 meV/atom	1.58 eV 11.1 meV/atom
100-Ce_2L_0V		1.31 eV 9.1 meV/atom	2.63 eV 18.4 meV/atom	–
100-Ce_2L_1V			–	0.85 eV 6.0 meV/atom
100-Ce_3L_0V				0.48 eV 3.4 meV/atom

I tested whether merging the training data collected up to 2,000 steps from each on-the-fly run could enhance the accuracy of the machine learning force field (MLFF). Details of these results are shown in Figures S6 and S7. The patterns of the merged datasets and the corresponding RMSE for the resulting MLFF are summarized in Table 1. I examined the following combinations: datasets were constructed from the 2-layer and 3-layer 100-Ce models, with and without an oxygen vacancy. Each combination was evaluated independently. Additionally, on-the-fly runs were conducted on the initial structure of the 100-Ce model with an oxygen vacancy (see Fig. 2b). With the exception of the 100-Ce_3L_0V case, the RMSE showed little change, having nearly converged until the 2,000 steps. Combining the two layers of (100-Ce) surfaces, i.e., 100-Ce_2L_0V

and 100-Ce_2L_1V datasets, resulted in limited improvement in accuracy (Table 1). In addition, no improvement in accuracy was observed for the dataset from different layers, i.e., the 100-Ce_2L_0V and 100-Ce_3L_0V datasets. However, combining training data from the three-layer pristine surface model (100-Ce_3L_0V) and the oxygen vacancy surface (100-Ce_3L_1V) significantly improved the accuracy of MLFF (Fig. 3b,d).

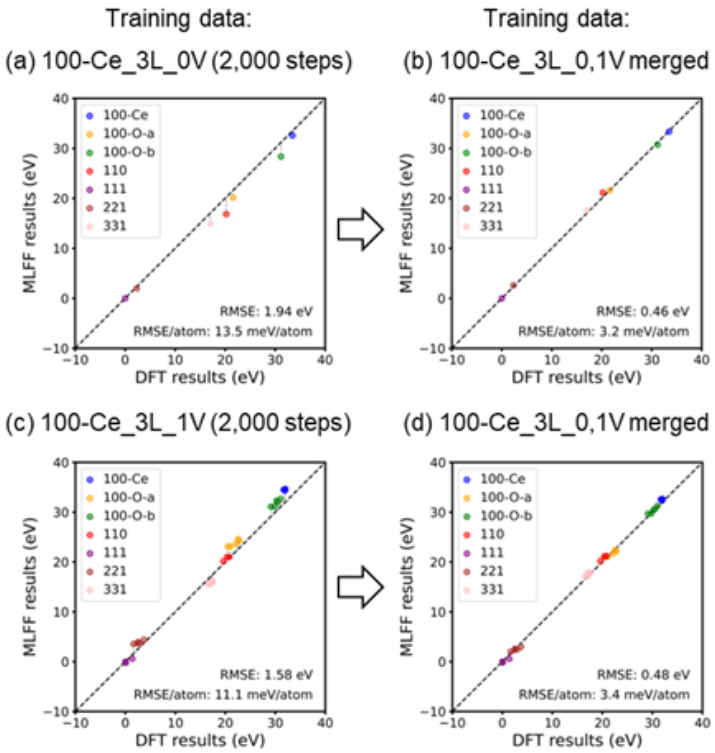


Fig. 3. The accuracy of a constructed machine learning force field (MLFF) based on datasets sampled from 100-Ce_3L_0V and 100-Ce_3L_1V as input structures. Using the 111 facets as a reference to compute relative energies. The MLFF was trained on the fly using the (a) 100-Ce_3L_0V and (c) 100-Ce_3L_1V. (b,d) trained on a merged dataset combining 100-Ce_3L_0V and 100-Ce_3L_1V. (a,b) are the results of structure optimization for seven pristine surfaces, and (c,d) are the results for 30 oxygen vacancy surfaces.

Fig. 3a shows the predicted relative energies after structure optimization for pristine surfaces and surfaces with an oxygen vacancy. Combining the 100-Ce_3L_0V and the 100-Ce_3L_1V dataset results in improved the accuracy of the relative energy prediction for pristine surfaces from 1.94 eV to 0.46 eV, and surface with an oxygen vacancy, 1.58 to 0.48 eV.

3.3.1. Oxygen Diffusion Pathways

To further assess the accuracy of the potential energy surface described by MLFF, simulations of lattice oxygen and oxygen vacancy diffusion processes were performed. Here, the diffusion pathways of an oxygen atom on various surfaces were evaluated using the MLFF constructed from the 100-Ce_3L_0V and 100-Ce_3L_1V datasets (see Fig. 3). The energy changes along the diffusion path were plotted in terms of total energy. Fig. 4 compares the diffusion pathways for lattice oxygen from Vac. 1 to Vac. 2 on the 100-Ce facet, calculated using MLFF and DFT. The diffusion pathway was calculated using the CI-NEB method. To visualize where the energy differences between DFT and MLFF are most significant, I plotted the energy change of each image by total energy. It is important to note that the structure used for training was a small-scale slab model; therefore, the total energies of the medium-scale slab model were not included in the training, and predicted total energies were consequently underestimated in all cases. As a result, the accuracy of oxygen diffusion was evaluated by comparing the relative energy differences between the initial image and the transition state vicinity (which corresponds to the structure with the highest energy among all NEB images, referred to as NEB top).

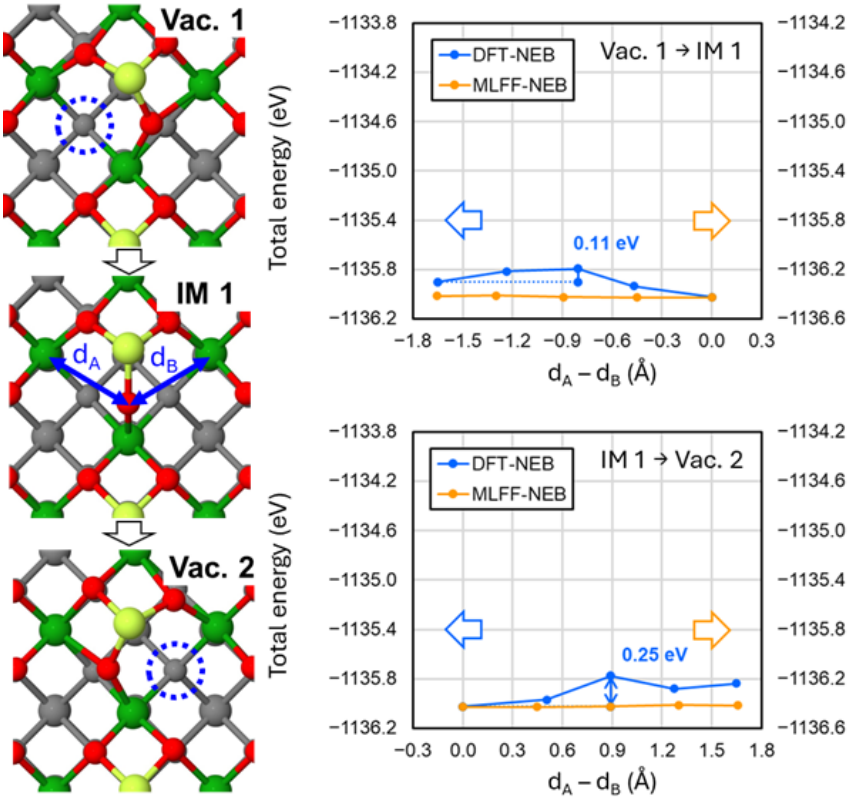


Fig. 4. Diffusion path of lattice oxygen (and oxygen vacancy) on the 100-Ce facet. The top first, second, and third Ce layers are indicated in light green, green, and gray, respectively. The top first and second O layers are shown in red and gray, respectively. The blue dashed circle is a vacancy site.

d_A and d_B represent the distances from the two Ce atoms on the left and right to the diffusing oxygen atom, and the difference between these two distances was used to compare the geometries obtained by DFT and MLFF. At the DFT level, one intermediate (IM1) with oxygen bridged on top of the first and second Ce layers was located on the diffusion pathway of oxygen atom from vac.1 to vac.2. The diffusion barrier at the DFT level from vac1 to IM1 and IM1 to vac2 were calculated to be relatively small 0.11 and 0.25 eV, respectively. Therefore, the MLFF created by the present method could not

reproduce the energy difference correctly. While energy differences among Vac. 1, IM1, and Vac. 2 are small, reaction coordinates are almost consistent among all images between DFT and MLFF.

On the 100-O-a surface, two pathways were investigated for oxygen atom diffusion. Fig. 5a shows path (a), where the diffusion occurs along a row of oxygen atoms on the 100-O-a surface. For path (a), the reaction coordinate is also defined as the difference between d_A and d_B, where d_A is the distance from the diffusing lattice oxygen atom to the Ce atom adjacent to Vac. 1, and d_B is the distance from the diffusing lattice oxygen atom to the Ce atom adjacent to Vac. 2. Since $d_A < d_B$ in Vac. 1, the reaction coordinate is negative. As the oxygen atom approaches the structure of Vac. 2, $d_A > d_B$. The relative stability of Vac. 1 and Vac. 2 is also considered. The NEB top (transition state vicinity) for both DFT and MLFF was located near $d_A - d_B = 0$. The diffusion barrier for DFT is 0.88 eV, and for MLFF, it is 0.57 eV. This is a reasonable value, considering that the RMSE of the relative energy for the oxygen vacancy surfaces is 0.48 eV (see Fig. 3).

Fig. 5b shows path (b) of oxygen atom diffusion on the 100-O-a surface, corresponding to a pathway where oxygen atoms cross a row of lattice oxygen atoms. In this pathway, a stable structure, IM1, located in the middle of the pathway connecting Vac. 1 and Vac. 2, was identified by both MLFF and DFT. The relative stability between Vac. 1 and IM1, as well as between IM1 and Vac. 2, obtained by MLFF, is similar to that obtained by DFT. For the oxygen diffusion barriers from Vac. 1 to IM1 and from IM1 to Vac. 2, the values calculated by MLFF are 0.39 eV and 0.78 eV, respectively, which are similar to those obtained at the DFT level (0.40 eV and 0.52 eV, respectively). The

difference of about 0.4 Å in the reaction coordinates of the transition state for the two pathways in Fig. 5(b), as obtained by DFT and MLFF, is not considered a significant error, given that the lattice oxygen is shifted by about 2.1 Å for each case.

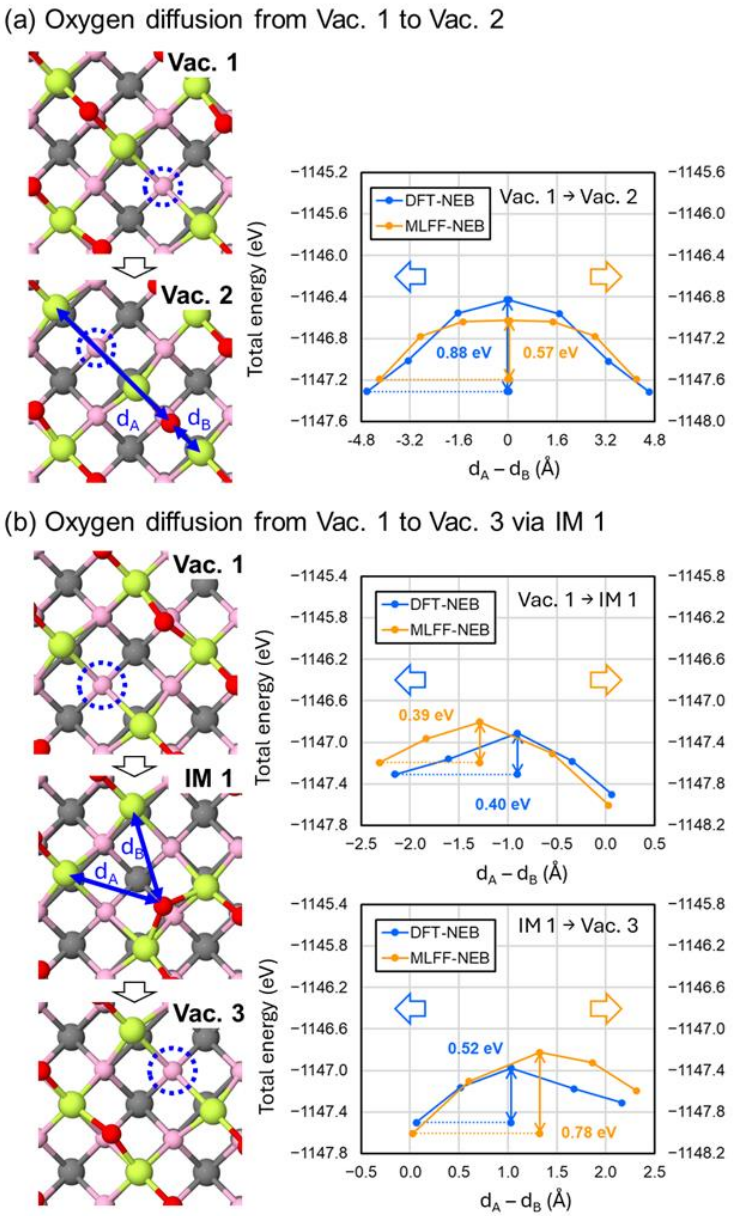


Fig. 5. Diffusion path of lattice oxygen (and oxygen vacancy) on 100-O-a facet. The top first, second and third O layers are indicated in red, pink and gray, respectively. The top first and second Ce layers are shown in light green and gray, respectively. The blue dashed circle is a vacancy site.

Two diffusion pathways were also investigated on the 110 surfaces, as shown in Fig. 6. Path (a) is a diffusion path that traverses a row of OCeO on the 110 surfaces, while path (b) is a diffusion path along a row of OCeO. A local minimum along the path (a), IM 1, was found in the DFT calculation between Vac. 1 and Vac. 2. However, the structure optimization by MLFF converged the structure of Vac. 1 and Vac. 2 as close to IM 1. Fig. 6b compared the diffusion path along the OCeO sequence on the 110 surface.

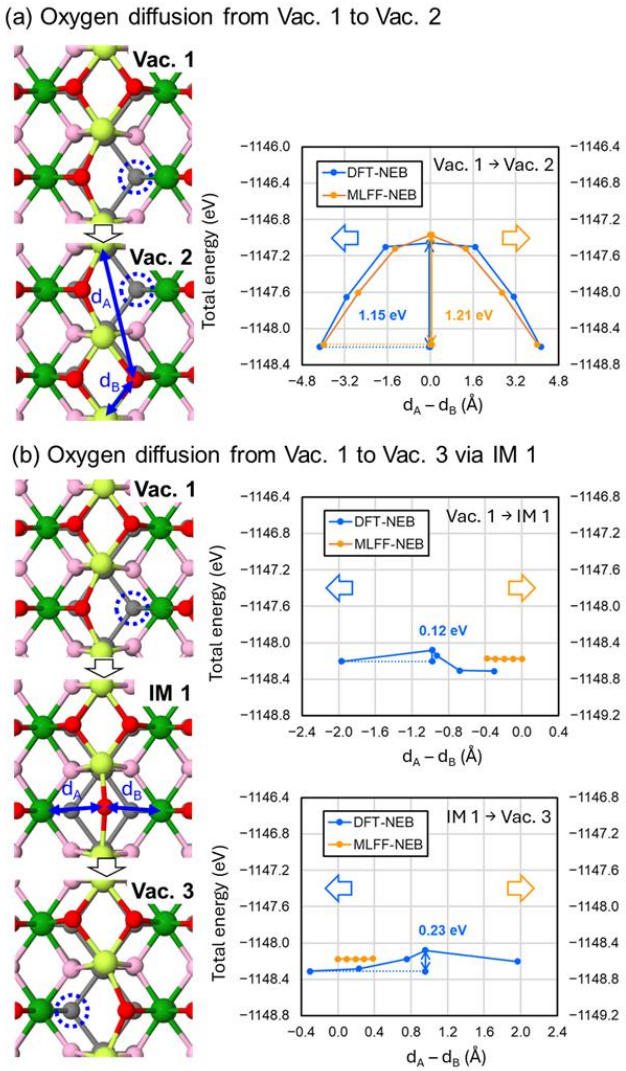


Fig. 6 Diffusion path of lattice oxygen (and oxygen vacancy) on 110 facet. The top first, second, and third Ce layers are indicated in light green, green, and gray, respectively. The top first, second third O layers are shown in red, pink and gray respectively. The blue dashed circle is a vacancy site.

The calculated diffusion barriers are 1.15 eV at the DFT level and 1.21 eV at the MLFF level. Also, the differences in the reaction pathways are similar. The energy and geometry on the diffusion path are well evaluated. This result indicates that the MLFF well reproduce the potential energy surface of the CeO_2 surface except for small (< 0.3 eV) energy differences.

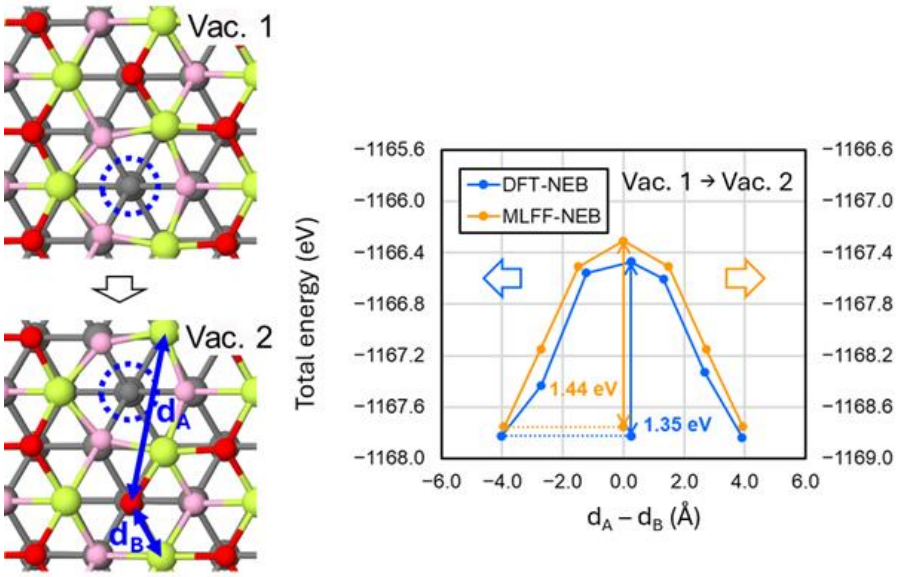


Fig. 7. Diffusion path of lattice oxygen (and oxygen vacancy) on 111 facet. The top first and second Ce layers are indicated in light green, and gray, respectively. The top first, second third O layers are shown in red, pink and gray respectively. The blue dashed circle is a vacancy site.

Fig. 7 shows the pathway through which the lattice oxygen diffuses on the topmost surface. The relative stability of Vac.1 and Vac. 2 are consistent for DFT and MLFF calculation. This diffusion pathway overcomes a barrier of 1.35 eV at the DFT level and 1.44 eV at MLFF. MLFF correctly reproduces the energy difference and structure.

3.4. Conclusions

In this study, I systematically explored an efficient way to construct MLFF based on VASP on-the-fly MLFF scheme. Our proposed approach aims to train MLFF suitable for simulating various metal oxide facets, specifically addressing oxygen vacancy stability on CeO_2 surfaces. The key elements of our efficient training approach are:

(1) Starting with Unstable Structures: More unstable initial structures accelerate the error convergence, improving force field accuracy with fewer steps.
(2) Gradual Temperature Increase: Gradually raising MD simulation temperatures (300 K to 4,000 K) helped capture diverse atomic configurations and maintain stability during on-the-fly run.
(3) Dataset Merging: Merging datasets from models with different numbers of atoms improved MLFF accuracy.

Firstly, a comparison was made regarding the initial structure of on-the-fly runs. It was found that using more unstable structures tended to converge the accuracy of the force field more quickly. The MLFF accuracy is improved with fewer MD steps when the unstable 100-Ce surface is chosen as the initial structure rather than the stable 111 surface. The unstable 100-Ce surface is thought to collapse more quickly during an on-the-fly run, which allows sampling of various local configurations with fewer MD steps.

Combining multiple training datasets can significantly enhance accuracy compared to training on a single structure for extended periods. In this research, I merged datasets from models with different numbers of atoms. However, I observed no improvement in the MLFF accuracy when merging datasets from the two-layer models, both with and without an oxygen vacancy, or when merging the two-layer and three-layer datasets with

and without an oxygen vacancy. On the other hand, merging the dataset from the three-layer models, both with and without an oxygen vacancy, led to a notable improvement: the RMSE decreased from 1.94 eV to 0.46 eV for relative energy prediction of pristine surfaces and from 1.58 eV to 0.48 eV for relative energy prediction of surfaces with an oxygen vacancy. When training using a single dataset—specifically the three-layer model with or without an oxygen vacancy—there was no such improvement in RMSE after 10,000 training steps. The results indicate that incorporating different compositions in the training datasets can enhance the MLFF performance effectively. Combining multiple training datasets can improve accuracy significantly more than focusing on a single structure for long periods.

The oxygen vacancy diffusion in CeO2 surfaces was also investigated. The relative stability of vacancy is well consistent with DFT results. The structures and energies along diffusion pathways obtained by MLFF were in relatively good agreement with those obtained by DFT. However, the MLFF failed to reproduce the qualitative stability and structure of diffusion pathways with small barriers. Insufficient sampling or regression model issues may cause this issue, and improvement of the issues is the subject of future research.

In summary, MLFF trained under high-temperature conditions correctly predicted an oxygen vacancy site's relative stability on various facets. MLFF could not distinguish structures with small energy changes in NEB calculation. However, The approach of this study will be helpful for future simulations with large-scale slab models that mimic the surface structure of real systems and will contribute to our understanding of the atomic level of metal oxide surfaces.

3.5. Supporting Information

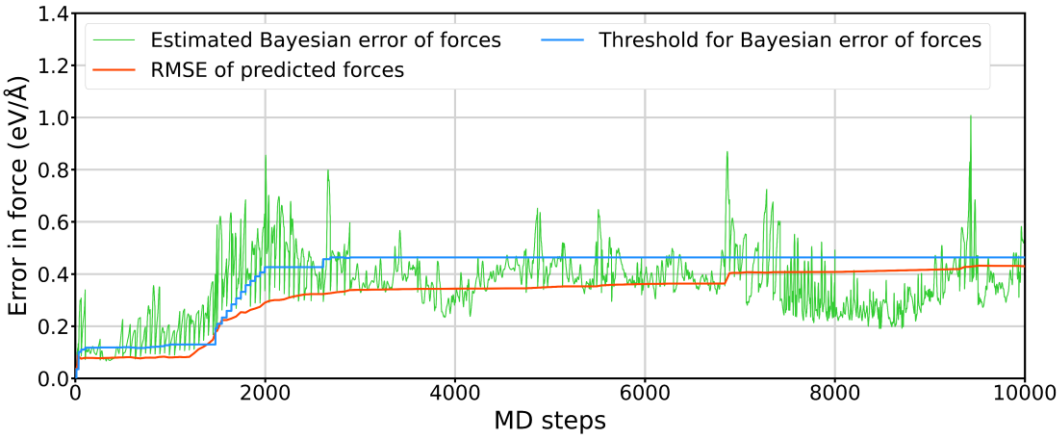


Figure S1. The trends in threshold updates and force errors for an on-the-fly run using 100-Ce_2L_0V as the training structure.

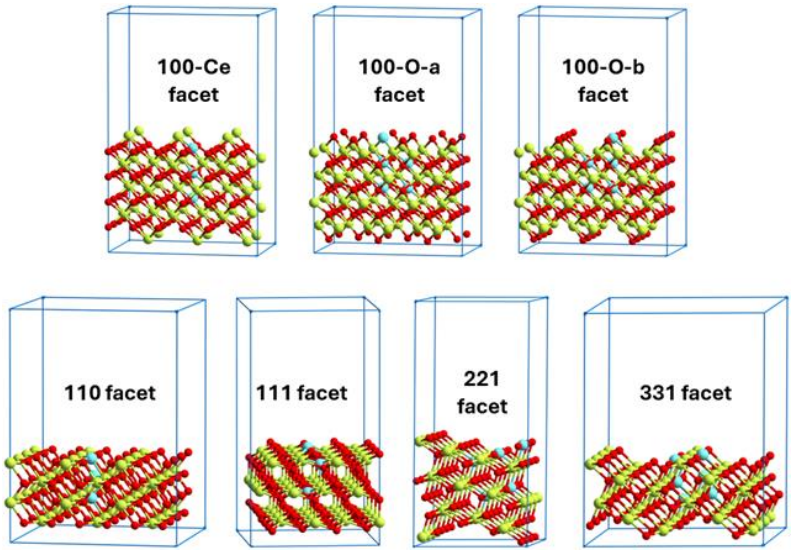


Figure S2. One oxygen atom highlighted in light blue was removed from each surface model to create surface models with an oxygen vacancy. An oxygen vacancy was selected only from the relaxed layers.

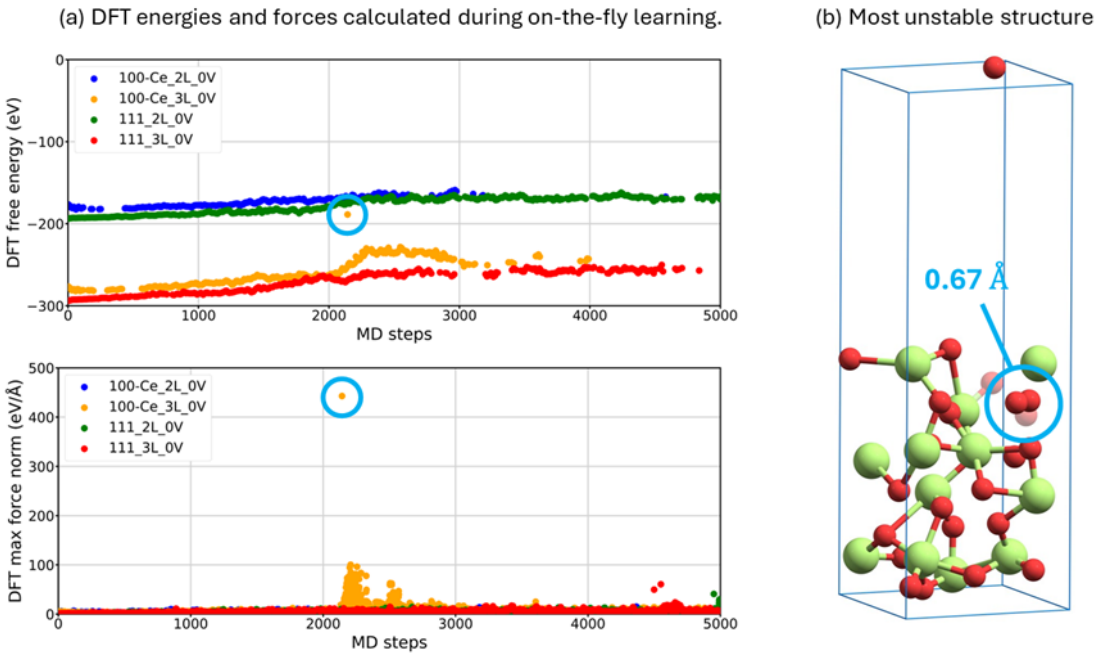


Figure S3. Results of DFT calculations during on-the-fly run. (a) Energies and forces calculated by DFT. A light blue circle indicates the most unstable result. (b) Most unstable structure. It corresponds to the results highlighted in (a).

In the training run utilizing 100-Ce_3L_0V as the initial structure, an extremely unstable configuration was observed between 2,000 and 3,000 steps. This instability arose from the proximity of the two oxygen atoms within the structure, as illustrated in part (b). This result aligns with the fact that the accuracy of the MLFF developed for 100-Ce_3L_0V deteriorated rapidly after 3,000 steps.

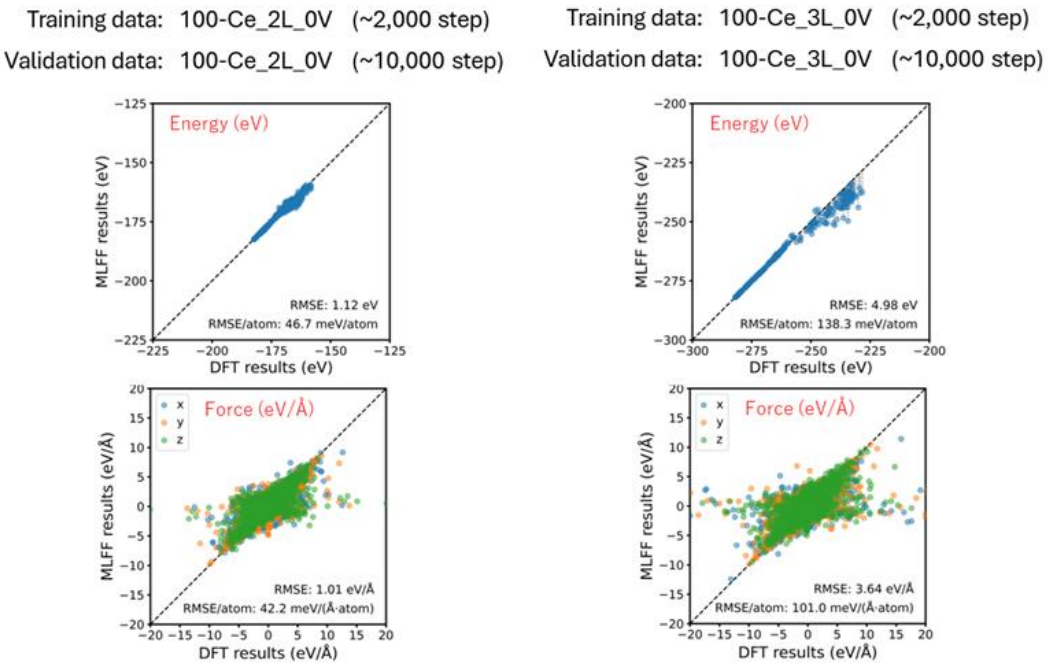


Figure S4. Reuse the results from DFT calculations obtained during on-the-fly learning to verify the accuracy of the MLFF.

In the on-the-fly run with 100-Ce_2L_0V, the MLFF constructed until 2,000 steps accurately predicted energy trends, even for structures sampled after 2,000 steps. However, in the on-the-fly run with 100-Ce_3L_0V, the MLFF constructed until 2,000 steps cannot reproduce the energies and forces of unstable structures.

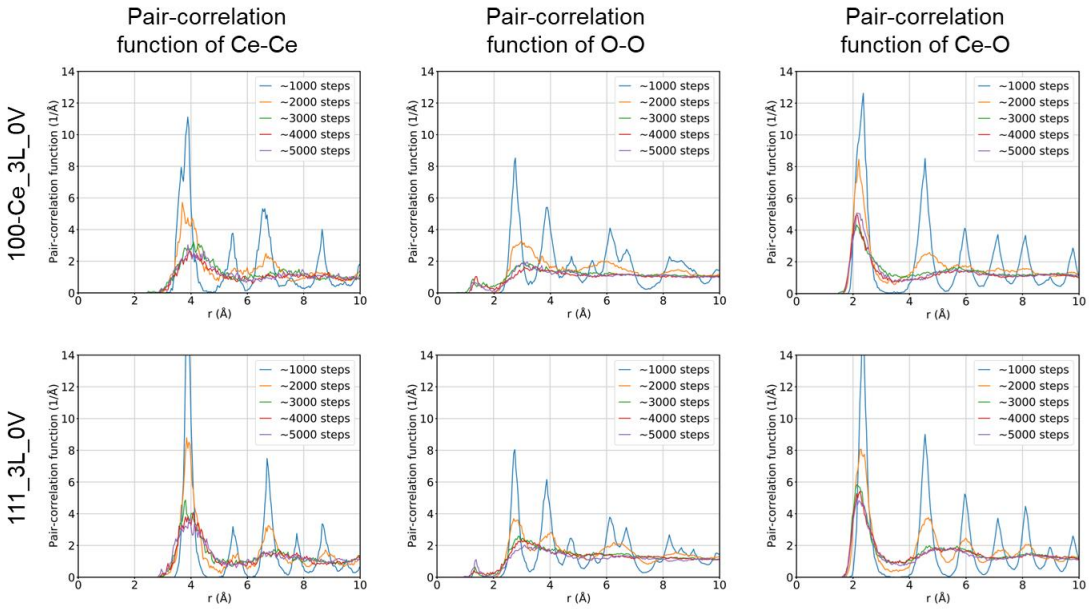


Figure S5. Pair correlation function from training run using (a) 100-Ce_3L_0V and (b) 111_3L_0V.

The pair-correlation function (PCF) is shown up to 5,000 steps. The Ce-Ce PCF indicates that the 111_3L_0V structure exhibits sharper peaks between 1,000 and 2,000 steps compared to the 100-Ce_3L_0V structure. This suggests that in the case of 111_3L_0V, the Ce atoms are relatively localized in their lattice positions until the 2,000 steps. Consequently, when using the unstable structure 100-Ce as the initial configuration, the crystal structure collapses more rapidly, leading to a broader sampling of local structures untile 2,000 steps.

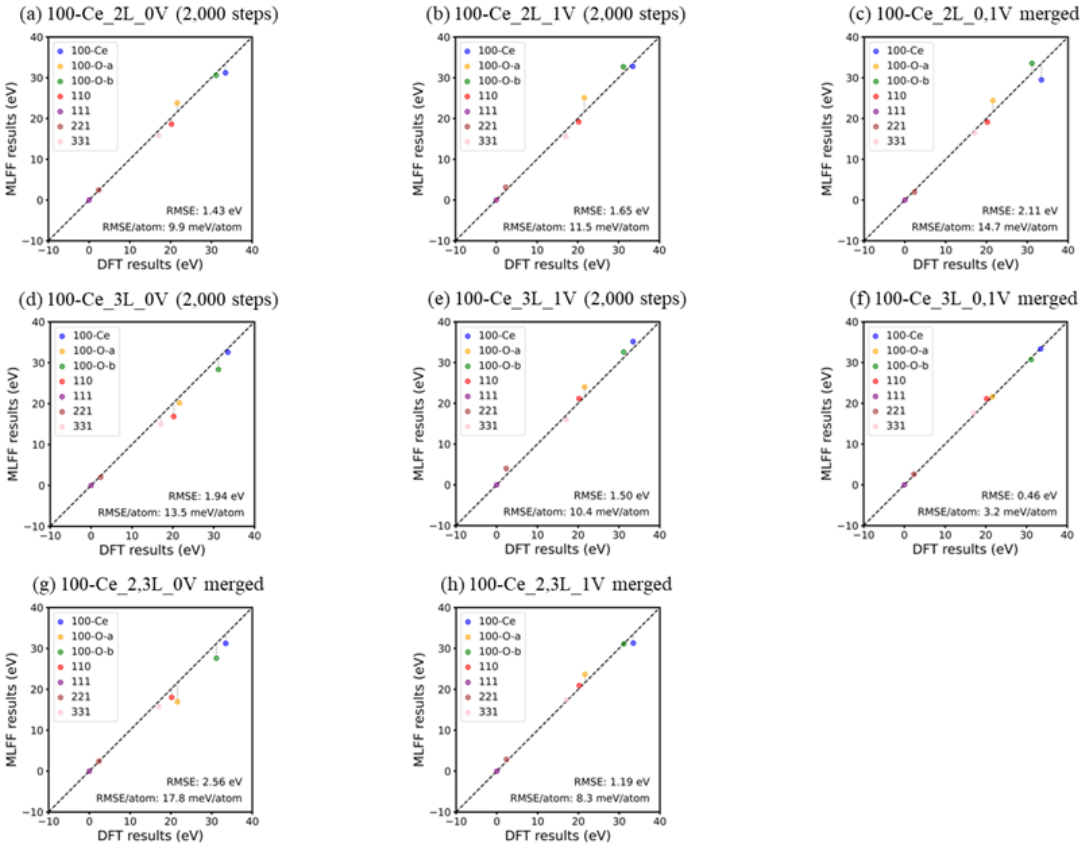


Figure S6. Comparison of the accuracy of constructed MLFF based on dataset sampled from the (a) 100-Ce_2L_0V, (b) 100-Ce_2L_1V, (d) 100-Ce_3L and (e) 100-Ce_3L_1V as initial structures. Relative predicted energies for seven pristine surfaces by MLFF. (c) trained on merging datasets from (a) and (b). (f) trained on merging datasets from (d) and (e). (g) trained on merging datasets from (a) and (d). (h) trained on merging datasets from (b) and (e).

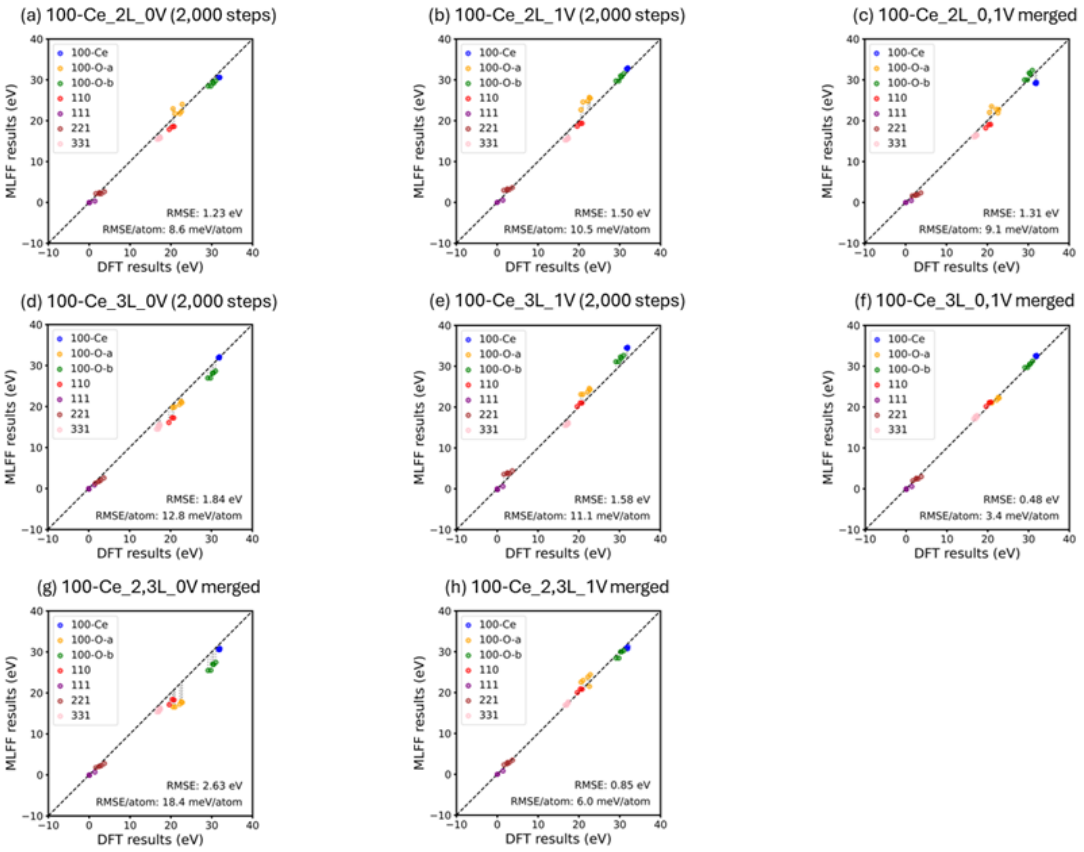


Figure S7. Comparison of the accuracy of constructed MLFF based on dataset sampled from the (a) 100-Ce_2L_0V, (b) 100-Ce_2L_1V, (d) 100-Ce_3L and (e) 100-Ce_3L_1V as initial structures. Relative predicted energies for 30 oxygen vacancy surfaces by MLFF. (c) trained on merging datasets from (a) and (b). (f) trained on merging datasets from (d) and (e). (g) trained on merging datasets from (a) and (d). (h) trained on merging datasets from (b) and (e).

3.6. References

(1) Lang, R.; Du, X.; Huang, Y.; Jiang, X.; Zhang, Q.; Guo, Y.; Liu, K.; Qiao, B.; Wang, A.; Zhang, T. Single-Atom Catalysts Based on the Metal-Oxide Interaction. *Chem Rev* **2020**, *120*, 11986-12043.

(2) Sahoo, S.; Wickramathilaka, K. Y.; Njeri, E.; Silva, D.; Suib, S. L. A review on transition metal oxides in catalysis. *Front Chem* **2024**, *12*, 1374878.

(3) Li, P.; Chen, X.; Li, Y.; Schwank, J. W. A review on oxygen storage capacity of CeO_2-based materials: Influence factors, measurement techniques, and applications in reactions related to catalytic automotive emissions control. *Catalysis Today* **2019**, *327*, 90-115.

(4) Putla, S. B.; Kamali, M.; Swapna, B.; Reddy, B. M.; Sudarsanam, P. Review of Shape-Controlled CeO_2 Nanocatalysts for Purification of Auto-Exhaust Pollutants. *ACS Applied Nano Materials* **2024**, *7*, 6749-6771.

(5) Li, L.; Zhu, B.; Zhang, J.; Yan, C.; Wu, Y. Electrical properties of nanocube CeO_2 in advanced solid oxide fuel cells. *International Journal of Hydrogen Energy* **2018**, *43*, 12909-12916.

(6) Yan, H.; Zhang, N.; Wang, D. Highly efficient CeO_2-supported noble-metal catalysts: From single atoms to nanoclusters. *Chem Catalysis* **2022**, *2*, 1594-1623.

(7) Polychronopoulou, K.; AlKhoori, A. A.; Efstathiou, A. M.; Jaoude, M. A.; Damaskinos, C. M.; Baker, M. A.; Almutawa, A.; Anjum, D. H.; Vasiliades, M. A.; Belabbes, A.; et al. Design Aspects of Doped CeO_2 for Low-Temperature Catalytic CO Oxidation: Transient Kinetics and DFT Approach. *ACS Appl Mater Interfaces* **2021**, *13*, 22391-22415.

(8) Liu, S.; Xue, Y.; Jia, Y.; Wang, H.; Nie, Q.; Fan, J. Catalytic CO oxidation on CeO_2-based materials: Modification strategies, structure-performance relationships, challenges and prospects. *Separation and Purification Technology* **2025**, *359*.

(9) Reina, T. R.; Gonzalez-Castano, M.; Lopez-Flores, V.; Martinez, T. L.; Zitolo, A.; Ivanova, S.; Xu, W.; Centeno, M. A.; Rodriguez, J. A.; Odriozola, J. A. Au and Pt Remain Unoxidized on a CeO_2-Based Catalyst during the Water-Gas Shift Reaction. *J Am Chem Soc* **2022**, *144*, 446-453.

(10) Yu, J.; Qin, X.; Yang, Y.; Lv, M.; Yin, P.; Wang, L.; Ren, Z.; Song, B.; Li, Q.; Zheng, L.; et al. Highly Stable Pt/CeO_2 Catalyst with Embedding Structure toward Water-Gas Shift Reaction. *J Am Chem Soc* **2024**, *146*, 1071-1080.

(11) Pu, Z.; Liu, Q.; Chen, C.; Wang, F. Promoting surface lattice oxygen and oxygen vacancy of CeO_2 for photothermal methane dry reforming over Ni/CeO_2 catalysts. *Chemical Engineering Journal* **2024**, *497*.

(12) Liu, B.; Liu, J.; Ma, S.; Zhao, Z.; Chen, Y.; Gong, X.-Q.; Song, W.; Duan, A.; Jiang, G. Mechanistic Study of Selective Catalytic Reduction of NO with NH_3 on W-Doped CeO_2 Catalysts: Unraveling the Catalytic Cycle and the Role of Oxygen Vacancy. *The Journal of Physical Chemistry C* **2016**, *120*, 2271-2283.

(13) Zhou, Y.; Ren, S.; Yang, J.; Liu, W.; Su, Z.; Chen, Z.; Wang, M.; Chen, L. Effect of oxygen vacancies on improving NO oxidation over CeO_2 {111} and {100} facets for fast SCR reaction. *Journal of Environmental Chemical Engineering* **2021**, *9*.

(14) Chen, W.; Xu, S. Unraveling the Complete Mechanism of the NH_3-Selective Catalytic Reduction of NO over CeO_2. *ACS Catalysis* **2023**, *13*, 15481-15492.

(15) Oshiro, K.; Gao, M.; Han, L.; Zhang, D.; Hasegawa, J.-y. Theoretical Investigation of the Alkali Metal Poisoning Tolerance Mechanism of CeO2-Containing Fe and H2SO4 Additives. *The Journal of Physical Chemistry C* **2023**, *127*, 18914-18925.

(16) Li, X.; Paier, W.; Paier, J. Machine Learning in Computational Surface Science and Catalysis: Case Studies on Water and Metal-Oxide Interfaces. *Front Chem* **2020**, *8*, 601029.

(17) Wu, Z.; Yin, W. J.; Wen, B.; Ma, D.; Liu, L. M. Oxygen Vacancy Diffusion in Rutile TiO_2: Insight from Deep Neural Network Potential Simulations. *J Phys Chem Lett* **2023**, *14*, 2208-2214.

(18) Halim, H. H.; Ueda, R.; Morikawa, Y. Machine learning molecular dynamics simulation of CO-driven formation of Cu clusters on the Cu(111) surface. *J Phys Condens Matter* **2023**, *35*.

(19) Deringer, V. L.; Bartok, A. P.; Bernstein, N.; Wilkins, D. M.; Ceriotti, M.; Csanyi, G. Gaussian Process Regression for Materials and Molecules. *Chem Rev* **2021**, *121*, 10073-10141.

(20) Vandermause, J.; Torrisi, S. B.; Batzner, S.; Xie, Y.; Sun, L.; Kolpak, A. M.; Kozinsky, B. On-the-fly active learning of interpretable Bayesian force fields for atomistic rare events. *npj Computational Materials* **2020**, *6*.

(21) Eren, B.; Zherebetskyy, D.; Patera, L. L.; Wu, C. H.; Bluhm, H.; Africh, C.; Wang, L. W.; Somorjai, G. A.; Salmeron, M. Activation of Cu(111) surface by decomposition into nanoclusters driven by CO adsorption. *Science* **2016**, *351*, 475-478.

(22) Yokaichiya, T.; Ikeda, T.; Muraoka, K.; Nakayama, A. On-the-fly kinetic Monte Carlo simulations with neural network potentials for surface diffusion and reaction. *J Chem Phys* **2024**, *160*.

(23) Timmermann, J.; Lee, Y.; Staacke, C. G.; Margraf, J. T.; Scheurer, C.; Reuter, K. Data-efficient iterative training of Gaussian approximation potentials: Application to surface structure determination of rutile IrO_2 and RuO_2. *J Chem Phys* **2021**, *155*, 244107.

(24) Kobayashi, T.; Ikeda, T.; Nakayama, A. Long-range proton and hydroxide ion transfer dynamics at the water/CeO_2 interface in the nanosecond regime: reactive molecular dynamics simulations and kinetic analysis. *Chem Sci* **2024**, *15*, 6816-6832.

(25) Kresse, G.; Furthmuller, J. Efficiency of ab-initio total energy calculations for metals and semiconductors using a plane-wave basis set. *Comp Mater Sci* **1996**, *6*, 15-50.

(26) Kresse, G.; Furthmuller, J. Efficient iterative schemes for *ab initio* total-energy calculations using a plane-wave basis set. *Phys Rev B Condens Matter* **1996**, *54*, 11169-11186.

(27) Grimme, S.; Antony, J.; Ehrlich, S.; Krieg, H. A consistent and accurate ab initio parametrization of density functional dispersion correction (DFT-D) for the 94 elements H-Pu. *J Chem Phys* **2010**, *132*, 154104.

(28) Dudarev, S. L.; Botton, G. A.; Savrasov, S. Y.; Humphreys, C. J.; Sutton, A. P. Electron-energy-loss spectra and the structural stability of nickel oxide: An LSDA+U study. *Phys Rev B* **1998**, *57*, 1505-1509.

(29) Jain, A.; Ong, S. P.; Hautier, G.; Chen, W.; Richards, W. D.; Dacek, S.; Cholia, S.; Gunter, D.; Skinner, D.; Ceder, G.; et al. Commentary: The Materials Project: A materials genome approach to accelerating materials innovation. *APL Materials* **2013**, *1*.

(30) Andersson, D. A.; Simak, S. I.; Johansson, B.; Abrikosov, I. A.; Skorodumova, N. V. Modeling of CeO_2, Ce_2O_3, and CeO_{2-x} in the LDA+*U* formalism. *Phys Rev B* **2007**, *75*.

(31) Plata, J. J.; Marquez, A. M.; Sanz, J. F. Communication: improving the density functional theory+*U* description of CeO_2 by including the contribution of the O 2*p* electrons. *J Chem Phys* **2012**, *136*, 041101.

(32) Matz, O.; Calatayud, M. Breaking H_2 with CeO_2: Effect of Surface Termination. *ACS Omega* **2018**, *3*, 16063-16073.

(33) Jiang, Y.; Adams, J. B.; van Schilfgaarde, M. Density-functional calculation of CeO_2 surfaces and prediction of effects of oxygen partial pressure and temperature on stabilities. *J Chem Phys* **2005**, *123*, 64701.

(34) Prieur, D.; Bonani, W.; Popa, K.; Walter, O.; Kriegsman, K. W.; Engelhard, M. H.; Guo, X.; Eloirdi, R.; Gouder, T.; Beck, A.; et al. Size Dependence of Lattice Parameter and Electronic Structure in CeO_2 Nanoparticles. *Inorg Chem* **2020**, *59*, 5760-5767.

(35) Henkelman, G.; Uberuaga, B. P.; Jónsson, H. A climbing image nudged elastic band method for finding saddle points and minimum energy paths. *The Journal of Chemical Physics* **2000**, *113*, 9901-9904.

(36) Alex Ganose, A. O. pymlff. https://github.com/utf/pymlff (accessed 2024 December 12th).

(37) Hoover, W. G.; Ladd, A. J. C.; Moran, B. High-Strain-Rate Plastic Flow Studied via Nonequilibrium Molecular Dynamics. *Physical Review Letters* **1982**, *48*, 1818-1820.

(38) Evans, D. J. Computer ‘‘experiment’’ for nonlinear thermodynamics of Couette flow. *The Journal of Chemical Physics* **1983**, *78*, 3297-3302.

Chapter 4. General Conclusion

Heterogeneous catalysts contain a variety of surface structures and many more types of adsorption sites, which are possible due to defects and atomic arrangements, making it a challenging task to elucidate the relationship between catalytic activity and their structures. To address this issue, in this thesis, I first screened adsorption sites based on first-principles thermodynamics to search for stable surface structures and investigate the mechanism of alkali poisoning resistance. Next, I investigated the efficient way to construct MLFF to calculate the stability of oxygen vacancy sites on different facets.

In Chapter 2, DFT calculations were used to investigate the mechanism of the excellent alkali poisoning resistance of $Fe/H_2SO_4/CeZr$ catalysts and the role of the additives Fe and H_2SO_4. Models of the catalyst surface under experimental conditions were studied based on first-principles thermodynamic methods. Fe and H_2SO_4 promote forming an oxygen vacancy on the CeO_2 surface. Screening of stable SO_4^{2-} adsorption structures around the oxygen vacancy suggested by calculations that they form a characteristic adsorption site ($SO_4/Fe_CeO_2_V_O$). Using various surface models, I further examined the adsorption sites of K atoms and NH_3, the reducing agent. It was found that on a normal CeO_2 surface, the adsorption of NH_3 is inhibited by the adsorption of K on the lattice oxygen, where the Brønsted acid site, one of the NH_3 adsorption sites, is formed. On the other hand, calculations indicate that the $SO_4/Fe_CeO_2_V_O$ site can accumulate multiple K atoms. This result suggests that the surface structure created by Fe and H_2SO_4 separates K atoms from NH_3 adsorption sites, thereby maintaining the excellent NO_X conversion of the $Fe/H_2SO_4/CeZr$ catalyst.

In Chapter 3, an efficient method for constructing MLFF based on VASP on-the-fly ML scheme was investigated. The approach proposed in this thesis aims to train MLFF

suitable for simulating various surface structures, explicitly dealing with oxygen vacancy stability and its diffusion on CeO_2 surfaces. The efficient learning approach in this thesis consists of three components:

(1) Starting the training run from an unstable structure: Structural diversity in the training data was achieved earlier using a more unstable initial structure.

(2) Increasing simulation temperature: Gradually increasing the temperature of the training run (from 300 K to 4,000 K) allowed us to capture a variety of atomic configurations while maintaining stability.

(3) Merging datasets: Merging datasets of models with different numbers of atoms improved the accuracy of MLFF.

For (1), a comparison was made concerning the initial structure of the training run. The accuracy of the MLFF tends to converge more quickly when a more unstable structure is used; the accuracy of the MLFF was improved with fewer MD steps when an unstable 100-Ce surface was chosen as the initial structure over a stable 111 surface. It is thought that the unstable 100-Ce surface can collapse faster on the fly and thus sample a variety of local structures with fewer MD steps.

For (3), I considered combining data from different training runs. Merging the three-layer data sets with and without the oxygen vacancy model improved the RMSE from 1.94 eV to 0.46 eV for the prediction of relative energy on the pristine surface and 1.58 eV to 0.48 eV for the prediction of relative energy on the surface with oxygen vacancy. The RMSE did not improve much after 10,000 learning steps for each training run. On the other hand, training with different compositions can improve MLFF very efficiently.

Combining multiple training datasets can improve accuracy more effectively than learning a single composition over an extended period.

The diffusion of an oxygen vacancy on the CeO_2 surface was also studied using the final force field created. The structure and energies along the diffusion path obtained by MLFF were in relatively good agreement with those obtained by DFT. On the other hand, MLFF failed to reproduce the qualitative stability and structure when the energy change was small. Insufficient sampling or regression model issues may cause this issue, and improvement of the issues is the subject of future research.

MLFF trained under high-temperature conditions correctly predicted the relative stability of an oxygen vacancy on various surfaces; MLFF could not distinguish structures with extremely small energy differences in the NEB calculations. The present approach will be helpful for future simulations using large-scale slab models that mimic the surface structure of real systems and will contribute to our understanding of metal oxide surfaces at the atomic level.

Acknowledgment

I would like to express my heartfelt gratitude to Hasegawa-sensei for his exceptional guidance and support throughout the past five years. Despite his demanding responsibilities as the institute director, he always made time to discuss my research and provide thoughtful advice. His guidance on research direction, fellowship applications, conference presentations, and many other aspects of my research activities at Hokkaido University has been invaluable.

I would like to extend my heartfelt gratitude to Gao-sensei, who directly supervised my research over the past five years. She introduced me to collaborative projects with the Fukuoka group at the ICAT and the ICReDD team, greatly enriching my understanding of catalytic reactions. Her extensive support throughout drafting my research papers—from shaping the overall narrative to proofreading the details—was invaluable. I also profoundly appreciated her thoughtful gestures, like treating us to soup curry during our discussions. Her constant encouragement and unwavering support have been instrumental in completing this thesis; I am genuinely grateful for that.

I am sincerely grateful to Iida-sensei for his meticulous guidance during our reading circle on the fundamentals of quantum chemistry. His insightful advice on solid-state DFT calculations during group meetings was invaluable. I sincerely appreciate his detailed instruction and support.

Since I first visited the Hasegawa Laboratory, Miyazaki-sensei has been an incredible source of guidance and support. His advice has been invaluable, not just for my research but also for various aspects of life as a graduate student. He was there to help me transition smoothly into the doctoral course. He introduced me to other students in ICAT and

fostered meaningful interactions. I truly appreciate his efforts in promoting communication and building connections between laboratories, which significantly enriches my experience.

Shiraogawa-sensei often invited me out for meals, providing gentle encouragement. He also shared thoughtful insights about research and career paths that helped me think more deeply. His clear explanations of programming and electronic state theory greatly enriched my research. I am genuinely grateful for the support he has given me.

I am deeply grateful to Morita-san for her outstanding support with the administrative tasks related to my research assistantship and fellowship applications. Her swift and efficient handling of these processes allowed me to focus entirely on my research and conference presentations. I truly appreciate her kind and dedicated assistance, which immensely helped my research activities.

I am deeply grateful to Harabuchi-sensei for his invaluable advice on my research throughout our collaborative work and for his constant encouragement while writing my thesis. I also sincerely appreciate his kindness in inviting me to various events, including sports activities, which provided a refreshing break and valuable opportunities for interaction.

During our collaborative research, S., Ruben-sensei provided me with clear and detailed explanations of machine learning potentials and helpful references to relevant literature. His guidance greatly enhanced my understanding of this area, and I am truly grateful for his support and valuable insights.

I would like to express my sincere gratitude to Nus-san (Dr. Manussada Ratanasak) for the cheerful demeanor and thoughtful sense of humor, which were a constant source of encouragement. The insightful and detailed questions during our group meeting helped me gain new perspectives on my research. I am genuinely grateful for Nus-san's kindness and thoughtful support.

I am deeply grateful to Bim-san (Dr. Rattanawalee Rattanawan), Danjo-san (Dr. Danjo De Chavez), and May-san (Dr. Sarinya Hadsadee) for the thoughtful advice and insights shared during our group meeting on my research. Their dedication and accomplishments as postdoctoral researchers have been truly inspiring and have served as wonderful examples, encouraging me to immerse myself even more in my work. I sincerely appreciate all of their support.

As a fellow member of the Hasegawa Laboratory, I am genuinely grateful for the wonderful memories we created together during group meetings, reading circles, and lab events. The support and friendship of R. Hosaka-san, R. Hara-san, T. Chiba-san, and H. Hirase-san made my time in the laboratory both fulfilling and enriching. I sincerely appreciate all of your kindness and encouragement. Thank you very much.

I want to thank S. Kato-san, S. Toyama-san, and H. Itakura-san for creating a bright and lively atmosphere in the laboratory. Your presence always brought energy and positivity, making my time in the lab all the more enjoyable.

I would like to express my heartfelt thanks to the laboratory members for their support throughout graduate school. Their thoughtful encouragement and meaningful exchanges have been a great source of strength, and they played a crucial role in helping me complete this thesis.

I would like to express my heartfelt gratitude to Arimitsu-sensei for teaching me research fundamentals at University of the Ryukyus. Your encouragement and thoughtful advice inspired me to pursue graduate studies, ultimately enabling me to complete my doctoral course. I am deeply grateful for your support.

I am genuinely grateful to T. Ishikawa-san, E. Gima-san, P., Samira-san, and K. Endo-san for their guidance on the basics of organic synthesis during my time at University of the Ryukyus. Although my current research field is computational chemistry, the support and experiences I gained in the Arimitsu Lab became a significant driving force behind my approach to research. Thank you very much for your kindness and support.

I want to express my heartfelt gratitude to Tomomichi Tatsuyama and Satsuki Iwasa. As lab members at University of the Ryukyus, we spent many hours together studying for graduate school entrance exams and overcoming the challenges of research life. The memories we shared during our undergraduate and graduate years have been a source of encouragement and support as I worked on my doctoral dissertation. Thank you so much for everything.

To my parents, grandparents, and aunts. Thank you for your unwavering support and understanding of my career decisions. I know there were times when I caused you concern. However, your constant encouragement and belief in me gave me the confidence and strength to complete my doctoral dissertation. I am deeply grateful to all of you for always cheering me on.